



UNIVERSITY OF COPENHAGEN
FACULTY OF SCIENCE

Master's Thesis

Meghana Killi

Compact LAEs at High-z: Feature or Anomaly?

Thesis Advisor: Gabriel Brammer

Principal Supervisor: Darach Watson

Handed in: August 23, 2021

DAWN

COSMIC DAWN CENTER

Contents

1	Introduction	1
1.1	Morphology	1
1.1.1	UV Continuum vs Ly α Line	2
1.2	Astro-physical Properties from SED	4
1.2.1	SFR vs Stellar mass	6
1.2.2	Galaxy Luminosity Function	7
2	Compact Objects	9
2.1	Observational Origin for Compactness	9
2.1.1	Dust and the Nature of Ly α	9
2.1.2	Slitless Spectroscopy	10
2.1.3	Low SNR	11
2.1.4	IGM absorption	12
2.1.5	Clumpy Star-formation	12
2.1.6	AGN	13
2.2	Physical Origin for Compactness	13
2.2.1	High-z Galaxies	13
2.2.2	LAEs	14
2.2.3	Super Star clusters	15
3	Methods	17

3.1	Data	17
3.1.1	Fields and Filters	17
3.1.2	HST Grism Data	18
3.1.3	Skelton Catalog	19
3.1.4	Parent Sample Selection	19
3.1.5	Ly α Detection	21
3.2	Sérsic Model Fitting with GALFIT	23
3.2.1	GALFIT Description	23
3.2.2	Fitting Procedure	24
3.2.3	GALFIT Input	24
3.3	SED fitting with EAZY	27
3.3.1	EAZY Description	28
3.3.2	EAZY Input	28
4	Results	29
4.1	Results from GALFIT	29
4.1.1	GALFIT Output	29
4.1.2	1D Surface Brightness Profiles	30
4.1.3	Line vs Continuum Morphology	31
4.1.4	Spatial Offset between Line and Continuum	32
4.1.5	Comparison of GALFIT parent and sub-sample	33
4.2	Results from EAZY	37
4.2.1	EAZY Output	37
4.2.2	Comparison of EAZY parent and sub-sample	37
4.3	Summary	42
5	Discussion and Further Work	45
5.1	Comparison of Sub-sample with Literature	45

CONTENTS

5.1.1	Van Der Wel Catalog	45
5.1.2	ALPINE Survey	46
5.1.3	Quasars and AGN	46
5.2	Error Analysis	47
5.2.1	GALFIT errors	47
5.2.2	EAZY Errors	49
5.3	Noise	49
5.4	LAE vs LBG	49
6	Conclusion	53
A	Appendix of GALFIT and EAZY Fits for Sub-sample	69
A.1	s_12390	69
A.2	s_17197	71
A.3	s_17357	72
A.4	s_18207	73
A.5	s_21181	74
A.6	s_26144	75
A.7	s_33531	76
A.8	s_36953	77
A.9	s_43831	78
A.10	s_44106	79
A.11	n_16335	80
A.12	n_16708	81
A.13	n_29365	82
A.14	n_31351	83
A.15	n_39376	84
A.16	e_06005	85

A.17 e_18484	86
------------------------	----

List of Figures

1.1	Sérsic Profiles	3
1.2	SFR vs Stellar Mass (from literature)	6
1.3	Luminosity Function (from literature)	8
2.1	IGM Absorption	12
2.2	Star-forming Region	13
3.1	CANDELS Footprints	18
3.2	HST Filters	19
3.3	Grism Spectrum	20
3.4	Spurious Detection	22
3.5	Redshift Distribution	23
3.6	GALFIT Input Images	25
4.1	GALFIT Fit	30
4.2	1D Surface Brightness Profile	31
4.3	GALFIT radii with continuum morphology	32
4.4	GALFIT radii with $Ly\alpha$ morphology	33
4.5	$Ly\alpha$ -Continuum offsets	34
4.6	GALFIT Parameter Pairplot	35
4.7	GALFIT Radius-Redshift	36
4.8	GALFIT Radius-Redshift by Magnitude	36

4.9	EAZY SED	38
4.10	Redshift evolution of SFR and stellar mass	39
4.11	SFR vs Stellar Mass (this work)	40
4.12	Luminosity Function (this work)	41
5.1	Comparison with Van Der Wel	46
5.2	GALFIT Uncertainty	48
5.3	Noisy Continuum Image	50

List of Tables

3.1	SNR for Sub-sample	21
3.2	Sample Breakdown	22
3.3	Magnitude Zeropoints	26
3.4	GALFIT constraint file	27
4.1	GALFIT Parameters	30
4.2	Sub-sample Summary	43
5.1	Comparison with ALPINE survey	46

Abstract

Young star-forming galaxies in the early Universe can be identified by their intense Hydrogen Lyman- α ($Ly\alpha$) emission that is bright enough to be projected like a beacon nearly all the way across the Universe. This radiation provides valuable insight into the formation of the first galaxies and their evolution over cosmic time. The goal of this project was to take advantage of this illuminating emission line to understand the lives of the smallest of these star-forming galaxies. What follows is a summary of our findings thus far.

We present a sample of 17 bright, yet extremely compact (~ 1 kpc size) $Ly\alpha$ emitters (LAEs) at $z \sim 4-7$ selected from a parent sample of 1060 Lyman-break galaxies (LBGs) observed in (Hubble Space Telescope) HST data in 4 of the 5 CANDELS fields. We compare and contrast the sub-sample and parent sample with the aim of identifying the cause of the compact nature of these objects.

We make relative size measurements by fitting Sérsic profiles to the $Ly\alpha$ line and UV continuum morphology images, and find that the sub-sample of LAEs is generally more compact than the parent sample of LBGs. Within the sub-sample, $Ly\alpha$ morphology is more compact than UV continuum, contrary to the expectation of extended halos.

We also fit templates to the spectral energy distributions (SEDs) of the objects based on photometric flux measurements from the Skelton catalog (Skelton et al. 2014). Here, we find that the sub-sample star-formation rates and stellar masses are generally higher than the parent sample.

Based on our results and findings from literature, we tentatively conclude that the compact nature is partly a true physical feature of high- z LAEs and partly due to observational limitations. In other words, it is both a feature and an anomaly.

Chapter 1

Introduction

In this chapter, we provide some scientific background on relevant topics, including astro-physical properties of the objects we study, the methods used to detect and measure these objects, and some common analysis techniques used to retrieve the physical properties from observations.

1.1 Morphology

A galaxy's structure is a result of the physical processes that occur in its life-time such as its assembly, interaction with its surroundings and nearby objects, and its star-formation history. Therefore, measuring and quantifying galaxy morphology, and studying how it evolves across cosmic time (i.e., with decreasing redshift (z)) can give us crucial information about their stage of evolution at each cosmic epoch.

The traditional classification of galaxy morphology involves the Hubble tuning fork diagram (Hubble 1926) that classifies galaxies into elliptical, spiral, and irregular (e.g. Jarrett 2000). This classification led to the theory that galaxies evolve from spiral to elliptical via irregular, which is thought to be two galaxies in the process of merging. All the gas in the merging galaxies is used up during the intense star-bursting episode that results from the merger, leaving a quenched elliptical in their place (Baugh, Cole, and Frenk 1996).

However, the traditional Hubble sequence is of limited applicability at high- z (see Sec.2.2.1). In this case, galaxy structure must be studied using either parametric and non-parametric methods. Parametric approaches fit analytic models to a galaxy's light distribution (e.g; Boris Häußler et al. 2013, Robotham et al. 2017). Such parametric methods are valuable for classifying symmetrical Hubble-type galaxies. However, they are known to break down for more irregular, peculiar-type galaxies, as they assume a smooth light distribution. But for our compact objects, parametric fitting using the Sérsic profile (Sérsic 1963) seems to work well (Sec.3.2.2).

Sérsic Profile

The two-dimensional surface brightness of galaxies is often described in terms of the Sérsic profile (Sérsic 1963), which takes the form

$$\Sigma(r) = \Sigma_e \exp \left[-\kappa \left(\left(\frac{r}{r_e} \right)^{1/n} - 1 \right) \right] \quad (1.1)$$

where r_e is the effective radius defined such that half of the flux lies within r_e , and Σ_e is the surface brightness at r_e . The parameter n , which is coupled to κ , is the Sérsic index; a higher Sérsic index indicates a steep inner brightness profile and more extended wings, while a lower index indicates a shallower profile at small radius and less extended wings. κ is a free parameter defined as $\kappa = \frac{\Gamma(2n)}{2}$, where Γ is the complete gamma function. The case of $n = 4$ is the de Vaucouleurs profile, often used to model classical bulges (de Vaucouleurs 1948). Values of $n = 1$ and $n = 0.5$ describe exponential disks and Gaussian profiles, respectively (Kimbrell et al. 2021).

The Sérsic index provides a classification scheme analogous to the Hubble tuning fork, where a low Sérsic index describes a “disky” galaxy and a higher index is characteristic of a more centrally concentrated elliptical morphology (Fig.1.1).

Fig.1.1 shows Sérsic profiles with varying Sérsic indices, where r_e and Σ_e are held fixed. This plot can be read as the upper right quadrant of a face-on galaxy. As the Sérsic index increases, the central core profile gets steeper, and the outer wing becomes more extended. A low n has a flatter core and a more sharply truncated wing.

1.1.1 UV Continuum vs Ly α Line

We can compare the size of the source as it appears in various bands, including UV, IR, and optical to estimate stellar, gas, and dust components. Nelson et al. 2012 compared the $H\alpha$ morphology with the stellar continuum morphology of galaxies at $z \sim 1$, and found that the $H\alpha$ emission is slightly more extended. Since $H\alpha$ scales with the quantity of ionizing photons produced by hot young stars, it can be used to trace the young, high-mass stellar population. The rest-frame optical or near-IR stellar continuum emission, on the other hand, traces the stellar mass of a galaxy, which is dominated by the old stellar population. They thus surmised that the the youngest stars have a more extended distribution than older stars, meaning star formation was proceeding from the center of the galaxy to its edges. In other words, the galaxies were forming stars inside-out.

In this project, we compare the morphologies as observed in the UV continuum and Ly α line. The former traces the massive O and B stars, while the latter traces the gas both immediately around these stars, but also up to a large distance out of the star-forming regions, thanks to the scattering effects of Ly α (see. Sec.2.1.1).

The reason for choosing Ly α over $H\alpha$ and UV continuum over optical continuum is simple. For the galaxies of interest at $z > 4$, the Balmer-series hydrogen recombination

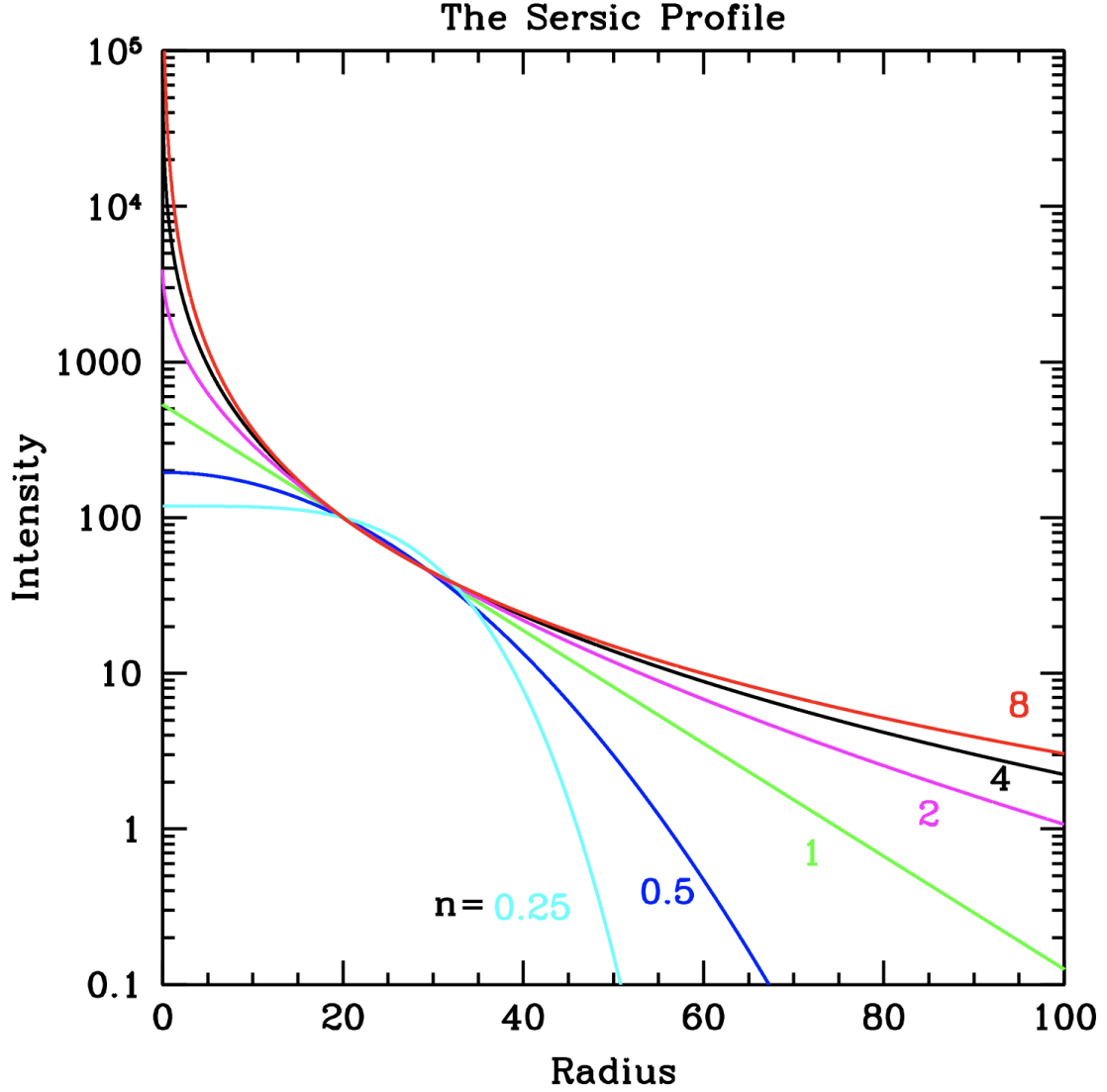


Figure 1.1: Sérsic profiles with each colored curve representing different Sérsic indices (Peng et al. 2010)

lines like $H\alpha$ and the rest-frame optical stellar continuum are redshifted to infrared wavelengths beyond the reach of current instrumentation.

$Ly\alpha$

Most of the $Ly\alpha$ emission we see from a galaxy is produced when H recombines in the neutral interstellar medium after being ionized by high energy photons from hot, massive main sequence O and B stars (and AGN if any). 2/3 of these ionizing photons are converted into $Ly\alpha$ photons, resulting in what can often be the strongest feature in a galaxy's spectrum. The first major burst of star formation in a young, high- z galaxy is therefore expected to produce large numbers of ionizing photons in a mostly dust-free environment, which is exactly the kind of location where we expect to emit copious amounts of $Ly\alpha$ photons.

This is why beginning in the 1960s, $Ly\alpha$ emission has been used as a signature of young galaxies in the absence of dust (Partridge and Peebles 1967). Several studies since, such as the Large Area Lyman Alpha (LALA) survey (J.E. Rhoads et al. 2001, Malhotra, J. Rhoads, et al. 2001) and Lyman Alpha Reference Sample (LARS) survey series (Hayes, Östlin, Schaerer, et al. 2013, Hayes, Östlin, Duval, et al. 2014), have utilized this feature to identify dust-free young galaxies.

However, the observation of $Ly\alpha$ itself does not guarantee a young age or absence of dust (Finkelstein et al. 2015), but only indicates active star formation and lack of dust along the line of sight. The properties we derive will accordingly be affected by our point of view in time and space.

Furthermore, $Ly\alpha$ undergoes resonant scattering (see Sec.2.1.1), which creates large, extended halos around the stars.

Thus, our $Ly\alpha$ observations trace the gas (out to large distances) around young stars during a star-forming episode (not necessarily the first) in the lifetime of the galaxy.

UV Continuum Emission

In a galaxy, the UV continuum radiation is produced directly by O and B stars, akin to continuous blackbody radiation. Thus, continuum emission traces the young stellar population in a galaxy. Just as in the case of $Ly\alpha$, the properties we derive based on UV continuum morphology are affected by the amount of gas and dust along the line of sight. That said, the SNR for continuum observations is higher (see Table 3.1), which will allow us to discern more diffuse structure and features we may miss in line observations.

1.2 Astro-physical Properties from SED

Just as with morphology (Sec.1.1), extracting physical properties requires model-based fitting of the SED. For this project, we use the Easy and Accurate Zphot from Yale (EAZY; G. B. Brammer, P. G. van Dokkum, and Coppi 2008) algorithm to perform this fitting (Sec.3.3.1).

The spectral energy distribution (SED) of galaxies is used to derive photometric redshifts and basic physical properties such as stellar mass and SFR (e.g. Conroy 2013, Salvato, Olivier Ilbert, and Hoyle 2019).

Rest-frame UV to optical SEDs of high- z LAEs can be obtained from the combination of deep optical and near-infrared data (Gawiser et al. 2007, Gawiser 2009, Lai et al. 2008, Jiang, Finlator, et al. 2016). Although, addition of longer wavelength flux data is necessary to probe the dust peak.

The accuracy of derived properties depends on the galaxy type, redshift range, specific set of filters, observational depth, treatment of line emission contributions, and

availability of spectroscopic redshifts to calibrate the photometric redshift (Förster Schreiber and Wuyts 2020). But especially in well-studied fields such as GOODS-S and COSMOS, extensive photometry in ~ 40 optical to mid-IR bands, photometric redshift estimates lead to very high accuracy (Skelton et al. 2014, Laigle et al. 2016).

IMF

The Initial Mass Function (IMF) of a galaxy gives the distribution of stellar masses, i.e., how many more low-mass stars there are compared to high-mass stars. This has been studied extensively for the nearby Universe. For the solar neighborhood, we commonly use the Kroupa (Kroupa 2001) or Chabrier IMF (Chabrier 2003) and for the galactic disk, the Salpeter IMF (Salpeter 1955). Each one has slightly more or fewer stars of one kind than the other; the Salpeter IMF is more bottom-heavy than Kroupa, i.e., it has more low-mass stars, Chabrier IMF has more high-mass stars than Salpeter, and so on. However, it is impossible to say whether any of these describes in any detail, the true distribution of stars in distant galaxies.

For lack of better information, the IMF is assumed to be universal, with the same shape at all times and in all galaxies. Usually, it is one of those mentioned above. Unsurprisingly, the IMF is one of the largest sources of systematic uncertainty in measurements of mass from light (Conroy 2013).

In this work, we assume a Chabrier IMF for all our calculations.

UV SFR

The star formation rate (SFR) of a galaxy is the amount of gas mass that it is converting into stars per unit time. This is related to the number of O and B stars it has, because once the galaxy stops forming stars, this stars quickly die out within a few tens of Myr. These stars emit the vast majority of their light in the UV. Hence, the UV luminosity can be used as a tracer for star formation rate.

For a Salpeter IMF, and within the wavelength range of 1500 to 2800 Å, the UV SFR can be calculated from UV luminosity using the Kennicutt relation (Kennicutt 1998) as

$$SFR(M_{\odot}yr^{-1}) = 1.4 \times 10^{-28} L_{\nu}(erg\ s^{-1}\ Hz^{-1}). \quad (1.2)$$

Then, using

$$M_{UV} = -2.5 \log(L_{\nu}) + 51.6, \quad (1.3)$$

for a Chabrier IMF, the UV SFR is estimated as

$$SFR(M_{\odot}yr^{-1}) = 3.8 \times 10^{-8} \times 10^{-\frac{(M_{UV}+A_{UV})}{2.5}} \quad (1.4)$$

where SFR is the star formation rate in solar masses per year, M_{UV} is the absolute UV magnitude, and A_{UV} is the UV dust extinction term.

1.2.1 SFR vs Stellar mass

A plot of SFR vs stellar mass (M_*) tells us how “active” a given galaxy or population of galaxies is. Normal galaxies like our own Milky Way ($M_* \sim 10^{11} M_\odot$, $SFR \sim 1 M_\odot \text{yr}^{-1}$) tend to lie somewhere in the middle. Star-bursting galaxies go higher and quiescents go lower on the plot.

The existence of a strong correlation between SFR and stellar mass of galaxies was first established based on the vast number local galaxy statistics obtained from the Sloan Digital Sky Survey (Brinchmann et al. 2004). Further studies established the main-sequence where normal Milky-Way type galaxies lie (Daddi et al. 2007, Rodighiero, Daddi, et al. 2011).

Recent studies have quantified the scatter, slope, normalization, and turnover points, finding that these quantities depend upon the sample selection methods and tracers used to calculate the SFR (Whitaker et al. 2015, Tomczak et al. 2016, Katsianis et al. 2020). The SFR-stellar mass relation also evolves with redshift (Kurczynski et al. 2016, Pearson et al. 2018). Although the slope remains approximately constant, the intercept (normalization) increases with increasing redshift (Fig.8 Speagle et al. 2014).

Typical LAEs have stellar mass ($M_* \sim 10^{8-9} M_\odot$) and SFR of $\sim 10 M_\odot \text{yr}^{-1}$ (e.g.: Kusakabe et al. 2018, Guaita et al. 2011), making them high- z analogs of local dwarf galaxies. Compared to other star-forming galaxy populations, LAEs are observed to have higher SFRs. However, Hagen et al. 2016 find that not all LAEs fit into this picture; they, in fact, can have a very wide range of stellar masses (at least three dex or more).

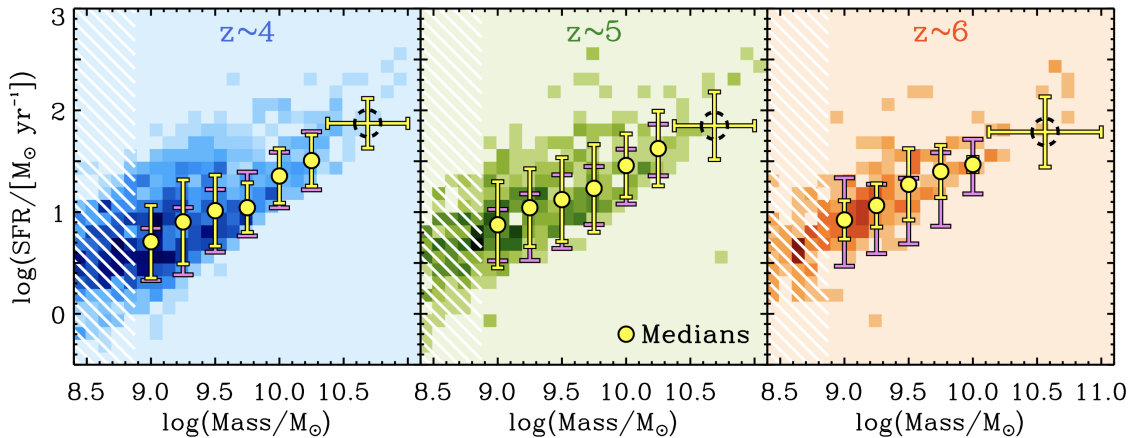


Figure 1.2: A log-log plot of star formation rate and stellar mass of galaxies at various redshifts. The darker-shaded regions indicate a higher number of individual objects in bins of stellar mass and SFR. Yellow circles with error bars are medians in bins of mass (purple error bars show the 68% range of errors from Monte Carlo simulations). The median SFR of a wider, high-mass bin is also shown by the dashed black circle. The white hatched regions mark the limit above which completeness effects become negligible. (Salmon et al. 2015)

Fig.1.2 shows a typical SFR-Stellar mass relation at $z \sim 4, 5$, and 6, taken from

Salmon et al. 2015. They find no evolution of the slope of the relation with redshift.

1.2.2 Galaxy Luminosity Function

The galaxy luminosity function (LF) gives the number of galaxies per magnitude per unit comoving volume of space. It tells us the distribution of galaxy luminosities at a given redshift, i.e., how many bright vs how many faint galaxies there are. The Schechter function (Schechter 1976) is a common empirical function used to describe the LF. The differential number of galaxies in a given luminosity bin is given by

$$n(L)dL = \phi^* \left(\frac{L}{L^*} \right)^\alpha e^{-L/L^*} \frac{dL}{L^*} \quad (1.5)$$

where L is galaxy luminosity, and L^* is a characteristic galaxy luminosity where the power-law form of the function cuts off. The parameter ϕ^* has units of number density and provides the normalization. α is the faint-end slope parameter. In terms of magnitude M , the Schechter function is

$$n(M)dM = (0.4 \ln 10) \phi^* [10^{0.4(M^*-M)}]^\alpha \exp[-10^{0.4(M^*-M)}] dM \quad (1.6)$$

where M^* is the characteristic absolute magnitude at normalisation point. Both α and ϕ^* are determined empirically for each population of galaxies by fitting the curve to observed data.

Fig.1.3 shows the evolution of the LF with redshift. Taken together, these curves show the buildup of galaxies from $z \sim 8$ to $z \sim 4$.

In practice, the observed LF is affected by the completeness of our sample (Johnston 2011). For instance, the phenomenon known as the Malmquist bias (Malmquist 1922) results in more bright galaxies than faint ones being detected. This gives rise to a completeness function that declines rapidly at faint magnitudes. Without proper corrections applied to compensate for the incompleteness of the sample, the LF would rise and then fall as our detected number counts fall, even as the true number counts continue to rise. At even fainter magnitudes, however, we expect a turnover in the true number counts as well, because it is difficult for very low-mass halos to host star-forming galaxies due to inefficiency of gas cooling (Liu et al. 2016).

Studies find that the $Ly\alpha$ LFs show three evolutionary trends: a monotonic increase from $z \sim 0$ to 3 (Deharveng et al. 2008, Oesch et al. 2010), no evolution from $z \sim 3$ to 6 (Herenz, Lutz Wisotzki, et al. 2019) and sometimes even $z \sim 3$ to 7 (de La Vieuville, Bina, et al. 2019), and a rapid drop beyond $z \sim 6$ to 7 (Ota et al. 2017, Bouwens, Illingworth, Oesch, et al. 2015). This results in the cosmic star formation history of the Universe peaking at cosmic noon (the classic “Madau plot”; Fig.8 of Madau and Dickinson 2014).

Furthermore, significant bright-end LF excesses are found beyond the Schechter function at $z \sim 2-3$, which can be explained by contamination from AGNs (Konno et al. 2016, Sobral et al. 2018). At higher redshifts up to $z \sim 6-7$, such bright-end LF excess

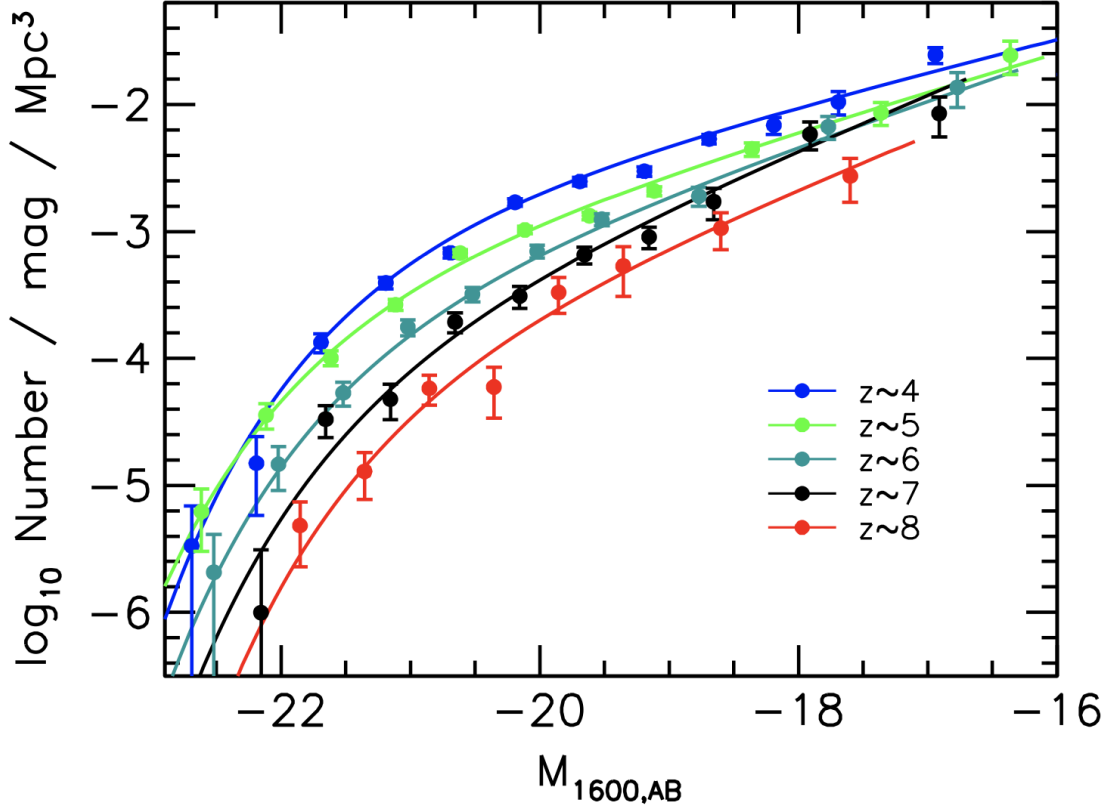


Figure 1.3: Galaxy LF across redshifts. The UV LF data points at $z \sim 4$ (blue solid circles), $z \sim 5$ (green solid circles), $z \sim 6$ (teal solid circles), $z \sim 7$ (black circles), and $z \sim 8$ (red solid circles) represent the average of all the galaxies in a given magnitude bin. The solid curves plot the Schechter fits to these points (Bouwens, Illingworth, Oesch, et al. 2015).

features are not clearly found, probably because the number densities of AGNs decrease with increasing redshift (Ouchi, Ono, and Shibuya 2020).

So far, we have discussed general observable properties of galaxies and what they mean in physical terms. In the next chapter, we will consider the curious case of compact objects, and try to discern whether the origin of this compactness is rooted in observation or reality.

Chapter 2

Compact Objects

The sources we study in this project have observed sizes of only a few kpc across, which makes them compact objects relative to other normal and star-forming galaxies at similar redshifts. This could be because they are truly compact, or because our observations are only able to pick up the compact part of a larger structure.

In the former case, it would be interesting to understand the physical origin of the compactness - how do they form and evolve, and how do they fit in to our understanding of galaxies and galaxy evolution over cosmic time?

In the latter case, it would be useful to know which part of our observations is responsible for creating this false narrative. We can then update the design of our detection (improving spectral and spatial resolution, increasing the depth and width of our surveys, etc.) and analysis methods (e.g.: developing models that can fit the morphology and photometric flux more accurately) so that the data can better reflect reality.

Either way, it is important to critically and thoroughly examine our observations and observation methods. Hence, in this chapter, we look into the literature on high- z observations of compact objects, and investigate potential reasons for compactness.

2.1 Observational Origin for Compactness

Observations at high- z suffer from several limitations that may affect our interpretation. We discuss a few relevant issues below, especially for high- z $Ly\alpha$ observations.

2.1.1 Dust and the Nature of $Ly\alpha$

$Ly\alpha$ is a resonant line, which means that it can be absorbed and re-emitted several times on its way out of a galaxy. A $Ly\alpha$ photon has exactly the energy required for an electron to transition between ground state and first excited state of H atom. If

such a photon is absorbed by a H atom, the atom is excited into the first energy state. When the atom de-excites back to ground state, the absorbed photon is re-emitted, but in a completely different direction than the one it came from initially. This is called resonant scattering Larsen 2021.

Considering that most of the Universe is neutral H, $Ly\alpha$ photons rarely make it very far before they encounter a H atom, which means that they have to “random walk” out of a galaxy (in both physical and frequency space - Osterbrock 1962) being absorbed and re-emitted over and over again, and in a different direction each time. It takes a very long time and distance for photons to escape the galaxy in this way, and on their way out, they form a giant glowing halo around the central source. All $Ly\alpha$ producing galaxies exhibit diffuse $Ly\alpha$ halos at least to some extent in space (Steidel et al. 2011).

In addition, the presence of dust can drastically alter observations at high- z . Especially in case of short wavelength observations as in UV continuum, we can lose a large fraction of the emitted flux to dust attenuation. The effect is even more pronounced in $Ly\alpha$ due to the increased path length from scattering.

Atek et al. 2008 find that in high HI column density environments, only 10% of emitted $Ly\alpha$ photons escape. For a galaxy with dust spread out in a disk, photons can escape more easily in the direction perpendicular to the disk than through it (Zheng and Wallace 2014, Verhamme et al. 2012). Therefore, If we’re seeing the galaxy face on, we might only see the emission and not the dust obstruction. This makes it difficult to correct for the dust extinction. Moreover, in this work, we use the dust extinction (A_v) estimates from EAZY (Sec.3.3.1) to calculate our UV SFRs (Eq.1.4). These estimates are only as reliable as the templates used to fit the object.

The combination of low escape fractions and high scattering could mean that all $Ly\alpha$ observations are, by nature, necessarily incomplete.

However, studies do show that the escape fraction of $Ly\alpha$ photons (and/or the ionizing photon production rate) from galaxies increases with increasing redshift from $z \sim 0$ to $z \sim 6$ (Hayes, Schaerer, et al. 2011, Khaire et al. 2016). Additionally, many find that LAEs seem to be consistently dust-poor compared to other UV-selected galaxy populations (S. Santos et al. 2020).

2.1.2 Slitless Spectroscopy

Traditionally, $Ly\alpha$ observations were carried out using narrow band (NB) imaging, where the observation is restricted in wavelength, or narrow slit spectroscopy, where it is restricted in spatial extent. Slit spectroscopy has the advantage of masking out most other bright sources in the observation field, but it requires some prior knowledge of the location and orientation of the source on the sky. NB imaging does not require knowledge of the exact spatial position; LAEs can be detected by their strong excess in the NB filter compared to nearby continuum filters. It does, however, require knowledge of the redshift of the source so that the filter can be placed at the appropriate wavelength of the emission line. This prior knowledge adds potential bias to our sample.

In addition, for objects that extend well beyond the size of the slit, or are highly asymmetric, slits result in a substantial amount of the flux being missed. Similarly, for objects where the exact redshift is not known beforehand, NB imaging may miss whole or part of the emission line. Unless we already know, prior to observation, exactly what the galaxy looks like, how extended it is, and the exact redshift it is at, it is very likely that our slit or filter placement will be at least slightly off.

Consequently, detection rates of giant nebulae are less than 10% using NB imaging at $2 < z < 3$ (Cantalupo et al. 2014, Hennawi, Prochaska, et al. 2015, Arrigoni Battaia et al. 2016), and no more than 50% for spectroscopic surveys, and the latter only works for smaller nebulae (North et al. 2012, Hennawi and Prochaska 2013, Fathivavsari et al. 2015).

Slitless surveys (Courbot et al. 2016, Bacher et al. 2016) have been developed and used to detect extended $Ly\alpha$ emission, although they do suffer from higher background flux level (Maseda and MUSE GTO Consortium 2020). Borisova et al. 2016 observed that the detection rate of $Ly\alpha$ halos near quasars at $z \sim 2$ was 100% with IFUs.

For this project, we use a technique that overcomes both the limitations of slit-spectroscopy and NB imaging, minimizing or even eliminating slit losses. Slitless grism imaging by the ACS instrument on HST can generate NB images over a continuous range of redshifts, i.e., a data cube of images of the galaxy across several filter bandpasses. This ensures that we capture all the flux in both the spatial and spectral dimensions, so that we can accurately study how compact or extended our sources really are.

2.1.3 Low SNR

Cosmological surface brightness dimming goes as $(1 + z)^{-4}$. Thus, sources at $z \sim 6$ appear over 2000 times less bright than similar sources at $z \sim 0$.

Even if low SNR is not the reason for the compactness observed in continuum (ref. Table.3.1), it may explain why the $Ly\alpha$ morphology is compact and clumpy.

At low- z , we see that most LAEs have an extended $Ly\alpha$ halo extending well beyond UV continuum emission (Hayes 2015, Leclercq et al. 2017, Wisotzki et al. 2018) due to scattering effects (see Sec.2.1.1). It has been suggested that this structure could even feed into the cosmic web through filaments (Bacon et al. 2021). Despite their size, it is very hard to observe these halos without very high SNR.

In our project, we do not necessarily detect any diffuse emission surrounding our compact objects (Sec.4.1.1). It could be that there is a diffuse, extended $Ly\alpha$ component around the objects that is simply invisible at our current depth and SNR even with IFUs (Sec.2.1.2). We examine this possibility in Sec.5.3.

2.1.4 IGM absorption

To first order, neutral H gas in the inter-galactic medium (IGM) at high- z erases the blue half, and transmits the red half of the $Ly\alpha$ emission line, reducing the total observed flux by a factor of 2. However, in reality, most of the $Ly\alpha$ is absorbed by inter-galactic neutral H by $z \sim 6$. Even post-reionization IGM at $z \sim 4$ can severely affect the transmission of $Ly\alpha$ flux owing to the infall of the neutral IGM onto galaxies (M. R. Santos 2004). Therefore, much more than half of the flux is lost, with the IGM transmitting only ~ 10 to 30% of all $Ly\alpha$ photons as shown in Fig.2.1.

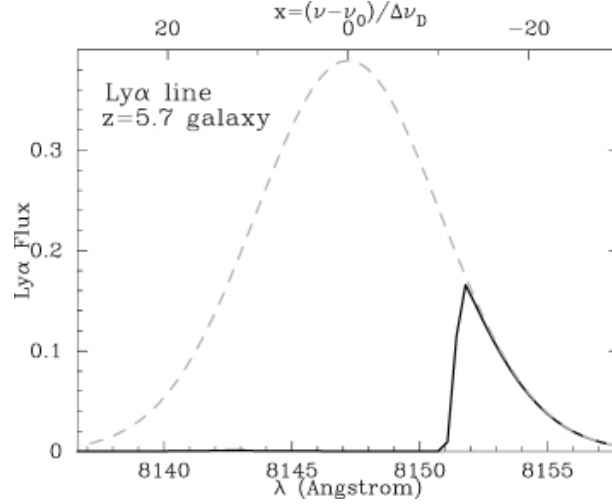


Figure 2.1: The effect of IGM absorption on the observed flux of the $Ly\alpha$ emission from a $z = 5.7$ star-forming galaxy. The intrinsic shape (dashed line) of the $Ly\alpha$ line is Gaussian. The solid represents the observed shape after IGM processing. Here, only $\sim 12\%$ of the $Ly\alpha$ is transmitted to the observer (Dijkstra, Lidz, and Wyithe 2007).

Our $Ly\alpha$ images may accordingly only paint an incomplete picture of the true nature of these objects, resulting in compact sizes that represent only the brightest parts of the source that were able to overcome the IGM absorption.

2.1.5 Clumpy Star-formation

Clumpy structures are identified in various high- z galaxies including some LAEs (Messa et al. 2019, Cornachione et al. 2018, Ritondale et al. 2019). Out of the galaxies studied in their sample at $z \sim 2.5$, Ravindranath et al. 2006 find that about 30% have multiple cores. Guo et al. 2012 similarly find 40% of their galaxies at $z \sim 2$ display massive clumps of \sim kpc sizes.

Hence, at higher z , just as in the case of diffuse halos (see Sec.2.1.3), our images could represent just one clump of star formation within a much larger structure.

Furthermore, as shown in Fig.2.2, feedback from young clumps can suppress further star formation elsewhere, ensuring that the rest of the galaxy remains invisible in UV and $Ly\alpha$.

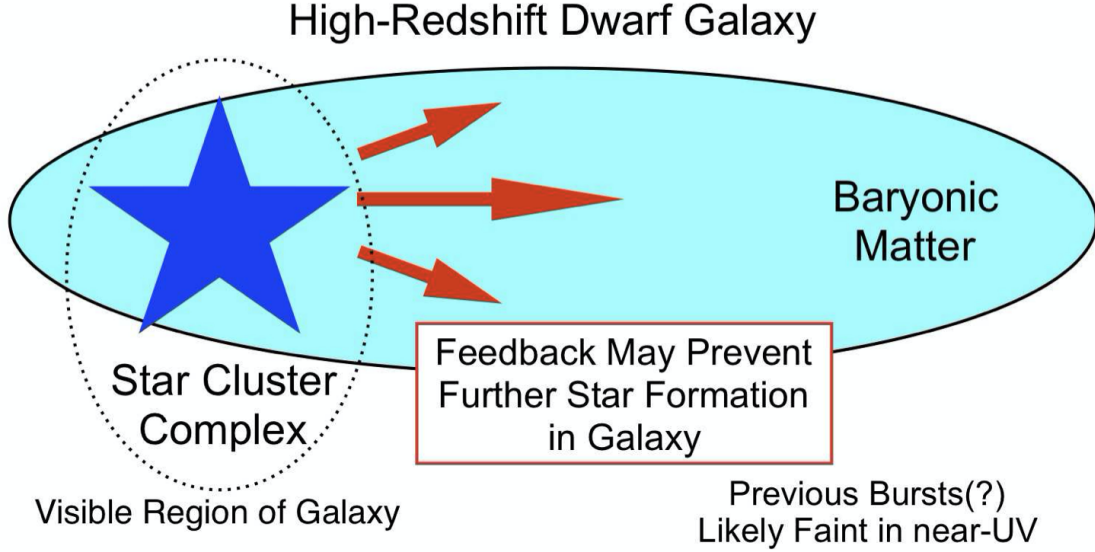


Figure 2.2: Cartoon depiction of a small, bright observable star-forming region within a larger galaxy invisible to our current telescopes (Bouwens, Illingworth, P. van Dokkum, et al. 2021).

2.1.6 AGN

Active Galactic Nuclei (AGN) appear as unresolved point sources (Mosleh et al. 2011) because we are only observing the central bright supermassive black hole that outshines the larger structure around it. This scenario is easy enough to test because AGN/Quasar objects will usually have complementary detections in X ray surveys. As we will see in Sec.5.1.3, this is indeed the case for 3 of our sources. In addition, we also place a limit (0.1 kpc) on the lowest object size that we consider “resolved,” thus making sure we steer clear of AGN.

2.2 Physical Origin for Compactness

There are many classes of objects such as clusters and associations of stars that are intrinsically small. It may be that our compact LAEs fall within one of these categories, i.e., they appear small because they *are* physically small.

2.2.1 High- z Galaxies

Studies show that galaxies at high- z were more irregular than local galaxies. This was first noted in early HST observations probing rest UV (e.g. Griffiths et al. 1994, van den Bergh, R. G. Abraham, Ellis, et al. 1996, Driver et al. 1998), and radio data (Windhorst et al. 1995). By the 2010s, the idea was well established (Conselice 2014, Huertas-Company et al. 2016). For example, Mortlock et al. 2013 visually classify and study the morphology of 1188 galaxies with $M_* \geq 10^{10} M_\odot$ and $z \sim 1$ to 3 in UDS field.

Approximately 40% of the galaxies are classified as disturbed galaxies at $z \sim 2.5$ to 3 compared to only 10% at $z \sim 1$.

Although there is some evidence that the irregular appearance of high- z galaxies is due to observational limitations, especially at the very highest redshifts beyond $z \sim 6$ (Jiang, Egami, et al. 2013), the general consensus is that it is indeed an intrinsic feature of early galaxies. That is to say that galaxies were truly more irregular because they were still in the process of formation (Cowie, Hu, and Songaila 1995).

Even early studies (e.g.: R. Abraham et al. 1996, van den Bergh 2002) realized that the conventional Hubble system no longer provides an adequate description of the morphological characteristics of a high fraction of galaxies at low magnitudes and high redshifts. The faintness and small angular size means that more subtle features, such as spiral arms, rapidly disappear with increasing redshift, leaving only the brightest galaxy components detectable (Barden, Jahnke, and B. Häußler 2008).

In addition, high- z galaxies display higher star formation rates compared to local analogs (Rodighiero, Cimatti, et al. 2010, Mortlock et al. 2013). Galaxies in general were much more extreme and vigorous than their mellow present-day counterparts.

Given this, it may be unsurprising to find bright compact objects at high- z ; perhaps they are simply very young galaxies or galaxy fragments that have not fully formed yet.

2.2.2 LAEs

It has been known since early HST observations such as Pascarelle et al. 1996 that LAEs display compact continuum morphologies. Deep HST extra-galactic legacy data have indicated that LAEs have half light radii of $r \sim 1kpc$ on average in rest-frame UV and optical stellar continuum (Malhotra, J. E. Rhoads, et al. 2012, Paulino-Afonso et al. 2018, Shibuya et al. 2019). It was observed that although sub-structures appear in some cases, the main stellar components of LAEs have “disky” radial surface brightness profiles with a Sérsic index of $n \sim 1$ (Gronwall et al. 2011, Taniguchi et al. 2009) similar to LBGs.

To explain the approximately constant typical sizes of LAEs over a wide span of redshifts, Malhotra, J. E. Rhoads, et al. 2012 suggested that the compact size is a required physical condition for a galaxy to become an LAE rather than a mere coincidence. Some other studies (Jiang, Egami, et al. 2013; Paulino-Afonso et al. 2018) and analytic calculations on morphologically compact conditions for Lyman continuum leakers such as Cen 2020 complement this picture.

However, Shibuya et al. 2019 argued that LAEs in a given range of UV luminosities do in fact show size evolution with redshift as $(1+z)^{-1.37}$, similar to the evolution of LBGs. Between $z = 6$ and 2, the size evolves by a factor of 3. It has also been suggested that size evolution differs between brighter and fainter galaxies (e.g., Bouwens, Illingworth, Oesch, et al. 2015, Finkelstein et al. 2015)). Shibuya et al. 2019 suggest that the no evolution results may be erroneously obtained due to the large range of luminosities

of the samples studied. Faint continuum LAEs with smaller sizes damp the evolution observed (Leclercq et al. 2017).

Perhaps this means that bright LAEs at high- z are intrinsically small and compact by nature.

2.2.3 Super Star clusters

Globular Clusters (GCs) in the local Universe often constitute of very old stellar populations that presumably formed in one or two large, nearly instantaneous bursts around the redshifts we're looking at. Kikuchihara et al. 2020 claim that low-mass galaxies ($M_* \sim 10^6 - 10^7 M_\odot$) at $z \sim 6 - 9$ can evolve to have stellar masses comparable to those of GCs in the Milky Way by $z \sim 0$.

Several studies have observed gravitationally lensed super star clusters and potential proto-GCs at high- z with sizes 100 pc and under (Vanzella, Calura, Meneghetti, Castellano, et al. 2019, Vanzella, Castellano, et al. 2017, Vanzella, Calura, Meneghetti, Mercurio, et al. 2017). Some of these objects are as small as 9 pc across, but the largest of the star cluster complexes can be up to 1 kpc across (Bouwens, Illingworth, P. van Dokkum, et al. 2021). Their derived stellar masses are $M_* \sim 10^6 - 10^7 M_\odot$.

Although without the magnification from lensing, it is not possible to spatially resolve sources with effective radii lower than ~ 100 pc at $z > 3$, a few of the compact sources studied in this work may still be candidates for star cluster complexes, super star clusters, or even proto-GCs, especially if they undergo some form of mass loss (through tidal stripping, gas expulsion following supernova events, etc.) as they evolve over cosmic time to $z \sim 0$ (Conroy 2012, Bastian and Lardo 2015).

If we really are looking at proto-GCs at high- z , we expect them to be very compact indeed.

In the following chapters, we apply several common analysis methods to our data to understand the nature of these objects in more detail, and answer some of the questions raised here. For instance, comparing the morphological properties of LAEs with those of LBGs when both populations are detected using the same observational methods can help us see if LAE morphology is intrinsically different from LBGs. The same applies for other astro-physical properties such as stellar mass and SFR. As another example, comparing the $Ly\alpha$ line morphology of a high- z LAE with its continuum morphology can tell us how the gas and stars are distributed in the LAE. We can then compare this in turn with a local LAE analog, and thereby deduce if and how the local LAE evolved from the high- z one. These are indeed the tests we apply in the next few chapters.

We use the Planck 2015 cosmological model (Planck Collaboration et al. 2016) with $H_0 = 67.8 \text{ km s}^{-1} \text{ Mpc}^{-1}$, a matter density parameter $\Omega_m = 0.308$ for all our distance calculations.

Chapter 3

Methods

In this chapter, we present an overview of the data used in this project, and the methods applied to analyze the morphology and flux of each source, with specific focus on the properties of the sub-sample LAEs with $Ly\alpha$ detection.

Firstly, we perform $Ly\alpha$ line and continuum morphology fitting with GALFIT on IFU thumbnail cutouts from 3D HST data to compare visual morphological characteristics (radius, Sérsic index) of line vs continuum and sub-sample vs parent sample.

Next, we plot Spectral Energy Distributions with EAZY (G. B. Brammer, P. G. van Dokkum, and Coppi 2008) using archival multi-wavelength photometric fluxes from Skelton et al. 2014 to derive astro-physical properties (stellar mass, UV SFR), and once again, compare sub-sample and parent sample.

The goal is to probe the sites of star-formation, AGN, stars, and gas separately, so as to identify properties that are unique to LAEs or those that can help us distinguish the sub-sample of LAEs from the parent sample of LBGs.

3.1 Data

For the morphological analysis, we use ACS/G800L grism spectra from HST that were taken as part of the 3D HST program in the optical-NIR wavelengths ($< 1\mu m$). We also use the Skelton catalogs (Skelton et al. 2014), which contain photometric flux data in filters across the electromagnetic spectrum (0.5 to $8\mu m$), to plot the SEDs.

3.1.1 Fields and Filters

The sources used in this work are from 4 of the 5 Cosmic Assembly Near-infrared Deep Extragalactic Legacy Survey (CANDELS) fields (Fig.3.1): the Great Observatories Origins Deep Survey-South and North (GOODS-S and GOODS-N) fields, the All-Wavelength Extended Groth Strip International Survey (AEGIS or EGS, a deeper

sub-field), and the UltraDeep Survey (UDS), the Cosmic Evolution Survey (COSMOS). These are among the most well studied patches of the sky in the history of Astronomy. Taken together, these 5 fields occupy ~ 600 square arcminutes on the sky, where some of the deepest observations of the Universe were generated.

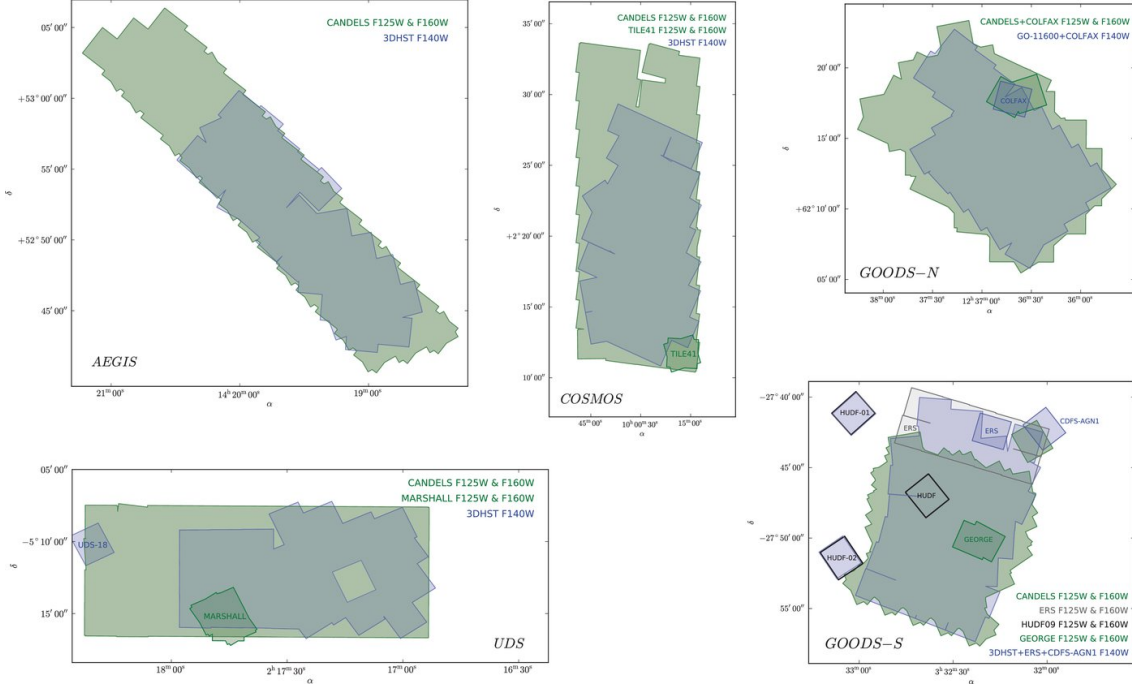


Figure 3.1: The footprints of all 5 CANDELS fields on the sky (Skelton et al. 2014)

In this work, the field names are shortened to a single letter that precedes the unique 5 digit ID of each source: s for GOODS-S, n for GOODS-N, e for EGS, and u for UDS. For instance, **s**_43831 is a source in the GOODS-S field with the unique HST id number 43831.

Two different HST filters are used to observe the sources: F850LP for GOODS-S and GOODS-N, and F814W for EGS and UDS (see Fig.3.2).

3.1.2 HST Grism Data

The continuum and $Ly\alpha$ line maps used in this project were all obtained using HST's G800L slitless grism on the Advanced Camera for Surveys (ACS) on HST. The use of slitless grism spectroscopy removes the need for potentially biasing photometric preselection or slit masks (Sec.2.1.2). ACS/G800L produces maps of every source at every wavelength with a spectral resolution of $R \sim 100$, covering the wavelength range $0.5 < \lambda < 1\mu m$. We utilize the data from several surveys conducted with ACS/G800L: 3D-HST, an optical-NIR spectroscopic survey covering all 5 CANDELS survey fields, along with additional very deep data from the GRAPES (N. Pirzkal et al. 2004) and PEARS (Straughn, Meurer, et al. 2008, Straughn, Norbert Pirzkal, et al. 2009) surveys in the GOODS fields (see Sec.3.1.1 for specifics of the fields). The spectra thus obtained were reduced and analyzed following the procedures described by Abramson et al. 2020.

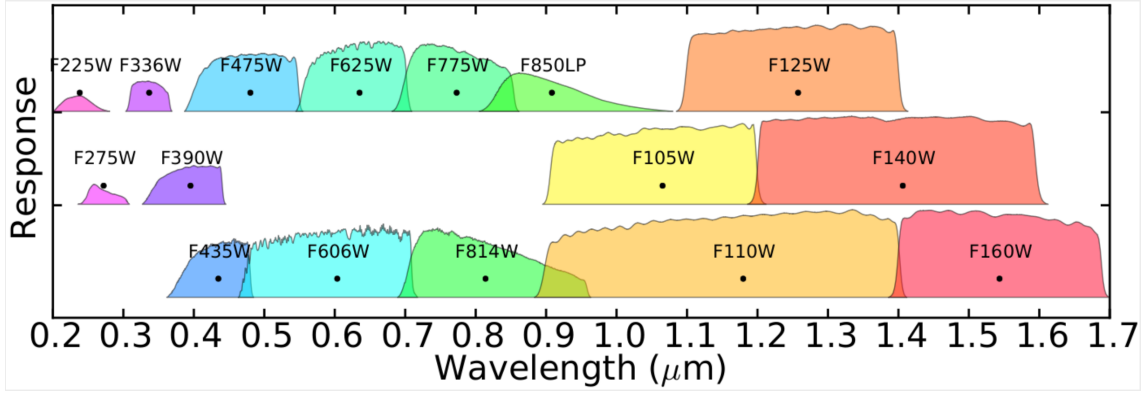


Figure 3.2: HST filters at different wavelengths, showing the transmission as a function of wavelength from UV to NIR (Jouvel et al. 2014). Note in particular the filters used in this work: F850LP and F814W for grism data, and F125W, F140W, and F160W for Skelton catalog data.

Fig.3.3 shows the 1D and 2D grism spectra extracted at the RA and Dec coordinates of one of our sub-sample sources: `n_16335` (criteria for sub-sample selection detailed in Sec.3.1.5).

Emission lines were extracted from the spectra using the Grism Redshift and Line Analysis tool (GRIZLI; G. Brammer 2019). $Ly\alpha$ line maps were produced by combining pointings of varying depths and position angles from all the above mentioned surveys to create very deep exposures (total exposure time as high as $\sim 58,000$ s for some targets).

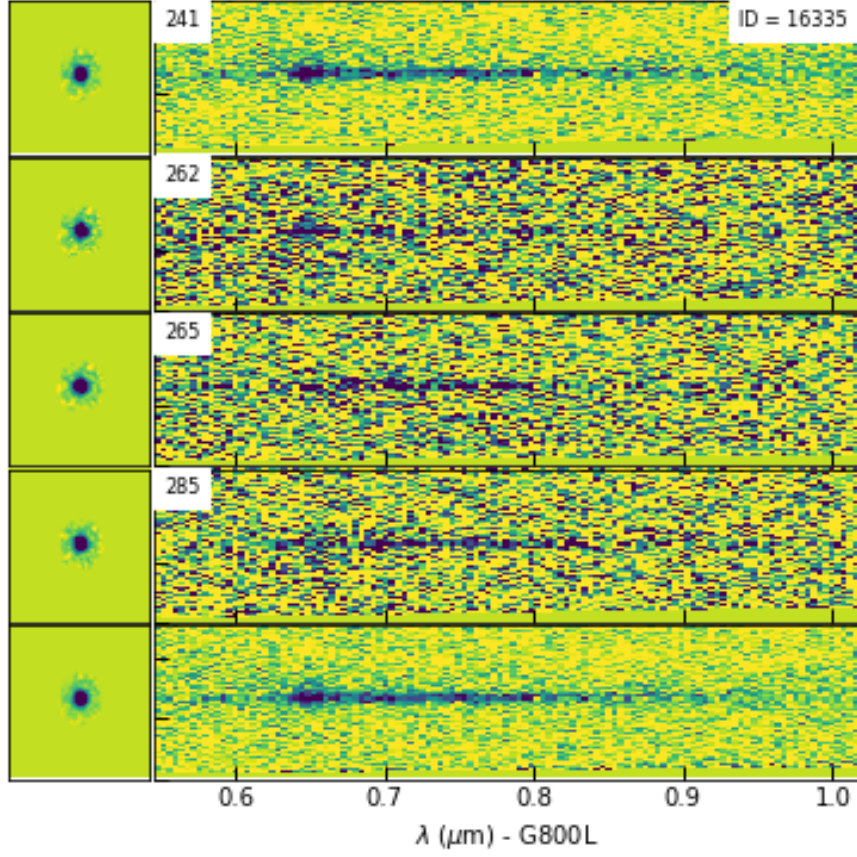
3.1.3 Skelton Catalog

The Skelton catalog consists of photometric fluxes across wavelengths from 0.5 to 8 μm for sources in the 5 CANDELS fields (Skelton et al. 2014). It spans the entire area covered by the HST F125W, F140W, and F160W filters, and includes data from an array of ground and space based telescopes including HST, Spitzer, Subaru, CFHT (Canada France Hawaii Telescope), VLT (Very Large Telescope), and many more.

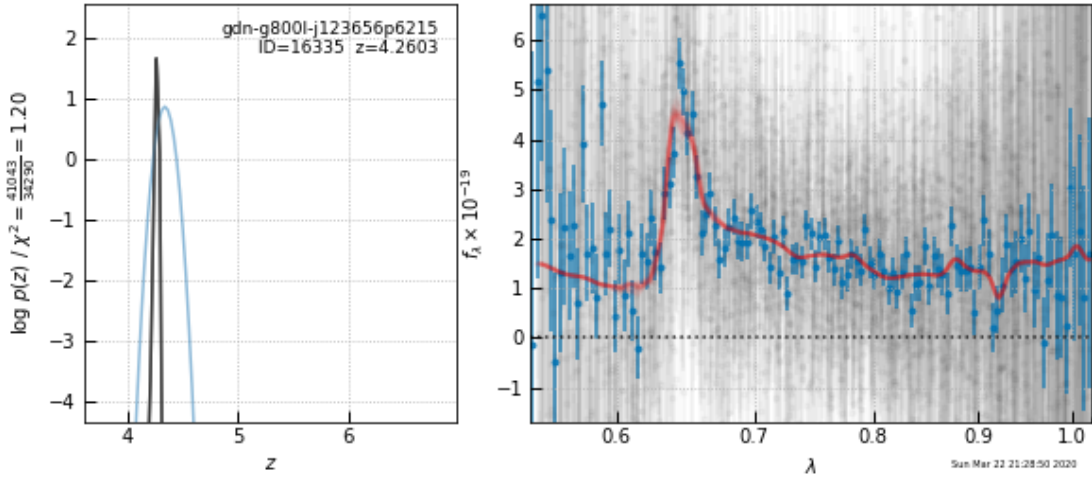
3.1.4 Parent Sample Selection

We first identified literature discussing large surveys of potential LAEs in the 5 CANDELS fields. Next, we combined (simple end-to-end stacking) the corresponding publicly available catalogs, including VANDELS (VIMOS (Visible Multi-Object Spectrograph) survey (McLure et al. 2018) of the CANDELS fields), several MUSE (Multi Unit Spectroscopic Explorer) survey catalogs (Herenz, Urrutia, et al. 2017), 3D-HST, and others. Note that some of these catalogs such as VANDELS and MUSE contain spectroscopic redshifts, whereas others only include photometric redshifts.

Then, we made a selection on this combined dataset to only include objects



(a) 2D spectrum extracted using the G800L grism in different filter bandpasses



(b) In the right panel is shown the 1D grism spectrum showing the $Ly\alpha$ emission line in units of $erg/s/cm^2$. The blue dots with errorbars are the flux data points and the red line is the best fit curve for the emission line. In the left panel is the posterior distribution for redshift associated with this extraction.

Figure 3.3: An example grism spectrum for n.16335. Top panel shows the 2D spectrum. At the bottom is the 1D spectrum along with posterior distribution for redshift.

that could potentially have $Ly\alpha$ detection in the wavelength range covered by the G800L

grism. This corresponds to $0.55 < \lambda < 1\mu m$, which translates to $\sim 3 < z < 7$. We further excluded sources that do not have reliable redshifts based on the redshift flags specified in the original catalogs. Additionally, we extracted grism spectra at the RA and Dec co-ordinates specified in the above catalogs, and rejected sources that had problematic grism exposures. We also had to exclude results in the COSMOS field due to data access issues. Finally, after all these cuts and exclusions, we ended up with a sample containing 1060 sources.

3.1.5 Ly α Detection

The SNR was calculated for *Ly α* images of all 1060 sources using the `sum_circle` function of `sep`, a source extraction library for Python (Barbary et al. 2016). The sigma image (discussed in Sec.3.2.3) was passed as the uncertainty. The calculation area was limited to a 6 pixel radius around the center of the thumbnail image, (corresponding to coordinates (60,60) in a thumbnail with dimensions 120x120 pixels), so that edge effects could be minimized.

Source	RA	Dec	z	Continuum SNR	<i>Lyα</i> SNR
s_17357	53.1744	-27.8674	3.62	344.16	27.90
s_21181	53.12439	-27.85169	3.68	51.42	13.06
s_18207	53.27	-27.86128	4.87	67.06	9.92
s_12390	53.07886	-27.88416	5.55	59.74	9.04
n_16335	189.09677	62.20985	4.26	33.85	8.78
n_39376	189.07953	62.31533	5.43	26.60	8.20
n_29365	189.39185	62.26475	6.46	175.60	7.46
s_44106	53.16947	-27.76565	4.67	20.82	7.24
e_06005	215.06541	52.89857	5.63	69.37	5.86
n_16708	189.44406	62.21157	4.99	29.51	5.66
s_26144	53.22516	-27.83362	4.41	109.76	5.64
s_36953	53.1438	-27.79094	4.80	14.23	5.58
e_18484	214.84113	52.78406	4.30	93.54	5.55
n_31351	189.20738	62.27347	6.11	36.99	5.55
s_43831	53.16741	-27.76688	4.06	26.58	4.83
s_17197	53.22086	-27.86499	4.56	110.25	3.32
s_33531	53.16265	-27.80368	4.51	15.83	2.73

Table 3.1: List of sub-sample sources along with their RA, Dec, redshift, and SNR for the Continuum and *Ly α* images (sorted by *Ly α* SNR).

Generally, *Ly α* is considered “detected” for images with $SNR > 3$. However, in our sample, several images with hot pixels and telescope artefacts complicated identification by SNR alone. This is exemplified by s_51796 shown in Fig.3.4b. The SNR for this image within a 6 pixel radius around the center (60,60) came out to be 9.63. But it clearly is an observational artefact, and not an actual detection. The truly high SNR source s_18207 with $SNR = 9.92$ is also shown for comparison.

In total, 24 sources were identified as $SNR \geq 5$, but only 14 of these were true

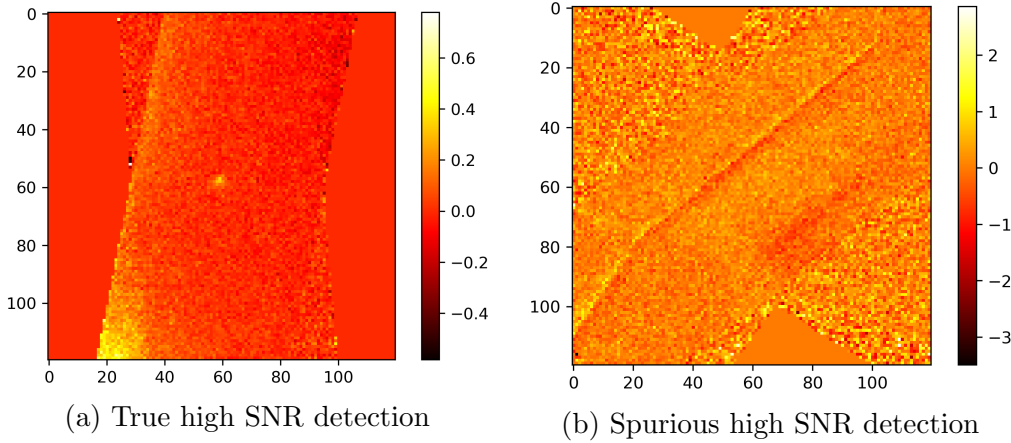


Figure 3.4: Thumbnail images from our data showing the $Ly\alpha$ line maps. On the left is shown a source with truly high SNR (9.92) for `s_18207`, and on the right, a spurious high SNR (9.63) detection for `s_51796`.

detections (as we will see below). For $SNR \geq 3$, 95 more sources were identified of which only 2 those were true detections. Hence, when going by SNR alone, the accuracy of detection is 58.3% at $SNR \geq 5$ and only 13.4% at $SNR \geq 3$.

It was, therefore, necessary to go through the images manually to detect faint sources “by-eye” and to reject spurious detections. Instead of doing this for the entire sample, we opted to perform manual selection only for the sources that either had a high $Ly\alpha$ SNR as calculated above or a more reliable redshift measurement as quantified by the `bic_diff` parameter in the HST grism catalog (Abramson et al. 2020).

The 17 sources were thus identified as $Ly\alpha$ detected using a combination of SNR measurement and by-eye selection: 10 from GOODS-S, 5 from GOODS-N, and 2 from EGS. Table 3.1 lists the SNR for each of the 17 sub-sample sources for both continuum and $Ly\alpha$ images along with their RA and Dec co-ordinates from HST data, and the redshift (from grism spectroscopy where available; otherwise photometric redshift from literature is provided).

Sample	GOODS-S	GOODS-N	EGS	UDS	Total
Full Skelton	50507	38279	41200	44102	174088
GALFIT parent	619	192	73	176	1060
EAZY parent	550	192	73	176	991
Sub-sample (GALFIT and EAZY)	10	5	2	0	17

Table 3.2: A breakdown of the number of sources in each field for the samples used in this work.

Table 3.2 shows a breakdown of the samples used in this work into their constituent CANDELS fields. The GALFIT parent sample is the main sample of 1060 sources obtained as discussed in Sec.3.1.4. The GALFIT sub-sample consists of a subset of the parent where $Ly\alpha$ was detected as described in Sec.3.1.5. Photometric fluxes from the Full Skelton catalog were used to make the SED fits in Sec.4.2.1, and hence, we could only fit SEDs for the part of our sample that had data in these catalogs; we had to exclude 69

GOODS-S sources from our main 1060 sample that were absent in the Skelton catalog. Therefore, the EAZY parent sample is 69 GOODS-S sources short of the GALFIT parent sample. The EAZY sub-sample is the same as the GALFIT sub-sample.

The redshift distribution of the full sample is shown in Fig.3.5.

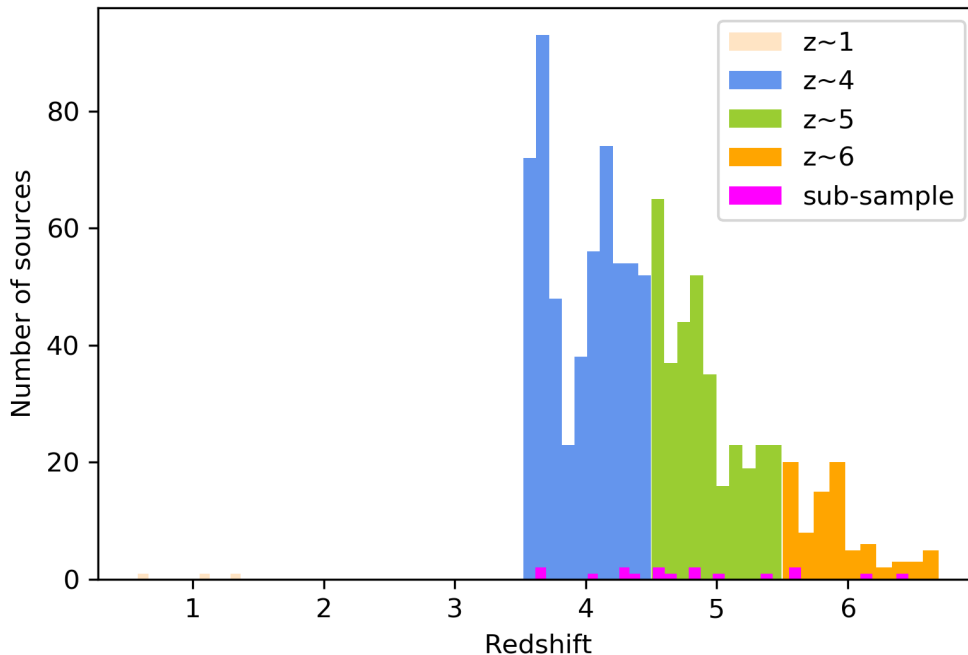


Figure 3.5: Distribution of the full sample redshifts. The majority of the sample - 564 sources - is at $z \sim 4$ (blue), followed by 337 at $z \sim 5$ (green), and 87 at $z \sim 6$ (orange). Only 3 sources are at $z \sim 1$ (cream). Sub-sample is shown in magenta.

3.2 Sérsic Model Fitting with GALFIT

We used GALFIT (Peng et al. 2010) to fit the $Ly\alpha$ line and continuum morphology for the sub-sample, and only continuum morphology for the rest of the parent sample with no line detection.

3.2.1 GALFIT Description

GALFIT (Peng et al. 2010) is a two-dimensional morphology fitting algorithm based on χ^2 minimization designed to extract structural components from galaxy images. It can simultaneously fit a galaxy with an arbitrary number of components, and has many built-in analytical models which can be used to fit each of these components.

3.2.2 Fitting Procedure

We initially began by individually fitting each galaxy with 1, 2, and more than 2 components. We tried varying combinations of the available model profiles such as Sérsic, PSF, Gaussian, King, Nuker, and Fermat.

We found that multiple-component fits usually did not produce significantly cleaner residuals or better reduced χ^2 . Rather, we found that the Sérsic profile did the best job of capturing the characteristic size of a given source, both for continuum and line images, and letting GALFIT find the Sérsic index yielded better results than if we set it at a fixed value beforehand.

With this optimal model in hand, we employed a Python wrapper script to batch-fit all the galaxies in our sample with a single Sérsic (with variable Sérsic index) to obtain characteristic measurements of morphology.

However, there were some exceptions where multiple components were necessary, e.g.: `s_17197` for which the continuum image fit best with 5 Sérsic components. The fits for each source are shown individually in Appendix A.

3.2.3 GALFIT Input

The GALFIT input file with the file extension “.feedme” initializes the fit. It contains initial guesses for the basic parameters: fit type, x and y coordinates, Sérsic index, half-light radius, axis ratio, and position angle among others.

It also initializes the number of components to be used for the fit. We use 2 components: one for the actual galaxy, and the other to set the background flux level, given as the “sky” component (Sec.3.2.3).

The filenames for the science, sigma, PSF, and mask images are also specified in the input file.

Images

Line images: The $Ly\alpha$ extension from the GRISM data was saved as a separate fits file to be given to GALFIT.

Continuum images: UV continuum cutouts were created from 3D HST grism data. These were also saved as separate fits files to be given to GALFIT.

PSF

PSF images were created from standard models for the appropriate HST filter projected onto each thumbnail position (Anderson and King 2000). The same PSF was

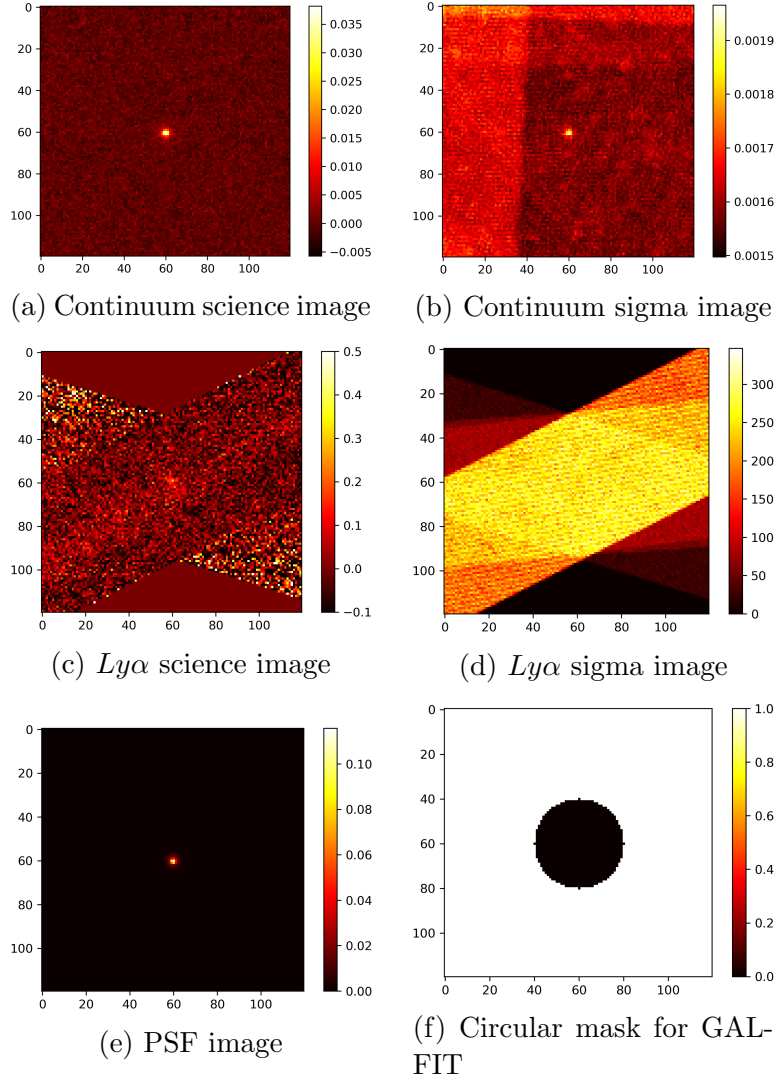


Figure 3.6: The images given as input to GALFIT to fit n_16335. Sub-figures a and c show the continuum and $Ly\alpha$ images, b and d the corresponding sigma images obtained as discussed in Sec.3.2.3, e shows the PSF image discussed in Sec.3.2.3, and f shows the circular mask within which GALFIT performs the fitting as explained in Sec.3.2.3. All flux units are in $10^{-17} \text{ erg/s/cm}^2$.

used for both line and continuum fitting.

Sigma image

Sigma Image was created by inverting the “WHT” weight extension associated with each science image in the grism data such that

$$\text{Sigma} = \frac{1}{\sqrt{\text{WHT}}}. \quad (3.1)$$

Mask

We created custom circular masks for both line and continuum images so that GALFIT only considers pixels if they have non-zero weight (i.e., finite sigma) and they are within a 20 pixel radius of the image center (60,60).

Fig.3.6 shows an example of the images given to GALFIT as input to perform continuum and $Ly\alpha$ line fitting for n_16335.

Aperture Magnitude

Aperture magnitude was calculated as

$$\text{mag} = -2.5 \log(\text{flux}) + \text{zeropoint} \quad (3.2)$$

where we determined the flux by summing over non-negative image pixels within a 6 pixel circular radius around image center (60,60), and the zeropoints are given in Table 3.3.

Field	Continuum Filter	AB Magnitude Zeropoint
GOODS-S	F850LP	24.84
GOODS-N	F850LP	24.84
EGS	F814W	25.94
UDS	F814W	25.94

Table 3.3: The zeropoints used for each filter and field to calculate aperture magnitude given as input to GALFIT (Zeropoint values taken from Koekemoer et al. 2011)

Sky Background Estimation

`skyback` is the GALFIT parameter for sky background flux. GALFIT can estimate the sky on its own from a given image, but that would introduce another free parameter. Especially for models with large Sérsic indices, there is degeneracy between sky background flux and flux from the source because of their extended wings (see Fig.1.1 and Häussler et al. 2007). Therefore, we chose to calculate the sky background separately and supplied it to GALFIT in the input file.

`skyback` was calculated as the median of the flux within an annulus with 6 and 15 pixel inner and outer radii respectively around the image center (60,60). The inner radius masks out the central pixels where the source is, and the outer radius masks out edge pixels in the image to create an annulus of pixels around the source where the sky background can be calculated. Within this annulus, we calculate the sigma clipped median (median value of the pixels within 3 sigma on either side of their mean value for the pixels within the annulus). The sigma clipping ensures that extreme outlier pixels (eg: cosmic ray hits, detector defects) are disregarded during median calculation.

Constraint file

In order to prevent GALFIT from searching through un-physical parameter space, we specify a set of constraints as detailed in Table 3.4. We included constraints for the x and y coordinates of the source, magnitude, axis ratio (semi-minor axis over the semi-major axis), and Sérsic index to ensure that the least squares fit converges onto the properties of the source in the center, without getting stuck in a local minimum. However, the downside to this practice is that if during fitting, GALFIT hits one of these constraints, it sometimes cannot “bounce back” into the allowed parameter space. Instead it fixes the current parameter at the limiting constraint value, and determines all other parameters based on this fixed limit, thus making the final fit problematic. These problematic fits can be seen in our output parameter plots with artificial “walls” where GALFIT hits the given constraints. Nevertheless, it was necessary to use constraints especially during batch-fitting where it is not possible to monitor each fit closely.

Parameter	Constraint	Comment
axis ratio (q)	0.5 to 1.0	absolute
half-light radius (re)	0.1 to 10	absolute
Sérsic index (n)	0.5 to 8	absolute
x position (x)	-4 4	relative
y position (y)	-4 4	relative
magnitude (mag)	-3 3	relative

Table 3.4: Parameters and their constraints given to GALFIT via the constraint file

The first column shows the parameter, the second gives the limits between which the parameter is allowed to vary while fitting, and the last column describes whether the limits are absolute, ie, “hard” constraints or relative to the value at which the fit was initialized in the input file (.feedme file).

For example, if the x position was initialized at the 60th pixel, the x coordinate of the final output fit is only allowed to be within the 56th and 64th pixels. On the other hand, the axis ratio of the final fit is only allowed to be within 0.5 and 1.0 regardless of what value it was initialized at.

The same constraints were given for other components if any.

3.3 SED fitting with EAZY

We fit SED templates to the photometric flux data using EAZY. We use the `fit_at_zbest` routine with best z being the HST grism redshift where available, and photometric redshift from literature otherwise.

3.3.1 EAZY Description

EAZY (G. B. Brammer, P. G. van Dokkum, and Coppi 2008) is a public software program that fits a set of galaxy SED templates to the observed photometry, providing photometric redshifts as well as other physical properties such as stellar mass, SFR, and A_v based on those templates. It is designed to produce high-quality redshifts for situations where complete spectroscopic calibration samples are not available.

The EAZY algorithm moves across a grid of redshifts or a single redshift defined by the user. At each redshift, it fits the best synthetic template spectrum obtained through linear combinations of a set of 12 built-in SED templates, which are population synthesis models. For each source in the catalog, it finds the best possible linear combination of these templates using χ^2 minimisation.

3.3.2 EAZY Input

The input to EAZY includes a catalog containing the flux of each source in filters ranging from UV to FIR, a translate file describing which flux column in the catalog corresponds to which filter, and a set of 12 galaxy templates. We also provide a list of parameters specifying the galactic extinction (0.0103), zeropoint (25), redshift and magnitude priors, etc.

We perform the photometric SED fitting at fixed z because we already have (in most cases) the more accurate spectroscopic redshifts in the catalog, and therefore do not require EAZY to find the best-fit redshifts. Instead, we use template fitting to obtain other properties of the galaxies such as the stellar mass and SFR.

Chapter 4

Results

In this chapter, we discuss the results obtained from our analysis with GALFIT and EAZY, and compare our findings with those from literature.

4.1 Results from GALFIT

4.1.1 GALFIT Output

The output from GALFIT is a .fits file with 4 extensions. The first extension is blank, the second is the input science image, the third is the model that was used to fit the science image, and the fourth is the residual leftover from subtracting the model from the science image. Due to the circular mask (Sec.3.2.3) and position constraints (Sec.3.2.3) given to GALFIT, it only fits the central bright source and ignores all the other sources in the rest of the image.

The fits and residuals for the continuum and $Ly\alpha$ for n_16335 are shown in Fig. 4.1 as an example. The fourth panel in both Fig.4.1a and Fig.4.1b shows the residual divided by the sigma image, so as to display it in terms of the number of standard deviations away from noise. A value of 1 on this image corresponds to 1 sigma confidence, 2 corresponds to 2 sigma confidence, and so on. The rest of the fits are attached in Appendix A.

The best-fit parameters obtained for this fit are given in Table 4.1. GALFIT also returns a value for the goodness of fit, χ^2 . The reduced χ^2 for this fit was 0.7699517 for continuum and 0.9983547 for $Ly\alpha$.

The characteristic continuum size is 0.9 pixels, which at the redshift of this source ($z \sim 4.26$) translates to 1.68 kpc, which is small but not unresolved. Moreover, this source wasn't found in any X ray catalogs (Sec. 5.1.3), which means that it is probably not an (luminous) AGN or Quasar. Hence, it is likely a compact LAE (see Sec.2.2.2).

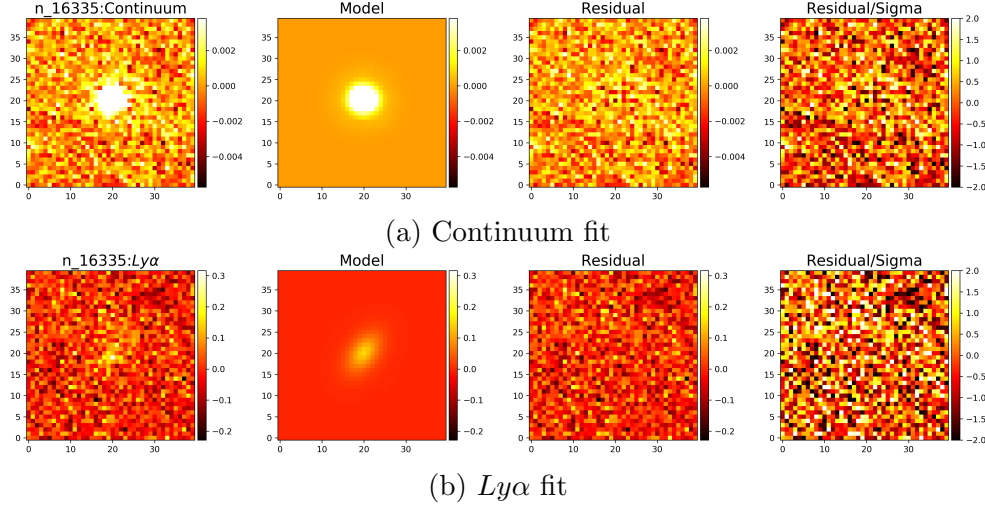


Figure 4.1: Images showing an example of GALFIT fit to `n_16335`. The first three panels show the .fits extensions from the GALFIT output imageblock: the input image of the source, the GALFIT model used to fit the input image, and the residual obtained by subtracting the model from the input image (Sec.4.1.1). The rightmost panel shows the residual divided by the sigma image.

Parameter	Continuum Fit		$Ly\alpha$ Fit	
	value	error	value	error
x position (pixels)	61.1504	0.0342	61.2486	0.2842
y position (pixels)	61.2400	0.0312	60.9727	0.3871
Magnitude	20.5545	0.0168	15.7770	0.1169
Radius (pixels)	0.9252	0.0514	4.0243	0.7690
Sérsic index	0.5000	0.3163	0.7221	0.4079
Axis ratio	0.6466	0.0715	0.5000	0.1082
Position angle (degrees)	-85.9800	8.7484	-36.6295	11.2221

Table 4.1: GALFIT output fit paramaters for `n_16335`

The $Ly\alpha$ radius, however, comes out to be over 4 pixels because the image looks wispy and spread out instead of having a definite, contained structure like the continuum image. Thus, GALFIT tries to fit the extended clumpy emission using a large radius. Although the residual looks clean, and the reduced χ^2 is close to 1, the fit is questionable. We need deeper data to accurately measure the $Ly\alpha$ morphology.

4.1.2 1D Surface Brightness Profiles

We estimated the 1D surface brightness profile for the continuum images using the `isophote` Python package. The resulting profiles for image, model, PSF, and residual for `n_16335` are shown in Fig.4.2 as a function of $a^{1/4}$, where a is the semi-major axis in pixels. We see that the model follows the image brightness closely until $a^{1/4} \sim 1.5$, which is around a 5 pixel radius, encompassing most of the light from the object. On

the other hand, the PSF is separate from both image and model. This tells us that the Sérsic model captures the central surface brightness better than a simple PSF. In other words, the object we're fitting is an extended Sérsic rather than a point source.

The profiles for the rest of the sources are attached in the Appendix A.

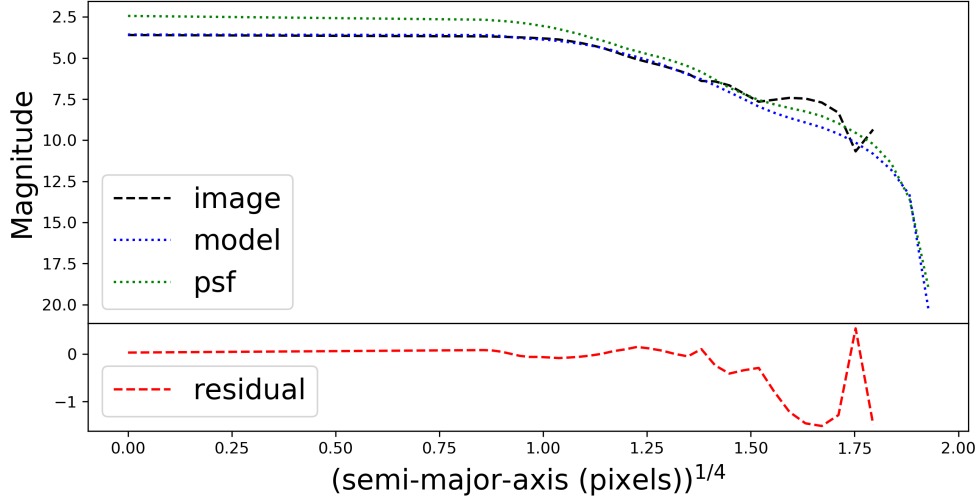


Figure 4.2: 1D surface brightness profiles for `n_16335`'s image (dashed black line), model (dotted blue line), and PSF (dotted green line) are shown in the upper panel, with residual curve (dashed red line) plotted in the lower panel.

4.1.3 Line vs Continuum Morphology

The derived radius for the continuum images is plotted against that from the $Ly\alpha$ line images in Fig.4.3 with the continuum image morphology used as data marker for each of the 17 sub-sample sources. The same plot of continuum vs $Ly\alpha$ radii is shown again in Fig.4.4, but this time, the data markers are represented with the $Ly\alpha$ morphology. The solid line indicates an identity line where the continuum and $Ly\alpha$ radii would be equal.

We see that for some sources, however, especially `s_44106`, $Ly\alpha$ radius is larger than continuum, which is unresolved. It might be that here we are picking up some of the diffuse, scattered light from the extended halo (see Sec.2.1.1).

Most other sources generally follow the one-to-one line. This is reasonable since both UV continuum and $Ly\alpha$ trace the young stars and star forming regions in a galaxy. However, it highlights the fact that we presumably do not have the depth required to observe the extended $Ly\alpha$ emission.

It is also clear that the continuum morphologies are much more distinct and contained, while many of the $Ly\alpha$ morphologies look amorphous. We likely require deeper data to create better line maps.

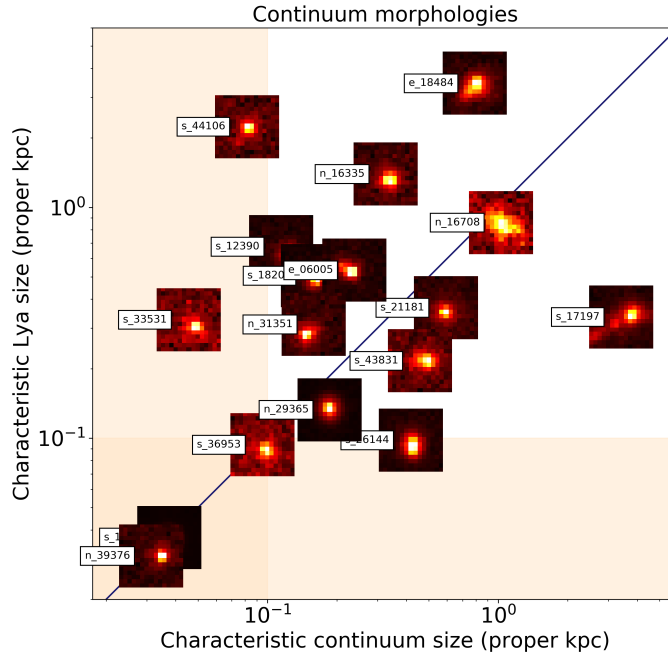


Figure 4.3: Derived galfit radii for continuum and $Ly\alpha$ line images with the data markers showing the continuum morphology. The purple line describes equal line and continuum radii. The cream colored shaded region indicates radii that are below our resolution limit of 0.1 kpc.

4.1.4 Spatial Offset between Line and Continuum

$Ly\alpha$ originates from the gas around O and B stars, while the UV continuum is emitted directly by the stars themselves, which means they should not be spatially offset from each other. However, $Ly\alpha$ scatters well beyond its location of origin (see Sec.2.1.1), which means it can indeed be offset from the continuum especially for galaxies with asymmetric gas reservoirs. Though in our case, we are unable to detect the scattered, diffuse light, so we do not expect to see an offset after all; the expectation value for the offset is about 1 pixel, which is $\sim 1kpc$. This is indeed what we observe in Fig.4.5, where we plot the offset between the $Ly\alpha$ and continuum source positions on the image as a function of the continuum radius.

Note that one pixel on our grism thumbnail images corresponds to 0.05 arcseconds, which at $z \sim 5$ would be $\sim 300pc$. Owing to the PSF convolution, GALFIT can estimate radii well below 1 pixel, but following a conservative approach, we choose not to trust derived radii $\leq 0.1kpc$. This is shown using the shaded area in all three plots Fig.4.3, Fig.4.4, and Fig.4.5.

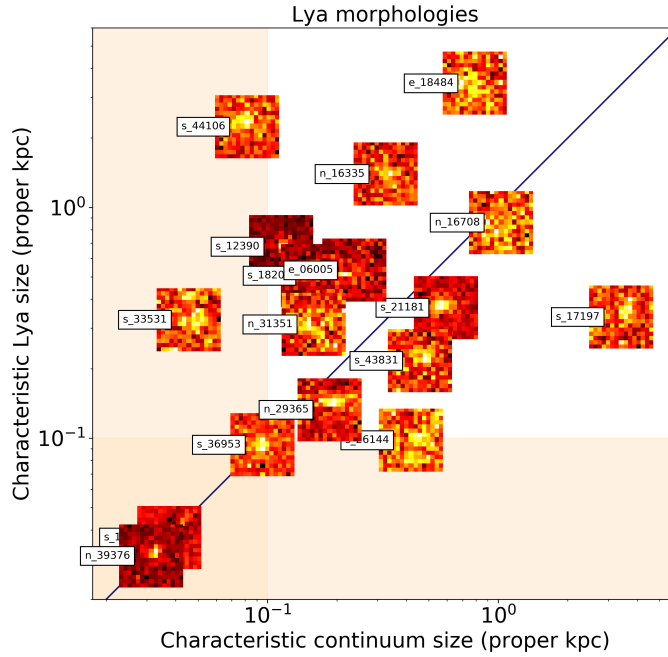


Figure 4.4: Same as Fig.4.3 but with the data points showing the $Ly\alpha$ morphology.

4.1.5 Comparison of GALFIT parent and sub-sample

Fig.4.6 is a pairplot of all GALFIT parameters, showing how they vary with each other in pairs. Also shown are the kernel density estimations (KDE) for each parameter indicating where on each plot most of the sample lies. It can be seen that the plots form “walls” where GALFIT hits the constraints provided (Sec.3.2.3). This is also reflected in the bimodality of the KDE plots. The Sérsic index, for instance, is boxed in between 0.1 and 8, and its KDE plot shows a larger number of objects at these two values.

The position angle has the most scatter, which is to be expected; there is no reason why galaxies would preferentially lie in one orientation over another on the sky. The axis ratio for the sub-sample is generally closer to 0.5 than 1, implying that these sources are more elongated than the parent population. Derived magnitudes are similar for sub and parent samples.

The most interesting result from this plot is for the radius. The sub-sample conspicuously fits with a smaller radius compared to the parent sample. This is in line with the observations of LAEs as discussed in Sec.2.2.2, especially the findings of Malhotra, J. E. Rhoads, et al. 2012. The converse does not hold true, i.e., there are several LBGs with compact continuum morphologies in our parent sample that do not exhibit $Ly\alpha$ emission.

Next, we investigate the redshift evolution of continuum size for sub and parent samples in Fig.4.7. Once again, we see that the average radius of continuum for the sub-sample is, in general, more compact than that of parent sample.

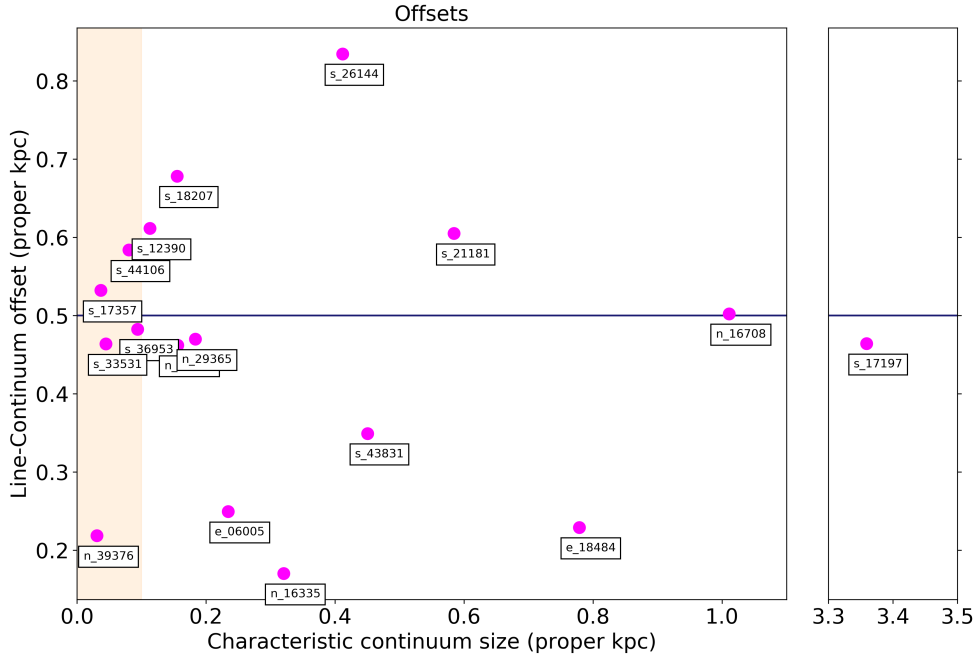


Figure 4.5: The $Ly\alpha$ line-continuum offsets as a function of the continuum radii. Again, the cream colored shaded region indicates radii that are below our resolution limit. The dark blue line shows the expectation value consistent with no offset, given the PSF size.

s_17197, the lone sub-sample data point at radius 10, is a noticeably extended source with an optimal fit involving 5 Sérsic components (Fig.A.4 in Appendix A). This is an exception to the generally small LAE continuum sizes. For this source, continuum radius is larger than the rest of the sub-sample, and also larger than its own $Ly\alpha$ radius. This is in contrast to the expectation of extended $Ly\alpha$ halos (with larger sizes than continuum) that were found in literature (Sec.2.1.3).

In Fig.4.8, we separate our sample by EAZY absolute magnitude (ref. Sec.4.2.1) into bright and faint bins in accordance with the analysis from Shibuya et al. 2019. We observe no clear evolution of the size with redshift in the bright bin, but see a slight decline in the faint bin. This is the opposite of findings from literature (Sec.2.2.2).

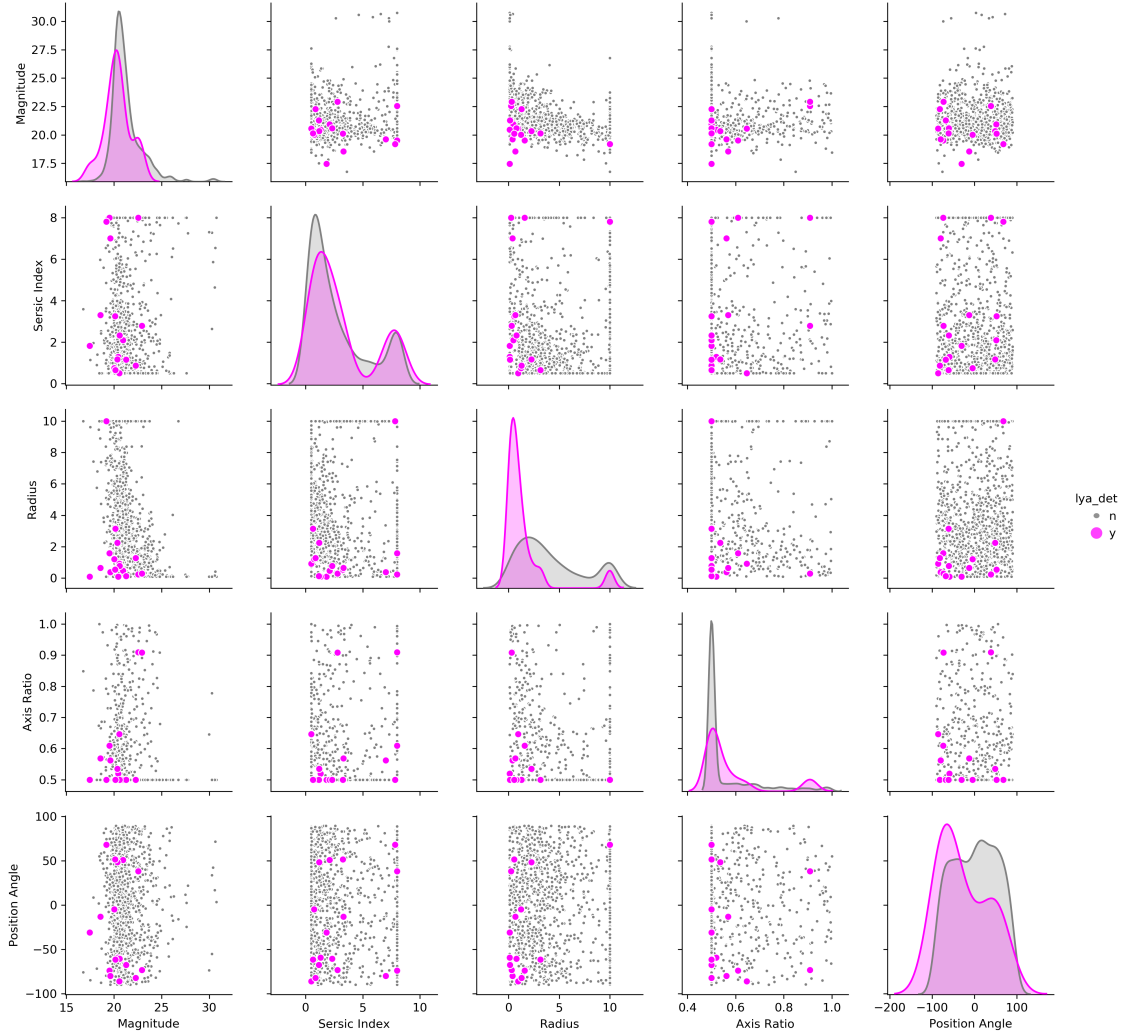


Figure 4.6: A pairplot of all parameters derived by GALFIT, along with the KDE plots for each along the diagonal. Magenta represents the sub-sample with $Ly\alpha$ detection, while grey is for the parent sample without detection.

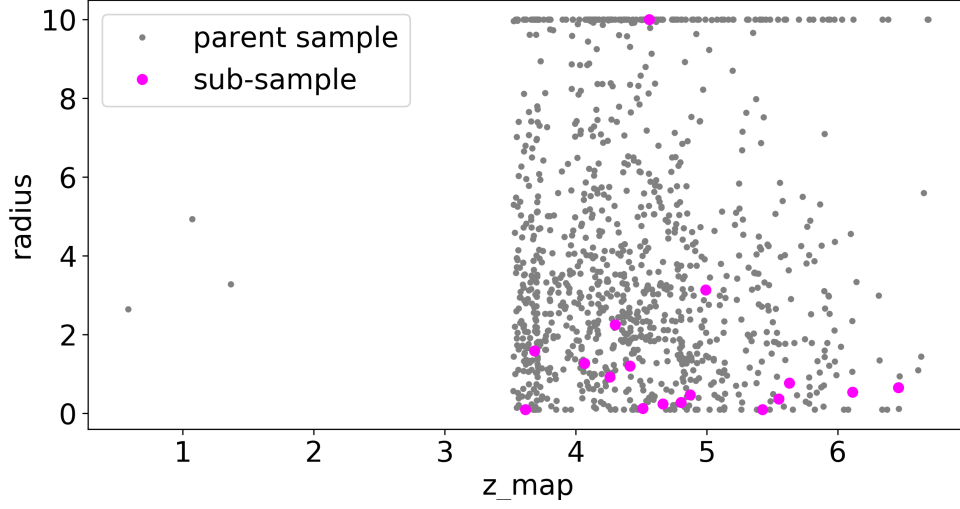
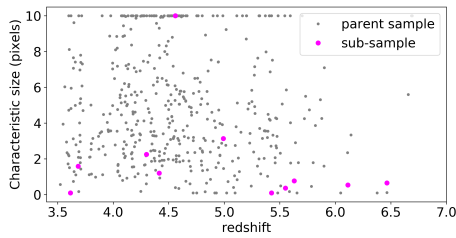
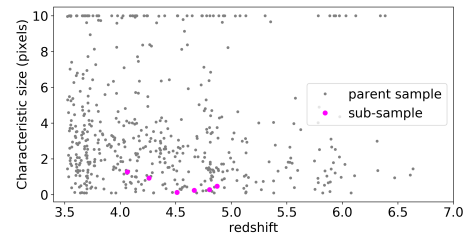


Figure 4.7: Derived galfit radii for continuum images as a function of redshift. It can be seen that the continuum radii for the sub-sample (magenta circles) are generally smaller than those for the parent sample (grey dots).



(a) Radius-redshift plot for bright bin



(b) Radius-redshift plot for faint bin

Figure 4.8: Same as Fig.4.7 but split into bright (< -21) and faint (> -21) bins by EAZY absolute magnitude. We find a slight decline in size with z in the faint bin.

4.2 Results from EAZY

4.2.1 EAZY Output

The output from EAZY is a table containing the best-fit properties such as the stellar mass, SFR, A_v , and absolute magnitude for each source in the input catalog.

It also outputs the fitted SED model as shown in Fig.4.9 for n_16335. Here, we see the peak of the $Ly\alpha$ emission at $\sim 0.7\mu m$. We also see that the fit follows the data points closely, and there isn't a large spread that usually arises from fitting dusty templates to data points with large uncertainties (Fig.A.21 in Appendix A). The best-fit stellar mass and SFR are $2.07 \times 10^9 M_\odot$ and $6.86 M_\odot yr^{-1}$ respectively. Comparing with the Milky Way, n_16335 is only a hundredth of the mass, but is converting gas to stars 9 times as quickly. This is consistent with what we expect for high- z galaxies (see Sec.2.2.1), especially for star-forming LAEs. In addition to the SED fit, EAZY returns the posterior probability of the redshift obtained from the fit. In the fixed redshift case, the latter plot is only a single vertical line at the given redshift, with a probability of 1. Note, however, that this does not mean the redshift is known with absolute certainty, because there is still the posterior redshift probability distribution associated with the grism photometry (see Fig.3.3).

4.2.2 Comparison of EAZY parent and sub-sample

Fig.4.10 shows the redshift evolution of the SFR and stellar mass. The UV SFR was estimated from the median absolute magnitudes. The A_v dust extinction listed in the EAZY output catalog was used in place of A_{UV} in Eq.1.4. A better estimate for A_{UV} could be obtained by estimating the UV β slope of the SEDs in future work.

Sub-sample stellar mass seems to be comparable to parent sample at $z \sim 4$, but is higher at higher redshifts. A similar trend is seen in the SFR plot but only for $z \sim 6$. These results are similar to the slight increase in SFR and stellar mass found by Barlow-Hall et al. 2019 for LAEs between $z \sim 2$ to 6, but not as drastic as those from Nilsson et al. 2009 who find rapid evolution between LAEs at $z > 3$ vs those at $z \sim 2$.

Among the parent sample sources, we see that there is no evolution of stellar mass with increasing redshift, but a slight rise in SFR with redshift.

SFR vs Stellar Mass

Fig.4.11 shows the UV SFR vs stellar mass plot for the EAZY parent sample and sub-sample at $z \sim 4, 5$, and 6.

We see that the sub-sample has generally higher SFR and stellar mass than parent sample. This could be because presence of $Ly\alpha$ is a signature of star formation, which in turn could reflect the fact that we only *observe* $Ly\alpha$ from the sub-sample and

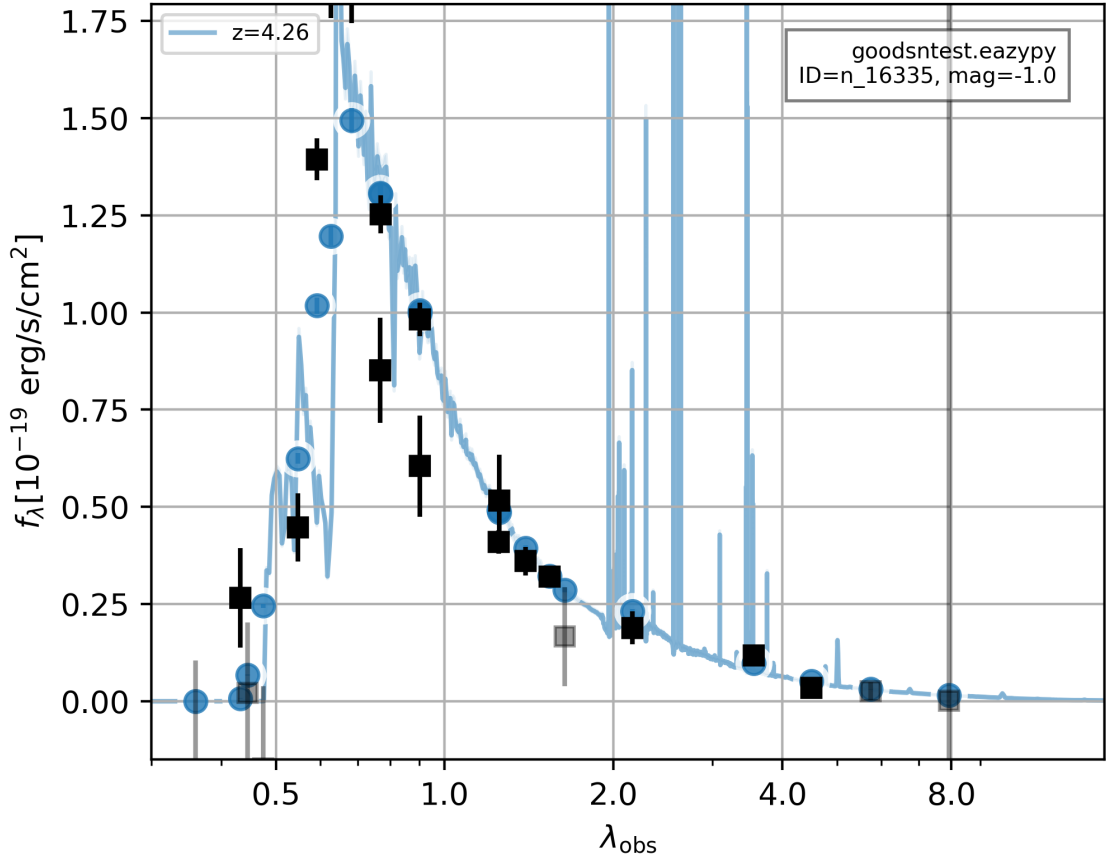
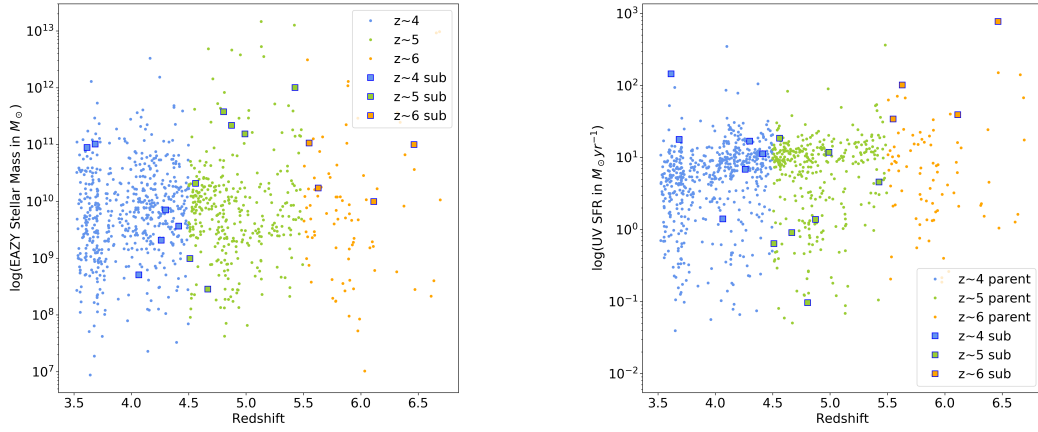


Figure 4.9: An example SED fit for n_16335 from EAZY on the left panel with observed flux (in erg/s/cm^2) as a function of observed wavelength (in μm). The black squares are the photometric fluxes with error bars from the catalog, grey squares are for data with $\text{SNR} < 2$, and grey ‘x’s are for “missing” data with flux less than the observation threshold. The blue line is the best-fit SED template combination, blue circles show the flux density of the fitted SED at the corresponding wavelengths integrated through the filter bandpasses, and blue shaded region depicts the possible spread of the fit due to large error bars or dust extinction.

therefore, derive higher SFRs for only these sources. Therefore, we cannot claim from this plot alone that LAEs necessarily have intrinsically higher SFRs and stellar masses than LBGs.

Luminosity Function

Fig.4.12 shows the LF for the sources in the EAZY parent sample at $z \sim 4, 5$, and 6 derived using the median absolute magnitudes listed in the EAZY output catalog. We see that at around $M_{UV} \sim -21$, the incompleteness of our sample begins to affect the number counts and the luminosity function falls off very rapidly. Retrieving proper number counts would require application of completeness corrections that are beyond the



(a) Evolution of the EAZY derived stellar mass as a function of redshift $z \sim 4$ (blue), 5 (green), and 6 (orange).

(b) Evolution of the UV SFR as a function of redshift $z \sim 4$ (blue), 5 (green), and 6 (orange).

Figure 4.10: The evolution of stellar mass and UV SFR with redshift. Parent sample is depicted with colored dots, and sub-sample with squares.

scope of this project.

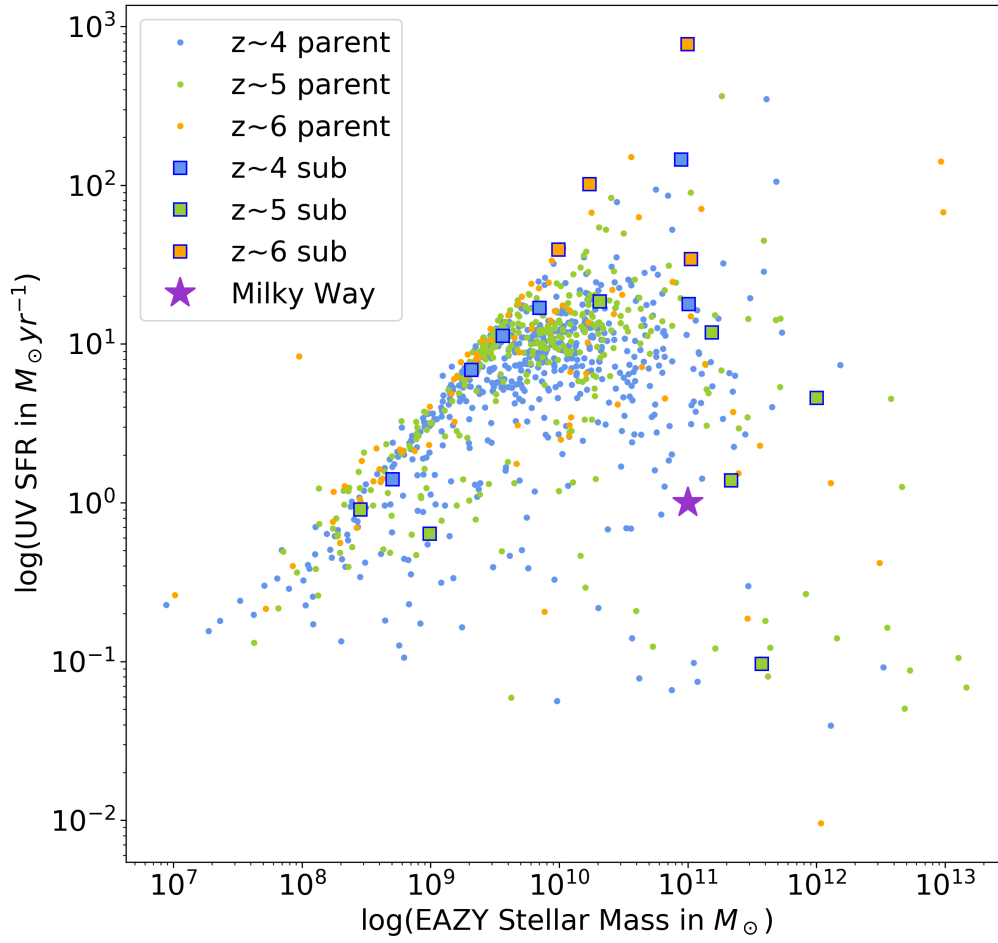


Figure 4.11: SFR vs stellar mass plot for EAZY parent sample at $z \sim 4$ (blue), 5 (green), and 6 (orange). The parent sample is depicted with colored dots, while the sub-sample with squares. The position of the Milky Way on the plot is shown with a purple star.

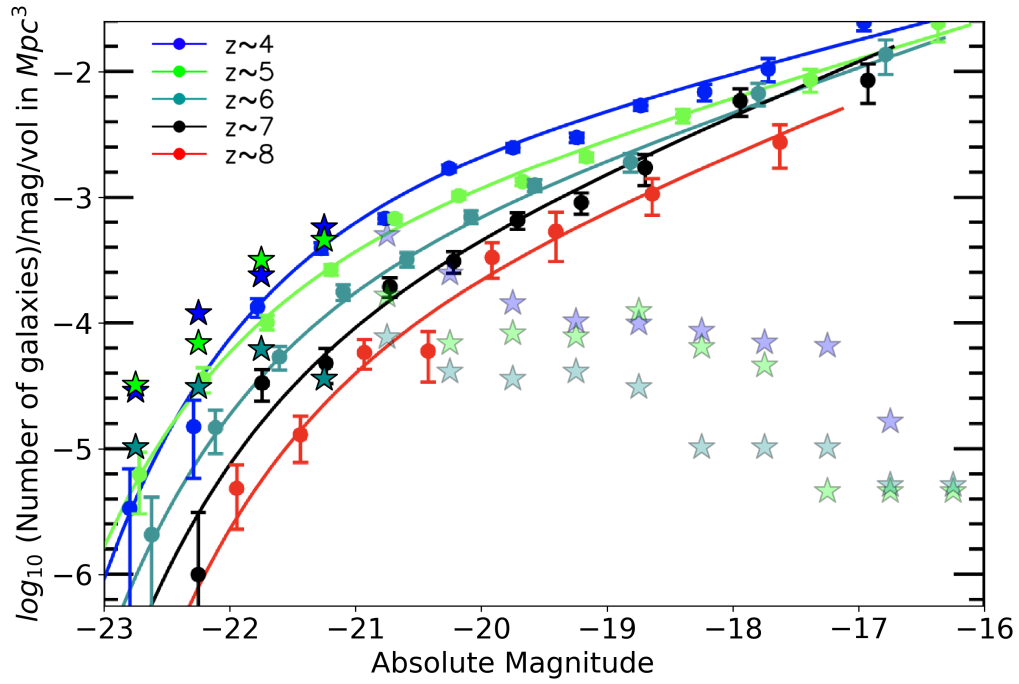


Figure 4.12: The LF derived from this work over-plotted onto the LF from Bouwens, Illingworth, Oesch, et al. 2015 (same as Fig.1.3). The data from this work is shown with star markers at $z \sim 4$ (blue), 5 (green), and 6 (teal). The transparency represents the part of our data where sample incompleteness grossly affects derived number counts.

4.3 Summary

Table 4.2 presents a summary of selected properties derived for the sub-sample from GALFIT and EAZY. Sizes under 0.1 kpc are marked with a ‘u’ for unresolved. We also include a quality flag for the SED fits based on visual inspection. Fits with less spread and small uncertainties on the flux data points are flagged “good” (e.g.: Fig.A.9 in Appendix.A). Those with a large spread and large uncertainties are flagged “poor” (e.g.: Fig.A.21 in Appendix.A). The “average” ones are somewhere in between (e.g.: Fig.A.27 in Appendix.A). In addition, we add some relevant comments about the sources in the last column.

We see that `n_16335` is a good candidate for follow-up study because it is resolved in GALFIT, but not too extended, which could mean that it is a truly compact object, potentially a super star cluster. From the SED fit discussed in Sec.4.2.1, it seems to have a stellar mass and SFR that is consistent with this possibility.

Source	GALFIT Radius		EAZY SED			Notes
	Continuum (kpc)	$Ly\alpha$ (kpc)	Fit quality	stellar mass (M_\odot)	SFR ($M_\odot yr^{-1}$)	
s_12390	0.11 (u)	0.68	good	1.06e+11	34.19	AGN/Quasar (McLure et al. 2018, Eric Wim Flesch 2021), Studied in Cassata et al. 2020
s_17197	3.36	0.33	good	2.07e+10	18.57	GALFIT fit with 5 Sérsics
s_17357	0.04 (u)	0.04 (u)	good	8.85e+10	145.35	AGN/Quasar (Eric Wim Flesch 2021)
s_18207	0.16	0.50	poor	2.17e+11	1.38	
s_21181	0.58	0.37	average	1.02e+11	17.81	AGN/Quasar (Eric Wim Flesch 2021)
s_26144	0.41	0.10 (u)	good	3.65e+09	11.26	Studied in Cassata et al. 2020
s_33531	0.04 (u)	0.32	poor	9.83e+08	0.64	
s_36953	0.09 (u)	0.09 (u)	poor	3.76e+11	<i>0.10</i>	
s_43831	0.45	0.22	average	5.08e+08	1.40	
s_44106	0.08 (u)	2.24	poor	<i>2.84e+08</i>	0.91	
n_16335	0.32	1.39	good	2.07e+09	6.86	Potential super star cluster
n_16708	1.01	0.86	average	1.54e+11	11.78	
n_29365	0.18	0.13	average	9.95e+10	773.40	Could be M star based on SED
n_31351	0.16	0.31	average	9.90e+09	39.34	Could be M star based on SED
n_39376	0.03 (u)	0.03 (u)	poor	1.01e+12	4.58	
e_06005	0.23	0.53	average	1.72e+10	101.50	
e_18484	0.78	3.45	good	7.05e+09	16.87	

Table 4.2: A summary of the properties derived for the sub-sample. The first column is the name of the source, second and third columns give the GALFIT radii for continuum and $Ly\alpha$ images respectively and tag unresolved (< 0.1 kpc) fits with a ‘u,’ fourth column is a flag for the quality of the EAZY SED fit based on the observed spread of the SED, fifth and sixth are the stellar mass and SFR from EAZY, and the last column includes some notable features of the source. The highest derived stellar mass and SFR values are shown in bold font, and the lowest in italicized font.

Chapter 5

Discussion and Further Work

In this chapter, we find our sub-sample sources in other studies from literature, discuss the uncertainty associated with our measurements, and briefly explore a few other avenues of analysis that were beyond the scope of this project, but important all the same.

5.1 Comparison of Sub-sample with Literature

In this section, we note a few interesting catalogs from literature that some of our sub-sample sources appear in (matched by RA and Dec co-ordinates).

5.1.1 Van Der Wel Catalog

All 10 GOODS-S sub-sample sources, and most of the parent sample sources in the GOODS-S, and UDS fields are part of van der Wel et al. 2012. They measure the global structural parameters 109,533 H_{F160W} -selected sources by Sérsic model fitting in H_{F160W} , J_{F125W} and, for a subset, Y_{F105W} filters. Their results are compared with ours in Fig.5.1

The results are generally in agreement except for the Sérsic index and axis ratio. This might be because we set a constraint on the latter to remain between 0.5 and 1 (Table 3.4) as we did not want to fit very elongated disk models to our compact objects. Further, the radii in this work were also constrained to small values - no more than 10 pixels, (which translates to 5 arcseconds). In contrast, some of the radii derived in van der Wel et al. 2012 were as high as 15 or even 24 arcseconds (not shown on the plot in Fig.5.1).

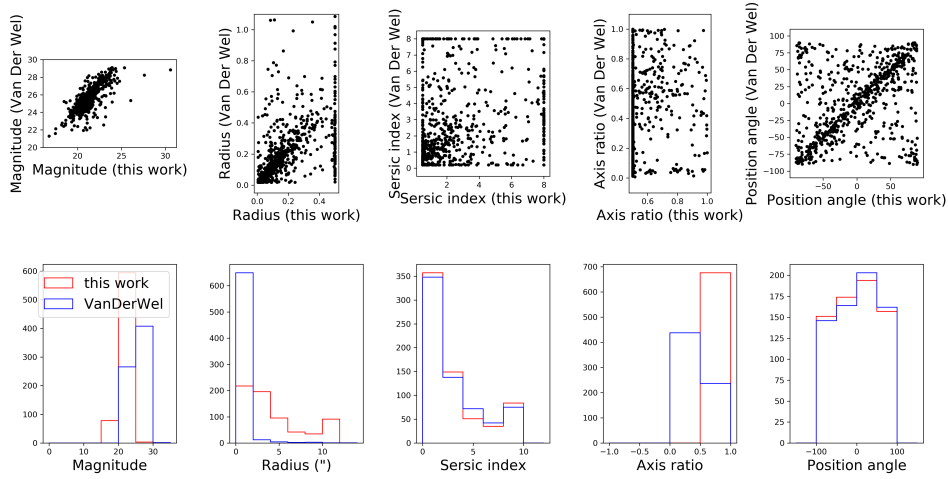


Figure 5.1: Comparison of our derived galfit parameters with those from van der Wel et al. 2012

5.1.2 ALPINE Survey

Two of the sub-sample sources, `s_12390` and `s_26144` were studied by Cassata et al. 2020, who estimated the stellar mass and SFR using the LePhare code (Arnouts and O. Ilbert 2011). Their results agree well with the EAZY results as shown in Table 5.1.

Name	Catalog	$\log(\text{Stellar Mass})$	$\log(\text{SFR})$
<code>s12390</code>	This work	11.03	1.54
CANDELS_GOODS 14	ALPINE-ALMA	10.49	1.5
<code>s26144</code>	This work	9.56	1.19
CANDELS_GOODS 12	ALPINE-ALMA	9.3	1.12

Table 5.1: Parameters and their constraints given to GALFIT via the constraint file

5.1.3 Quasars and AGN

`s_17357` and `s_21181` were identified as quasars in Eric W. Flesch 2019. `s_12390` was tagged as an AGN source in the VANDELS survey catalog (McLure et al. 2018). For these three sources, at least, the reason for compactness is clear - they are AGN/Quasar point sources.

5.2 Error Analysis

The main errors in our analysis stem from the exercise of fitting templates, both for morphology and for the spectra.

In general, our simplistic models, such as the Sérsic used to fit galaxy morphology and SED templates used to fit spectra, do not fully capture the true characteristics of galaxies. Complicating matters further is the fact that our initial guesses for the fitting are just that.

Additionally, there are errors from telescope imaging and spectroscopy which are included in the sigma images given to GALFIT, and the catalog flux errors given to EAZY.

5.2.1 GALFIT errors

Fig.5.2 shows the derived GALFIT uncertainties for radius, Sérsic index, and x position as a function of the SNR of the continuum image (as calculated in Sec.3.1.5). It can be seen that GALFIT returns un-physical uncertainty estimates upto 10^{10} especially when fitting images that have low SNR.

Besides these uncertainties, there are several other factors that must be taken into account when considering the results from this work.

dos Reis et al. 2020 found that since GALFIT is a least-squares fitting algorithm, the use of bad priors can affect the output parameter values settling the solution into a local χ^2 minimum. Although in theory, the initial parameters should not have a major effect on the fit unless they are considerably different from the actual values, in practice, the initial parameters (especially the magnitudes) are much more important in order to retrieve the models that provide the best residuals. Kimbrell et al. 2021 found that GALFIT magnitudes are most sensitive to changes in the sky background, while effective radii and Sérsic indices are most sensitive to the PSF.

Moreover, they found that a single Sérsic component was a poor fit and left very bright residuals. Meert, Vikram, and Mariangela Bernardi 2013 show that bias of 0.05 mag and 5 per cent of the half-light radius result from fitting a two-component galaxy with a single component and that this bias increases to 0.1 mag and 10 per cent of the half-light radius for brighter galaxies. M. Bernardi et al. 2014 show that single Sérsic fit tends to overestimate the sizes by about 10-15 per cent, particularly for the largest objects and that this bias is worst for objects that are likely to be ellipticals.

We also discussed in Sec.2.2.1 how high-z galaxies do not fit into the Hubble classification. For this reason, many studies favor non-parametric measurements such as the CAS (concentration, asymmetry, clumpiness) system and the Gini index (Lotz, Primack, and Madau 2004, Cotini et al. 2013, Bignone et al. 2020). Even more recently, convolutional neural networks (CNNs) have been used to analyze visual morphology and model-based structural parameters (e.g.: Tohill et al. 2021).

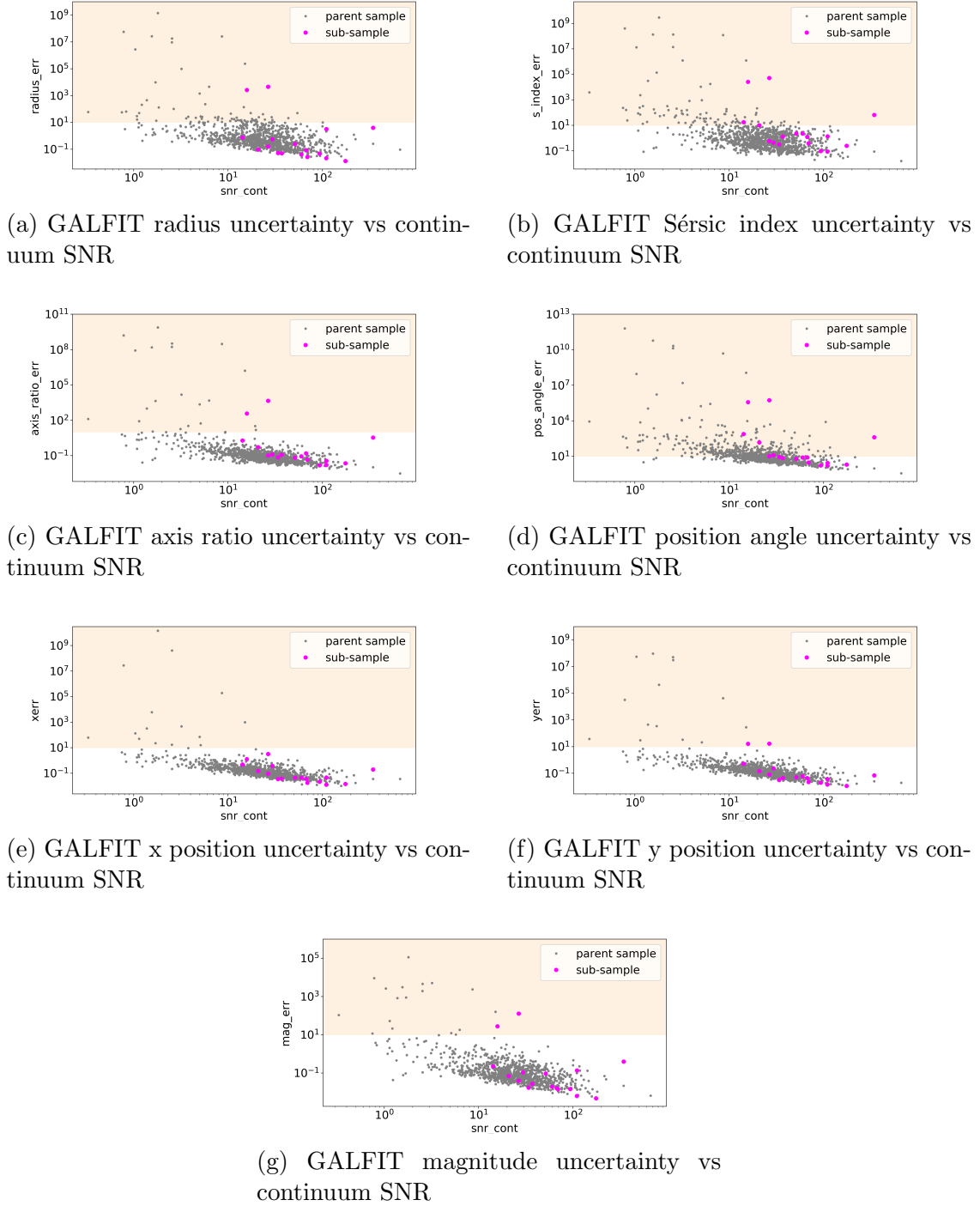


Figure 5.2: Derived GALFIT uncertainty as a function of the SNR of the continuum image (Sec.3.1.5). The shaded region indicates unphysical uncertainty estimates owing to low SNR in the input image supplied to GALFIT.

Still, for the compact sources studied in this project, parametric estimations, especially the Sérsic, seem to work well (Sec.3.2.2) because for our purposes, we only intend to retrieve a characteristic size measurement, and not the exact radius.

5.2.2 EAZY Errors

SED fitting codes like EAZY are quite reliable and robust in terms of redshift fitting. However, there is some debate as to their accuracy when it comes to estimating physical properties of the galaxies (Magris C. et al. 2015). Since we’re using EAZY primarily for the latter purpose, our results may suffer from these inaccuracies as well. Estimation of SFRs is especially tricky because they require an assumption about the IMF and star formation history of the galaxy (Sec.1.2).

However, as was discussed in Sec.5.1.2, the properties derived by Cassata et al. 2020 (using the LaPhare code) match with our EAZY results to within 0.1 dex. This was also demonstrated in studies such as Dahlen et al. 2013 and Mobasher et al. 2015 where results from several popular SED fitting codes turned out to be very similar to each other. That said, it is worth pointing out that many of these codes utilize some form of χ^2 minimization, which might mean they are essentially the same algorithm. In that case it is unsurprising that their results match.

5.3 Noise

Since the $Ly\alpha$ signal has lower SNR than the continuum, the noise would be relatively higher. Hence, we can add noise to the continuum image to simulate the noise level for $Ly\alpha$ observations. Fig.5.3b demonstrates this by adding Gaussian noise with mean = 0 and standard deviation = 10% of the maximum of the continuum flux value. We see that the resulting “noisy continuum” resembles the $Ly\alpha$ image for the object. We thus conclude that if the $Ly\alpha$ did have a diffuse extended emission like in low- z objects from literature, it would not be possible to observe it at this SNR. This was only a basic test, but more robust tests would need to be performed by artificially redshifting resolved, extended local galaxies to see how much of the extended structure we can recover (e.g. van den Bergh, R. G. Abraham, Whyte, et al. 2002, Petty et al. 2009).

5.4 LAE vs LBG

There is evidence to suggest that LAEs and LBGs are similar populations (Dayal and Ferrara 2012, de La Vieuville, Pelló, et al. 2020). Steidel et al. 2011 even go so far as to say that all LBGs would be identified as LAEs if the sensitivity of observations were high enough. This is why many studies including our own compare the two populations. However, it is also true that the physical properties such as size and stellar mass derived for LAEs are often different from those for LBGs (Malhotra, J. E. Rhoads, et al. 2012, Arrabal Haro et al. 2020). Hagen et al. 2016 argue that LAEs and LBGs cannot be compared directly due to this difference, and they instead use a sample of optical emission line galaxies (oELGs) because they have similar stellar masses, sizes, and SFRs as their LAEs. In future, we could also compare our LAE sub-sample to galaxy populations with similar properties, and see if our results and interpretation change significantly.

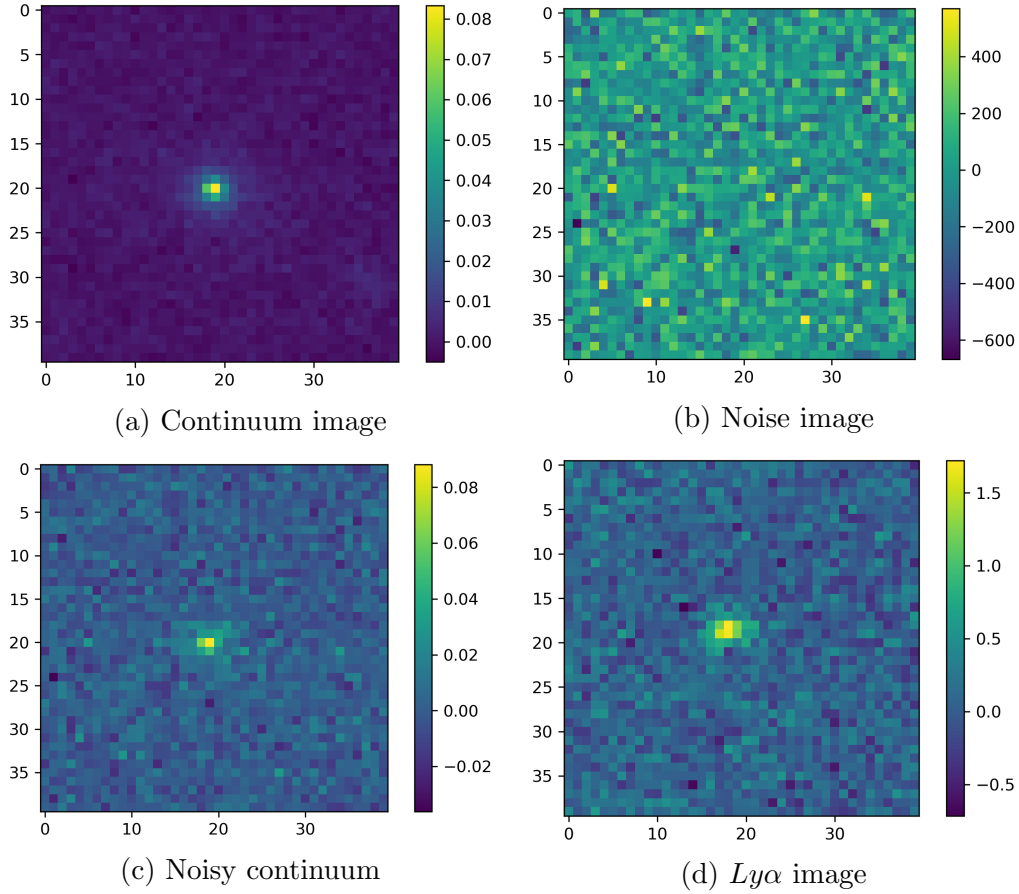


Figure 5.3: Images demonstrating the effect of noise on our observations. The first panel shows the continuum image for `s_21181` as an example. Second panel shows a Gaussian noise image with mean 0 and standard deviation 10% of the maximum of the continuum image. Third panel shows the continuum image with the noise added to it. Fourth panel shows `s_21181`'s $Ly\alpha$ image for comparison.

We can further expand upon the work done in this project by expanding our sample to include more LAE and LBG objects at lower and higher redshifts than what we used here. We can also repeat the analysis for other emission lines, e.g., $H\alpha$, OIII, CIV, and compare morphologies across the spectrum.

$H\alpha$, in particular, is a good candidate for follow-up study because it is very bright (although not as bright as $Ly\alpha$), and it is much less prone to scattering and dust attenuation than $Ly\alpha$. This means that whereas $Ly\alpha$ scatters out to form extended halos, $H\alpha$ is a much better tracer of the gas around young stars. Therefore, it can provide a more accurate picture of how compact or extended the sub-sample truly is. Furthermore, as noted in Sec.1.1.1, $H\alpha$ can be used in conjunction with the optical continuum to trace the young vs old stellar populations separately. We could then also get an estimate of the age of the LAEs and the stage of evolution they are at. Especially for super-star cluster candidates, this could help us understand how and when they formed.

All the above mentioned projects would require that we use other instruments capable of observing the specific emission lines at these redshifts. James Webb Space

Telescope (JWST), for instance provides IFU and spectroscopic coverage out to $5\ \mu m$, thereby allowing us to observe $H\alpha$ at higher redshift than HST. Other future telescopes such as the Extremely Large Telescope (ELT) can also help resolve compact objects of $< kpc$ scales at high redshift.

Chapter 6

Conclusion

We present a sample of 17 LAEs at $z \sim 4 - 7$ observed in 3D HST grism data. Their key feature is their extremely compact (~ 1 kpc size) morphology in both UV continuum and $Ly\alpha$ line images. The 17 objects were selected from a parent sample of 1060 LBGs that were in turn selected from publicly available catalogs from literature in 4 of the 5 CANDELS fields.

We explore various reasons for compactness, and attempt to understand whether it is an anomaly, i.e., a purely observational effect, or a feature, i.e., one with actual physical basis in reality.

We fit Sérsic profiles to the $Ly\alpha$ line and UV continuum morphology images using the GALFIT program, and find that the sizes derived for the sub-sample are generally smaller than those obtained for the parent sample. This is in line with observations from literature where LAEs are found to be more compact than other star-forming galaxies.

We also obtain photometric fluxes from the Skelton catalog (Skelton et al. 2014) for the (991 out of 1060; see Table 3.2) objects and fit SEDs using EAZY. Here, we find that the sub-sample star-formation rates and stellar masses are generally higher than the parent sample, which again is in line with what we find in literature.

Based on our analysis, n_16335 could potentially be a truly compact source, and a good candidate for follow-up as a super star cluster. In most other cases, however, it is hard to say whether the compactness arises from physical reality or mere observational effects. Based on other findings from literature, however, we may tentatively conclude that the compact nature is the result of a combination of feature and anomaly. We will need deeper data and further analysis to say for certain.

Acknowledgements

I am extremely grateful to my advisor, Gabriel Brammer, for his kindness, patience, and invaluable guidance over the last 2 years.

I am also thankful to my supervisor Darach Watson for his astute insights and for always motivating me to do better.

I also extend my sincere gratitude to Guarn, Sune, Peter, Seiji, the PhD students Clara, John, Kate, Vadim, Malte, Vasily, and Joonas, and everyone else in the DAWN team, who have helped me more times than I can count.

I am also eternally grateful to my ex-supervisors Caitlin Casey and Volker Bromm for helping me begin my astronomy career.

I especially thank my mom, dad, and sister for their constant support and encouragement, and for believing in me when I couldn't.

Finally, I thank my mental health counsellor, Ruth at Dansk Krisekorps, without whom this work would not have been possible.

Bibliography

- [1] R.G. Abraham et al. “Galaxy morphology to $I = 25$ mag in the Hubble Deep Field”. In: *mnras* 279.3 (Apr. 1996), pp. L47–L52. DOI: 10.1093/mnras/279.3.L47. arXiv: astro-ph/9602044 [astro-ph].
- [2] L.E. Abramson et al. “The Grism Lens-Amplified Survey from Space (GLASS) - XIII. G800L optical spectra from the parallel fields”. In: *mnras* 493.1 (Mar. 2020), pp. 952–972. DOI: 10.1093/mnras/staa276. arXiv: 1906.00008 [astro-ph.GA].
- [3] Jay Anderson and Ivan R. King. “Toward High-Precision Astrometry with WFPC2. I. Deriving an Accurate Point-Spread Function”. In: *pasp* 112.776 (Oct. 2000), pp. 1360–1382. DOI: 10.1086/316632. arXiv: astro-ph/0006325 [astro-ph].
- [4] S. Arnouts and O. Ilbert. *LePHARE: Photometric Analysis for Redshift Estimate*. Aug. 2011. ascl: 1108.009.
- [5] P. Arrabal Haro et al. “Differences and similarities of stellar populations in LAEs and LBGs at $z \sim 3.4$ – 6.8 ”. In: *mnras* 495.2 (June 2020), pp. 1807–1824. DOI: 10.1093/mnras/staa1196. arXiv: 2004.11175 [astro-ph.GA].
- [6] Fabrizio Arrigoni Battaia et al. “The Stacked Ly α Emission Profile from the Circum-Galactic Medium of $z \sim 2$ Quasars”. In: *apj* 829.1, 3 (Sept. 2016), p. 3. DOI: 10.3847/0004-637X/829/1/3. arXiv: 1604.02942 [astro-ph.CO].
- [7] H. Atek et al. “On the detectability of Ly α emission in star forming galaxies. The role of dust”. In: *aap* 488.2 (Sept. 2008), pp. 491–509. DOI: 10.1051/0004-6361:200809527. arXiv: 0805.3501 [astro-ph].
- [8] R. Bacher et al. “Tracking the Lyman alpha emission line in the CircumGalactic Medium in MUSE data”. In: EAS Publications Series 78-79 (Sept. 2016), pp. 233–245. DOI: 10.1051/eas/1678011.
- [9] R. Bacon et al. “The MUSE Extremely Deep Field: The cosmic web in emission at high redshift”. In: *aap* 647, A107 (Mar. 2021), A107. DOI: 10.1051/0004-6361/202039887. arXiv: 2102.05516 [astro-ph.CO].
- [10] Kyle Barbary et al. *kbarbary/sep: v1.0.0*. Version v1.0.0. Sept. 2016. DOI: 10.5281/zenodo.159035. URL: <https://doi.org/10.5281/zenodo.159035>.
- [11] M. Barden, K. Jahnke, and B. Häußler. “FERENGI: Redshifting Galaxies from SDSS to GEMS, STAGES, and COSMOS”. In: *apjs* 175.1 (Mar. 2008), pp. 105–115. DOI: 10.1086/524039. arXiv: 0812.1022 [astro-ph].
- [12] Cassandra Barlow-Hall et al. “High Redshift LAEs and their Cosmic Evolution: Morphologies, SFR and AGN Activity from $z \sim 2$ to 6”. In: *NLUAstro* 1.39-58 (2019). URL: <https://eprints.lancs.ac.uk/id/eprint/134671/>.

- [13] Nate Bastian and Carmela Lardo. “Globular cluster mass-loss in the context of multiple populations”. In: *mnras* 453.1 (Oct. 2015), pp. 357–364. DOI: 10.1093/mnras/stv1661. arXiv: 1507.05634 [astro-ph.GA].
- [14] C.M. Baugh, S. Cole, and C.S. Frenk. “Evolution of the Hubble sequence in hierarchical models for galaxy formation”. In: *mnras* 283.4 (Dec. 1996), pp. 1361–1378. DOI: 10.1093/mnras/283.4.1361. arXiv: astro-ph/9602085 [astro-ph].
- [15] M. Bernardi et al. “Systematic effects on the size-luminosity relations of early- and late-type galaxies: dependence on model fitting and morphology”. In: *mnras* 443.1 (Sept. 2014), pp. 874–897. DOI: 10.1093/mnras/stu1106.
- [16] Lucas A. Bignone et al. “Non-parametric morphologies of galaxies in the EAGLE simulation”. In: *mnras* 491.3 (Jan. 2020), pp. 3624–3642. DOI: 10.1093/mnras/stz3014. arXiv: 1908.10936 [astro-ph.GA].
- [17] Elena Borisova et al. “Ubiquitous Giant $Ly\alpha$ Nebulae around the Brightest Quasars at $z \sim 3.5$ Revealed with MUSE”. In: *apj* 831.1, 39 (Nov. 2016), p. 39. DOI: 10.3847/0004-637X/831/1/39. arXiv: 1605.01422 [astro-ph.GA].
- [18] R.J. Bouwens, G.D. Illingworth, P.A. Oesch, et al. “UV Luminosity Functions at Redshifts $z \sim 4$ to $z \sim 10$: 10,000 Galaxies from HST Legacy Fields”. In: *apj* 803.1, 34 (Apr. 2015), p. 34. DOI: 10.1088/0004-637X/803/1/34. arXiv: 1403.4295 [astro-ph.CO].
- [19] R.J. Bouwens, G.D. Illingworth, P.G. van Dokkum, et al. “Low-luminosity galaxies in the early universe have observed sizes similar to star cluster complexes”. In: *arXiv e-prints*, arXiv:2106.08336 (June 2021), arXiv:2106.08336. arXiv: 2106.08336 [astro-ph.GA].
- [20] Gabe Brammer. *Grizli: Grism redshift and line analysis software*. May 2019. ascl: 1905.001.
- [21] Gabriel B. Brammer, Pieter G. van Dokkum, and Paolo Coppi. “EAZY: A Fast, Public Photometric Redshift Code”. In: *apj* 686.2 (Oct. 2008), pp. 1503–1513. DOI: 10.1086/591786. arXiv: 0807.1533 [astro-ph].
- [22] J. Brinchmann et al. “The physical properties of star-forming galaxies in the low-redshift Universe”. In: *mnras* 351.4 (July 2004), pp. 1151–1179. DOI: 10.1111/j.1365-2966.2004.07881.x. arXiv: astro-ph/0311060 [astro-ph].
- [23] Sebastiano Cantalupo et al. “A cosmic web filament revealed in Lyman- α emission around a luminous high-redshift quasar”. In: *nat* 506.7486 (Feb. 2014), pp. 63–66. DOI: 10.1038/nature12898. arXiv: 1401.4469 [astro-ph.CO].
- [24] P. Cassata et al. “The ALPINE-ALMA [CII] survey. Small $Ly\alpha$ -[CII] velocity offsets in main-sequence galaxies at $4.4 < z < 6$ ”. In: *aap* 643, A6 (Nov. 2020), A6. DOI: 10.1051/0004-6361/202037517. arXiv: 2002.00967 [astro-ph.GA].
- [25] Renyue Cen. “Physics of Prodigious Lyman Continuum Leakers”. In: *apjl* 889.1, L22 (Jan. 2020), p. L22. DOI: 10.3847/2041-8213/ab6560. arXiv: 2001.11083 [astro-ph.GA].
- [26] Gilles Chabrier. “Galactic Stellar and Substellar Initial Mass Function”. In: *pasp* 115.809 (July 2003), pp. 763–795. DOI: 10.1086/376392. arXiv: astro-ph/0304382 [astro-ph].

- [27] Charlie Conroy. “Modeling the Panchromatic Spectral Energy Distributions of Galaxies”. In: *araa* 51.1 (Aug. 2013), pp. 393–455. DOI: 10.1146/annurev-astro-082812-141017. arXiv: 1301.7095 [astro-ph.CO].
- [28] Charlie Conroy. “On the Birth Masses of the Ancient Globular Clusters”. In: *apj* 758.1, 21 (Oct. 2012), p. 21. DOI: 10.1088/0004-637X/758/1/21. arXiv: 1101.2208 [astro-ph.GA].
- [29] Christopher J. Conselice. “The Evolution of Galaxy Structure Over Cosmic Time”. In: *araa* 52 (Aug. 2014), pp. 291–337. DOI: 10.1146/annurev-astro-081913-040037. arXiv: 1403.2783 [astro-ph.GA].
- [30] Matthew A. Cornachione et al. “The BOSS Emission-line Lens Survey. V. Morphology and Substructure of Lensed Ly α Emitters at Redshift $z \sim 2.5$ in the BELLS GALLERY”. In: *apj* 853.2, 148 (Feb. 2018), p. 148. DOI: 10.3847/1538-4357/aaa412. arXiv: 1708.08854 [astro-ph.GA].
- [31] Stefano Cotini et al. “The merger fraction of active and inactive galaxies in the local Universe through an improved non-parametric classification”. In: *mnras* 431.3 (May 2013), pp. 2661–2672. DOI: 10.1093/mnras/stt358. arXiv: 1303.0036 [astro-ph.GA].
- [32] Jean-Baptiste Courbot et al. “DETECTION OF FAINT EXTENDED SOURCES IN HYPERSPSPECTRAL DATA AND APPLICATION TO HDF-S MUSE OBSERVATIONS”. In: (Mar. 2016). URL: <https://hal.archives-ouvertes.fr/hal-01266333>.
- [33] Lennox L. Cowie, Esther M. Hu, and Antoinette Songaila. “Faintest Galaxy Morphologies From HST WFPC2 Imaging of the Hawaii Survey Fields”. In: *aj* 110 (Oct. 1995), p. 1576. DOI: 10.1086/117631. arXiv: astro-ph/9507055 [astro-ph].
- [34] E. Daddi et al. “Multiwavelength Study of Massive Galaxies at $z \sim 2$. I. Star Formation and Galaxy Growth”. In: *apj* 670.1 (Nov. 2007), pp. 156–172. DOI: 10.1086/521818. arXiv: 0705.2831 [astro-ph].
- [35] Tomas Dahlen et al. “A Critical Assessment of Photometric Redshift Methods: A CANDELS Investigation”. In: *apj* 775.2, 93 (Oct. 2013), p. 93. DOI: 10.1088/0004-637X/775/2/93. arXiv: 1308.5353 [astro-ph.CO].
- [36] Pratika Dayal and Andrea Ferrara. “Ly α emitters and Lyman-break galaxies: dichotomous twins”. In: *mnras* 421.3 (Apr. 2012), pp. 2568–2579. DOI: 10.1111/j.1365-2966.2012.20486.x. arXiv: 1109.0297 [astro-ph.CO].
- [37] G. de La Vieuville, D. Bina, et al. “Faint end of the $z \sim 3$ –7 luminosity function of Lyman-alpha emitters behind lensing clusters observed with MUSE”. In: *aap* 628, A3 (Aug. 2019), A3. DOI: 10.1051/0004-6361/201834471. arXiv: 1905.13696 [astro-ph.GA].
- [38] G. de La Vieuville, R. Pelló, et al. “MUSE observations towards the lensing cluster A2744: Intersection between the LBG and LAE populations at $z \sim 3$ –7”. In: *aap* 644, A39 (Dec. 2020), A39. DOI: 10.1051/0004-6361/202037651. arXiv: 2009.12824 [astro-ph.GA].
- [39] Gerard de Vaucouleurs. “Recherches sur les Nebuleuses Extragalactiques”. In: *Annales d’Astrophysique* 11 (Jan. 1948), p. 247.

- [40] Jean-Michel Deharveng et al. “ $Ly\alpha$ -Emitting Galaxies at $0.2 < z < 0.35$ from GALEX Spectroscopy”. In: *apj* 680.2 (June 2008), pp. 1072–1082. DOI: 10.1086/587953. arXiv: 0803.1924 [astro-ph].
- [41] Mark Dijkstra, Adam Lidz, and J. Stuart B. Wyithe. “The impact of The IGM on high-redshift $Ly\alpha$ emission lines”. In: *mnras* 377.3 (May 2007), pp. 1175–1186. DOI: 10.1111/j.1365-2966.2007.11666.x. arXiv: astro-ph/0701667 [astro-ph].
- [42] Sandra N. dos Reis et al. “Structural analysis of massive galaxies using HST deep imaging at $z < 0.5$ ”. In: *aap* 634, A11 (Feb. 2020), A11. DOI: 10.1051/0004-6361/201936276. arXiv: 1911.12455 [astro-ph.GA].
- [43] S.P. Driver et al. “Morphological Number Counts and Redshift Distributions to $I < 26$ from the Hubble Deep Field: Implications for the Evolution of Ellipticals, Spirals, and Irregulars”. In: *apjl* 496.2 (Apr. 1998), pp. L93–L96. DOI: 10.1086/311257. arXiv: astro-ph/9802092 [astro-ph].
- [44] H. Fathivavsari et al. “A coronagraphic absorbing cloud reveals the narrow-line region and extended Lyman α emission of QSO J0823 + 0529”. In: *mnras* 454.1 (Nov. 2015), pp. 876–888. DOI: 10.1093/mnras/stv1984. arXiv: 1508.06513 [astro-ph.GA].
- [45] Steven L. Finkelstein et al. “The Evolution of the Galaxy Rest-frame Ultraviolet Luminosity Function over the First Two Billion Years”. In: *apj* 810.1, 71 (Sept. 2015), p. 71. DOI: 10.1088/0004-637X/810/1/71. arXiv: 1410.5439 [astro-ph.GA].
- [46] Eric W. Flesch. “The Million Quasars (Milliquas) Catalogue, v6.4”. In: *arXiv e-prints*, arXiv:1912.05614 (Dec. 2019), arXiv:1912.05614. arXiv: 1912.05614 [astro-ph.GA].
- [47] Eric Wim Flesch. “Identification confusion and blending concealment in the SDSS-DR16 Quasar catalogues - 40 new quasars and 82 false quasars identified”. In: *mnras* 504.1 (June 2021), pp. 621–635. DOI: 10.1093/mnras/stab812. arXiv: 2012.00164 [astro-ph.GA].
- [48] Natascha M. Förster Schreiber and Stijn Wuyts. “Star-Forming Galaxies at Cosmic Noon”. In: *araa* 58 (Aug. 2020), pp. 661–725. DOI: 10.1146/annurev-astro-032620-021910. arXiv: 2010.10171 [astro-ph.GA].
- [49] Eric Gawiser. “Spectral Energy Distribution fitting: Application to $Ly\alpha$ -emitting galaxies”. In: *nar* 53.3 (June 2009), pp. 50–53. DOI: 10.1016/j.newar.2009.04.006. arXiv: 0904.3798 [astro-ph.CO].
- [50] Eric Gawiser et al. “ $Ly\alpha$ -Emitting Galaxies at $z = 3.1$: L^* Progenitors Experiencing Rapid Star Formation”. In: *apj* 671.1 (Dec. 2007), pp. 278–284. DOI: 10.1086/522955. arXiv: 0710.2697 [astro-ph].
- [51] R.E. Griffiths et al. “The Morphology of Faint Galaxies in Medium Deep Survey Images Using WFPC2”. In: *apjl* 435 (Nov. 1994), p. L19. DOI: 10.1086/187584.
- [52] Caryl Gronwall et al. “The Rest-frame Ultraviolet Light Profile Shapes of $Ly\alpha$ -emitting Galaxies at $z = 3.1$ ”. In: *apj* 743.1, 9 (Dec. 2011), p. 9. DOI: 10.1088/0004-637X/743/1/9. arXiv: 1005.3006 [astro-ph.CO].

- [53] Lucia Guaita et al. “Ly α -emitting Galaxies at $z = 2.1$: Stellar Masses, Dust, and Star Formation Histories from Spectral Energy Distribution Fitting”. In: *apj* 733.2, 114 (June 2011), p. 114. DOI: 10.1088/0004-637X/733/2/114. arXiv: 1101.3017 [astro-ph.CO].
- [54] Yicheng Guo et al. “Multi-wavelength View of Kiloparsec-scale Clumps in Star-forming Galaxies at $z \sim 2$ ”. In: *apj* 757.2, 120 (Oct. 2012), p. 120. DOI: 10.1088/0004-637X/757/2/120. arXiv: 1110.3800 [astro-ph.CO].
- [55] Alex Hagen et al. “HST Emission Line Galaxies at $z \sim 2$: Comparing Physical Properties of Lyman Alpha and Optical Emission Line Selected Galaxies”. In: *apj* 817.1, 79 (Jan. 2016), p. 79. DOI: 10.3847/0004-637X/817/1/79. arXiv: 1512.03063 [astro-ph.GA].
- [56] Boris Häußler et al. “MegaMorph - multiwavelength measurement of galaxy structure: complete Sérsic profile information from modern surveys”. In: *mnras* 430.1 (Mar. 2013), pp. 330–369. DOI: 10.1093/mnras/sts633. arXiv: 1212.3332 [astro-ph.CO].
- [57] Boris Häussler et al. “GEMS: Galaxy Fitting Catalogs and Testing Parametric Galaxy Fitting Codes: GALFIT and GIM2D”. In: *apjs* 172.2 (Oct. 2007), pp. 615–633. DOI: 10.1086/518836. arXiv: 0704.2601 [astro-ph].
- [58] Matthew Hayes. “Lyman Alpha Emitting Galaxies in the Nearby Universe”. In: *pasa* 32, e027 (July 2015), e027. DOI: 10.1017/pasa.2015.25. arXiv: 1505.07483 [astro-ph.GA].
- [59] Matthew Hayes, Göran Östlin, Florent Duval, et al. “The Lyman Alpha Reference Sample. II. Hubble Space Telescope Imaging Results, Integrated Properties, and Trends”. In: *apj* 782.1, 6 (Feb. 2014), p. 6. DOI: 10.1088/0004-637X/782/1/6. arXiv: 1308.6578 [astro-ph.CO].
- [60] Matthew Hayes, Göran Östlin, Daniel Schaerer, et al. “The Lyman Alpha Reference Sample: Extended Lyman Alpha Halos Produced at Low Dust Content”. In: *apjl* 765.2, L27 (Mar. 2013), p. L27. DOI: 10.1088/2041-8205/765/2/L27. arXiv: 1303.0006 [astro-ph.CO].
- [61] Matthew Hayes, Daniel Schaerer, et al. “On the Redshift Evolution of the Ly α Escape Fraction and the Dust Content of Galaxies”. In: *apj* 730.1, 8 (Mar. 2011), p. 8. DOI: 10.1088/0004-637X/730/1/8. arXiv: 1010.4796 [astro-ph.CO].
- [62] Joseph F. Hennawi and J. Xavier Prochaska. “Quasars Probing Quasars. IV. Joint Constraints on the Circumgalactic Medium from Absorption and Emission”. In: *apj* 766.1, 58 (Mar. 2013), p. 58. DOI: 10.1088/0004-637X/766/1/58. arXiv: 1303.2708 [astro-ph.CO].
- [63] Joseph F. Hennawi, J. Xavier Prochaska, et al. “Quasar quartet embedded in giant nebula reveals rare massive structure in distant universe”. In: *Science* 348.6236 (May 2015), pp. 779–783. DOI: 10.1126/science.aaa5397. arXiv: 1505.03786 [astro-ph.GA].
- [64] Edmund Christian Herenz, Tanya Urrutia, et al. “The MUSE-Wide survey: A first catalogue of 831 emission line galaxies”. In: *aap* 606, A12 (Sept. 2017), A12. DOI: 10.1051/0004-6361/201731055. arXiv: 1705.08215 [astro-ph.GA].

- [65] Edmund Christian Herenz, Lutz Wisotzki, et al. “The MUSE-Wide Survey: A determination of the Lyman α emitter luminosity function at $3 < z < 6$ ”. In: *aap* 621, A107 (Jan. 2019), A107. DOI: 10.1051/0004-6361/201834164. arXiv: 1810.05037 [astro-ph.GA].
- [66] E.P. Hubble. “Extragalactic nebulae.” In: *apj* 64 (Dec. 1926), pp. 321–369. DOI: 10.1086/143018.
- [67] M. Huertas-Company et al. “Mass assembly and morphological transformations since $z \sim 3$ from CANDELS”. In: *mnras* 462.4 (Nov. 2016), pp. 4495–4516. DOI: 10.1093/mnras/stw1866. arXiv: 1606.04952 [astro-ph.GA].
- [68] T.H. Jarrett. “Near-Infrared Galaxy Morphology Atlas”. In: *pasp* 112.774 (Aug. 2000), pp. 1008–1080. DOI: 10.1086/316603.
- [69] Linhua Jiang, Eiichi Egami, et al. “Physical Properties of Spectroscopically Confirmed Galaxies at $z \geq 6$. II. Morphology of the Rest-frame UV Continuum and $Ly\alpha$ Emission”. In: *apj* 773.2, 153 (Aug. 2013), p. 153. DOI: 10.1088/0004-637X/773/2/153. arXiv: 1303.0027 [astro-ph.CO].
- [70] Linhua Jiang, Kristian Finlator, et al. “Physical Properties of Spectroscopically Confirmed Galaxies at $z \geq 6$. III. Stellar Populations from SED Modeling with Secure $Ly\alpha$ Emission and Redshifts”. In: *apj* 816.1, 16 (Jan. 2016), p. 16. DOI: 10.3847/0004-637X/816/1/16. arXiv: 1511.01519 [astro-ph.GA].
- [71] Russell Johnston. “Shedding light on the galaxy luminosity function”. In: *aapr* 19, 41 (Aug. 2011), p. 41. DOI: 10.1007/s00159-011-0041-9. arXiv: 1106.2039 [astro-ph.CO].
- [72] S. Jouvel et al. “CLASH: Photometric redshifts with 16 HST bands in galaxy cluster fields”. In: *aap* 562, A86 (Feb. 2014), A86. DOI: 10.1051/0004-6361/201322419. arXiv: 1308.0063 [astro-ph.CO].
- [73] A. Katsianis et al. “The high-redshift SFR- M_* relation is sensitive to the employed star formation rate and stellar mass indicators: towards addressing the tension between observations and simulations”. In: *mnras* 492.4 (Mar. 2020), pp. 5592–5606. DOI: 10.1093/mnras/staa157. arXiv: 2001.06025 [astro-ph.GA].
- [74] Jr. Kennicutt Robert C. “Star Formation in Galaxies Along the Hubble Sequence”. In: *araa* 36 (Jan. 1998), pp. 189–232. DOI: 10.1146/annurev.astro.36.1.189. arXiv: astro-ph/9807187 [astro-ph].
- [75] Vikram Khaire et al. “The redshift evolution of escape fraction of hydrogen ionizing photons from galaxies”. In: *mnras* 457.4 (Apr. 2016), pp. 4051–4062. DOI: 10.1093/mnras/stw192. arXiv: 1510.04700 [astro-ph.CO].
- [76] Shotaro Kikuchihara et al. “Early Low-mass Galaxies and Star-cluster Candidates at $z \sim 6 - 9$ Identified by the Gravitational-lensing Technique and Deep Optical/Near-infrared Imaging”. In: *The Astrophysical Journal* 893.1 (Apr. 2020), p. 60. ISSN: 1538-4357. DOI: 10.3847/1538-4357/ab7dbe. URL: <http://dx.doi.org/10.3847/1538-4357/ab7dbe>.
- [77] Seth J. Kimbrell et al. “The Diverse Morphologies and Structures of Dwarf Galaxies Hosting Optically Selected Active Massive Black Holes”. In: *apj* 911.2, 134 (Apr. 2021), p. 134. DOI: 10.3847/1538-4357/abec40. arXiv: 2103.06289 [astro-ph.GA].

- [78] Anton M. Koekemoer et al. “CANDELS: The Cosmic Assembly Near-infrared Deep Extragalactic Legacy Survey - The Hubble Space Telescope Observations, Imaging Data Products, and Mosaics”. In: *apjs* 197.2, 36 (Dec. 2011), p. 36. DOI: 10.1088/0067-0049/197/2/36. arXiv: 1105.3754 [astro-ph.CO].
- [79] Akira Konno et al. “Bright and Faint Ends of $Ly\alpha$ Luminosity Functions at $z = 2$ Determined by the Subaru Survey: Implications for AGNs, Magnification Bias, and ISM H I Evolution”. In: *apj* 823.1, 20 (May 2016), p. 20. DOI: 10.3847/0004-637X/823/1/20. arXiv: 1512.01854 [astro-ph.GA].
- [80] Pavel Kroupa. “On the variation of the initial mass function”. In: *mnras* 322.2 (Apr. 2001), pp. 231–246. DOI: 10.1046/j.1365-8711.2001.04022.x. arXiv: astro-ph/0009005 [astro-ph].
- [81] Peter Kurczynski et al. “Evolution of Intrinsic Scatter in the SFR-Stellar Mass Correlation at $0.5 < z < 3$ ”. In: *apjl* 820.1, L1 (Mar. 2016), p. L1. DOI: 10.3847/2041-8205/820/1/L1. arXiv: 1602.03909 [astro-ph.GA].
- [82] Haruka Kusakabe et al. “The stellar mass, star formation rate and dark matter halo properties of LAEs at $z \sim 2$ ”. In: *pasj* 70.1, 4 (Jan. 2018), p. 4. DOI: 10.1093/pasj/psx148. arXiv: 1707.09373 [astro-ph.GA].
- [83] Kamson Lai et al. “Spitzer Constraints on the Stellar Populations of $Ly\alpha$ -Emitting Galaxies at $z = 3.1$ ”. In: *apj* 674.1 (Feb. 2008), pp. 70–74. DOI: 10.1086/524702. arXiv: 0710.3384 [astro-ph].
- [84] C. Laigle et al. “The COSMOS2015 Catalog: Exploring the $1 < z < 6$ Universe with Half a Million Galaxies”. In: *apjs* 224.2, 24 (June 2016), p. 24. DOI: 10.3847/0067-0049/224/2/24. arXiv: 1604.02350 [astro-ph.GA].
- [85] P Larsen. *What is radiative transfer? - Resonant scattering*. URL: https://www.anisotropela.dk/encyclo/radiative_transfer.html (visited on 08/01/2021).
- [86] Floriane Leclercq et al. “The MUSE Hubble Ultra Deep Field Survey. VIII. Extended Lyman- α haloes around high- z star-forming galaxies”. In: *aap* 608, A8 (Dec. 2017), A8. DOI: 10.1051/0004-6361/201731480. arXiv: 1710.10271 [astro-ph.GA].
- [87] Chuanwu Liu et al. “Dark-ages reionization and galaxy formation simulation - IV. UV luminosity functions of high-redshift galaxies”. In: *mnras* 462.1 (Oct. 2016), pp. 235–249. DOI: 10.1093/mnras/stw1015. arXiv: 1512.00563 [astro-ph.GA].
- [88] Jennifer M. Lotz, Joel Primack, and Piero Madau. “A New Nonparametric Approach to Galaxy Morphological Classification”. In: *aj* 128.1 (July 2004), pp. 163–182. DOI: 10.1086/421849. arXiv: astro-ph/0311352 [astro-ph].
- [89] Piero Madau and Mark Dickinson. “Cosmic Star-Formation History”. In: *araa* 52 (Aug. 2014), pp. 415–486. DOI: 10.1146/annurev-astro-081811-125615. arXiv: 1403.0007 [astro-ph.CO].
- [90] Gladis Magris C. et al. “On the Recovery of Galaxy Properties from SED Fitting Solutions”. In: *pasp* 127.947 (Jan. 2015), p. 16. DOI: 10.1086/679742. arXiv: 1411.7029 [astro-ph.GA].

- [91] S. Malhotra, J. Rhoads, et al. “Large Area Lyman Alpha Survey: Finding Young Galaxies at $z=4.5$ ”. In: *Astronomical Society of the Pacific Conference Series* 240 (Jan. 2001). Ed. by John E. Hibbard, Michael Rupen, and Jacqueline H. van Gorkom, p. 97. arXiv: astro-ph/0102140 [astro-ph].
- [92] S. Malhotra, James E. Rhoads, et al. “Sizing up $Ly\alpha$ and Lyman Break Galaxies”. In: *apjl* 750.2, L36 (May 2012), p. L36. DOI: 10.1088/2041-8205/750/2/L36. arXiv: 1106.2816 [astro-ph.CO].
- [93] K.G. Malmquist. “On some relations in stellar statistics”. In: *Meddelanden fran Lunds Astronomiska Observatorium Serie I* 100 (Mar. 1922), pp. 1–52.
- [94] Michael V. Maseda and MUSE GTO Consortium. “Ultra-faint Lyman Alpha Emitters with MUSE”. In: 352 (Jan. 2020). Ed. by Elisabete da Cunha et al., pp. 331–335. DOI: 10.1017/S1743921319008391.
- [95] R.J. McLure et al. “The VANDELS ESO public spectroscopic survey”. In: *mnras* 479.1 (Sept. 2018), pp. 25–42. DOI: 10.1093/mnras/sty1213. arXiv: 1803.07414 [astro-ph.GA].
- [96] Alan Meert, Vinu Vikram, and Mariangela Bernardi. “Simulations of single- and two-component galaxy decompositions for spectroscopically selected galaxies from the Sloan Digital Sky Survey”. In: *mnras* 433.2 (Aug. 2013), pp. 1344–1361. DOI: 10.1093/mnras/stt822. arXiv: 1211.6123 [astro-ph.CO].
- [97] Matteo Messa et al. “Star-forming clumps in the Lyman Alpha Reference Sample of galaxies - I. Photometric analysis and clumpiness”. In: *mnras* 487.3 (Aug. 2019), pp. 4238–4260. DOI: 10.1093/mnras/stz1337. arXiv: 1906.04751 [astro-ph.GA].
- [98] Bahram Mobasher et al. “A Critical Assessment of Stellar Mass Measurement Methods”. In: *apj* 808.1, 101 (July 2015), p. 101. DOI: 10.1088/0004-637X/808/1/101. arXiv: 1505.01501 [astro-ph.GA].
- [99] Alice Mortlock et al. “The redshift and mass dependence on the formation of the Hubble sequence at $z > 1$ from CANDELS/UDS”. In: *mnras* 433.2 (Aug. 2013), pp. 1185–1201. DOI: 10.1093/mnras/stt793. arXiv: 1305.2204 [astro-ph.CO].
- [100] Moein Mosleh et al. “The Evolution of the Mass-Size Relation to $z = 3.5$ for UV-bright Galaxies and Submillimeter Galaxies in the GOODS-North Field”. In: *apj* 727.1, 5 (Jan. 2011), p. 5. DOI: 10.1088/0004-637X/727/1/5. arXiv: 1011.3042 [astro-ph.CO].
- [101] Erica Nelson et al. “Spatially Resolved $H\alpha$ Maps and Sizes of 57 Strongly Star-forming Galaxies at $z \sim 1$ from 3D-HST: Evidence for Rapid Inside-out Assembly of Disk Galaxies”. In: *The Astrophysical Journal Letters* 747 (Feb. 2012), p. L28. DOI: 10.1088/2041-8205/747/2/L28.
- [102] K.K. Nilsson et al. “Evolution in the properties of Lyman- α emitters from redshifts $z \sim 3$ to $z \sim 2$ ”. In: *aap* 498.1 (Apr. 2009), pp. 13–23. DOI: 10.1051/0004-6361/200810881. arXiv: 0812.3152 [astro-ph].
- [103] P.L. North et al. “Spectroscopy of extended $Ly\alpha$ envelopes around $z = 4.5$ quasars”. In: *aap* 542, A91 (June 2012), A91. DOI: 10.1051/0004-6361/201015153. arXiv: 1205.3895 [astro-ph.CO].

- [104] P.A. Oesch et al. “The Evolution of the Ultraviolet Luminosity Function from $z \sim 0.75$ to $z \sim 2.5$ Using HST ERS WFC3/UVIS Observations”. In: *apjl* 725.2 (Dec. 2010), pp. L150–L155. DOI: 10.1088/2041-8205/725/2/L150. arXiv: 1005.1661 [astro-ph.CO].
- [105] Donald E. Osterbrock. “The Escape of Resonance-Line Radiation from an Optically Thick Nebula.” In: *apj* 135 (Jan. 1962), p. 195. DOI: 10.1086/147258.
- [106] Kazuaki Ota et al. “A New Constraint on Reionization from the Evolution of the $Ly\alpha$ Luminosity Function at $z \sim 6 - 7$ Probed by a Deep Census of $z = 7.0$ $Ly\alpha$ Emitter Candidates to $0.3L^*$ ”. In: *apj* 844.1, 85 (July 2017), p. 85. DOI: 10.3847/1538-4357/aa7a0a. arXiv: 1703.02501 [astro-ph.GA].
- [107] Masami Ouchi, Yoshiaki Ono, and Takatoshi Shibuya. “Observations of the Lyman α Universe”. In: *araa* 58 (Aug. 2020), pp. 617–659. DOI: 10.1146/annurev-astro-032620-021859. arXiv: 2012.07960 [astro-ph.GA].
- [108] R B Partridge and P J.E. Peebles. “ARE YOUNG GALAXIES VISIBLE.” In: *Astrophys. J.*, 147: 868-86(Mar. 1967). (Jan. 1967). DOI: 10.1086/149161. URL: <https://www.osti.gov/biblio/4435151>.
- [109] S.M. Pascarelle et al. “Sub-galactic clumps at a redshift of 2.39 and implications for galaxy formation”. In: *nat* 383.6595 (Sept. 1996), pp. 45–50. DOI: 10.1038/383045a0.
- [110] Ana Paulino-Afonso et al. “On the UV compactness and morphologies of typical Lyman α emitters from $z \sim 2$ to $z \sim 6$ ”. In: *mnras* 476.4 (June 2018), pp. 5479–5501. DOI: 10.1093/mnras/sty281. arXiv: 1709.04470 [astro-ph.GA].
- [111] W.J. Pearson et al. “Main sequence of star forming galaxies beyond the Herschel confusion limit”. In: *aap* 615, A146 (July 2018), A146. DOI: 10.1051/0004-6361/201832821. arXiv: 1804.03482 [astro-ph.GA].
- [112] Chien Y. Peng et al. “Detailed Decomposition of Galaxy Images. II. Beyond Axisymmetric Models”. In: *aj* 139.6 (June 2010), pp. 2097–2129. DOI: 10.1088/0004-6256/139/6/2097. arXiv: 0912.0731 [astro-ph.CO].
- [113] Sara M. Petty et al. “Structures of Local Galaxies Compared to High-Redshift Star-Forming Galaxies”. In: *aj* 138.2 (Aug. 2009), pp. 362–375. DOI: 10.1088/0004-6256/138/2/362. arXiv: 0904.4433 [astro-ph.CO].
- [114] N. Pirzkal et al. “GRAPES, Grism Spectroscopy of the Hubble Ultra Deep Field: Description and Data Reduction”. In: *apjs* 154.2 (Oct. 2004), pp. 501–508. DOI: 10.1086/422582. arXiv: astro-ph/0403458 [astro-ph].
- [115] Planck Collaboration et al. “Planck 2015 results. XIII. Cosmological parameters”. In: *aap* 594, A13 (Sept. 2016), A13. DOI: 10.1051/0004-6361/201525830. arXiv: 1502.01589 [astro-ph.CO].
- [116] Swara Ravindranath et al. “The Morphological Diversities among Star-forming Galaxies at High Redshifts in the Great Observatories Origins Deep Survey”. In: *apj* 652.2 (Dec. 2006), pp. 963–980. DOI: 10.1086/507016. arXiv: astro-ph/0606696 [astro-ph].
- [117] J.E. Rhoads et al. “The Large Area Lyman Alpha Survey.” In: *Astronomical Society of the Pacific Conference Series* 232 (Jan. 2001). Ed. by Roger Clowes, Andrew Adamson, and Gordon Bromage, p. 196. arXiv: astro-ph/0104294 [astro-ph].

- [118] E. Ritondale et al. “Resolving on 100 pc scales the UV-continuum in Lyman- α emitters between redshift 2 and 3 with gravitational lensing”. In: *mnras* 482.4 (Feb. 2019), pp. 4744–4762. DOI: 10.1093/mnras/sty2833. arXiv: 1811.03628 [astro-ph.GA].
- [119] A.S.G. Robotham et al. “PROFIT: Bayesian profile fitting of galaxy images”. In: *mnras* 466.2 (Apr. 2017), pp. 1513–1541. DOI: 10.1093/mnras/stw3039. arXiv: 1611.08586 [astro-ph.IM].
- [120] G. Rodighiero, A. Cimatti, et al. “The first Herschel view of the mass-SFR link in high- z galaxies”. In: *aap* 518, L25 (July 2010), p. L25. DOI: 10.1051/0004-6361/201014624. arXiv: 1005.1089 [astro-ph.CO].
- [121] G. Rodighiero, E. Daddi, et al. “The Lesser Role of Starbursts in Star Formation at $z = 2$ ”. In: *apjl* 739.2, L40 (Oct. 2011), p. L40. DOI: 10.1088/2041-8205/739/2/L40. arXiv: 1108.0933 [astro-ph.CO].
- [122] Brett Salmon et al. “The Relation between Star Formation Rate and Stellar Mass for Galaxies at $3.5 \leq z \leq 6.5$ in CANDELS”. In: *apj* 799.2, 183 (Feb. 2015), p. 183. DOI: 10.1088/0004-637X/799/2/183. arXiv: 1407.6012 [astro-ph.GA].
- [123] Edwin E. Salpeter. “The Luminosity Function and Stellar Evolution.” In: *apj* 121 (Jan. 1955), p. 161. DOI: 10.1086/145971.
- [124] Mara Salvato, Olivier Ilbert, and Ben Hoyle. “The many flavours of photometric redshifts”. In: *Nature Astronomy* 3 (June 2019), pp. 212–222. DOI: 10.1038/s41550-018-0478-0. arXiv: 1805.12574 [astro-ph.GA].
- [125] Michael R. Santos. “Probing reionization with Lyman α emission lines”. In: *mnras* 349.3 (Apr. 2004), pp. 1137–1152. DOI: 10.1111/j.1365-2966.2004.07594.x. arXiv: astro-ph/0308196 [astro-ph].
- [126] S. Santos et al. “The evolution of rest-frame UV properties, $Ly\alpha$ EWs, and the SFR-stellar mass relation at $z \sim 2 - 6$ for SC4K LAEs”. In: *mnras* 493.1 (Mar. 2020), pp. 141–160. DOI: 10.1093/mnras/staa093. arXiv: 1910.02959 [astro-ph.GA].
- [127] P. Schechter. “An analytic expression for the luminosity function for galaxies.” In: *apj* 203 (Jan. 1976), pp. 297–306. DOI: 10.1086/154079.
- [128] J.L. Sérsic. “Influence of the atmospheric and instrumental dispersion on the brightness distribution in a galaxy”. In: *Boletín de la Asociación Argentina de Astronomía La Plata Argentina* 6 (Feb. 1963), pp. 41–43.
- [129] Takatoshi Shibuya et al. “Morphologies of $\sim 190,000$ Galaxies at $z = 0-10$ Revealed with HST Legacy Data. III. Continuum Profile and Size Evolution of $Ly\alpha$ Emitters”. In: *apj* 871.2, 164 (Feb. 2019), p. 164. DOI: 10.3847/1538-4357/aaf64b. arXiv: 1809.00765 [astro-ph.GA].
- [130] Rosalind E. Skelton et al. “3D-HST WFC3-selected Photometric Catalogs in the Five CANDELS/3D-HST Fields: Photometry, Photometric Redshifts, and Stellar Masses”. In: *apjs* 214.2, 24 (Oct. 2014), p. 24. DOI: 10.1088/0067-0049/214/2/24. arXiv: 1403.3689 [astro-ph.GA].
- [131] David Sobral et al. “The nature of luminous $Ly\alpha$ emitters at $z \sim 2 - 3$: maximal dust-poor starbursts and highly ionizing AGN”. In: *mnras* 477.2 (June 2018), pp. 2817–2840. DOI: 10.1093/mnras/sty782. arXiv: 1802.10102 [astro-ph.GA].

- [132] J.S. Speagle et al. “A Highly Consistent Framework for the Evolution of the Star-Forming “Main Sequence” from $z \sim 0 - 6$ ”. In: *apjs* 214.2, 15 (Oct. 2014), p. 15. DOI: 10.1088/0067-0049/214/2/15. arXiv: 1405.2041 [astro-ph.GA].
- [133] Charles C. Steidel et al. “Diffuse $Ly\alpha$ Emitting Halos: A Generic Property of High-redshift Star-forming Galaxies”. In: *apj* 736.2, 160 (Aug. 2011), p. 160. DOI: 10.1088/0004-637X/736/2/160. arXiv: 1101.2204 [astro-ph.CO].
- [134] Amber N. Straughn, Gerhard R. Meurer, et al. “Emission-Line Galaxies from the Pears Hubble Ultra Deep Field: a 2d Detection Method and First Results”. In: *aj* 135.4 (Apr. 2008), pp. 1624–1635. DOI: 10.1088/0004-6256/135/4/1624. arXiv: 0802.2912 [astro-ph].
- [135] Amber N. Straughn, Norbert Pirzkal, et al. “Emission-Line Galaxies from the Hubble Space Telescope Probing Evolution and Reionization Spectroscopically (PEARS) Grism Survey. I. The South Fields”. In: *aj* 138.4 (Oct. 2009), pp. 1022–1031. DOI: 10.1088/0004-6256/138/4/1022. arXiv: 0907.2254 [astro-ph.CO].
- [136] Y. Taniguchi et al. “Hubble Space Telescope/Advanced Camera for Surveys Morphology of $Ly\alpha$ Emitters at Redshift 5.7 in the COSMOS Field”. In: *apj* 701.2 (Aug. 2009), pp. 915–944. DOI: 10.1088/0004-637X/701/2/915.
- [137] C. Tohill et al. “Quantifying Non-parametric Structure of High-redshift Galaxies with Deep Learning”. In: *apj* 916.1, 4 (July 2021), p. 4. DOI: 10.3847/1538-4357/ac033c.
- [138] Adam R. Tomczak et al. “The SFR- M_* Relation and Empirical Star-Formation Histories from ZFOURGE* at $0.5 < z < 4$ ”. In: *apj* 817.2, 118 (Feb. 2016), p. 118. DOI: 10.3847/0004-637X/817/2/118. arXiv: 1510.06072 [astro-ph.GA].
- [139] Sidney van den Bergh. “Ten Billion Years of Galaxy Evolution”. In: *pasp* 114.798 (Aug. 2002), pp. 797–802. DOI: 10.1086/341708. arXiv: astro-ph/0204315 [astro-ph].
- [140] Sidney van den Bergh, Roberto G. Abraham, Richard S. Ellis, et al. “A Morphological Catalog of Galaxies in the Hubble deep Field”. In: *aj* 112 (Aug. 1996), p. 359. DOI: 10.1086/118020. arXiv: astro-ph/9604161 [astro-ph].
- [141] Sidney van den Bergh, Roberto G. Abraham, Laura F. Whyte, et al. “The Visibility of Galactic Bars and Spiral Structure at High Redshifts”. In: *aj* 123.6 (June 2002), pp. 2913–2924. DOI: 10.1086/340355. arXiv: astro-ph/0202444 [astro-ph].
- [142] A. van der Wel et al. “Structural Parameters of Galaxies in CANDELS”. In: *apjs* 203.2, 24 (Dec. 2012), p. 24. DOI: 10.1088/0067-0049/203/2/24. arXiv: 1211.6954 [astro-ph.CO].
- [143] E. Vanzella, F. Calura, M. Meneghetti, M. Castellano, et al. “Massive star cluster formation under the microscope at $z = 6$ ”. In: *mnras* 483.3 (Mar. 2019), pp. 3618–3635. DOI: 10.1093/mnras/sty3311. arXiv: 1809.02617 [astro-ph.GA].
- [144] E. Vanzella, F. Calura, M. Meneghetti, A. Mercurio, et al. “Paving the way for the JWST: witnessing globular cluster formation at $z > 3$ ”. In: *mnras* 467.4 (June 2017), pp. 4304–4321. DOI: 10.1093/mnras/stx351. arXiv: 1612.01526 [astro-ph.GA].

- [145] E. Vanzella, M. Castellano, et al. “Magnifying the Early Episodes of Star Formation: Super Star Clusters at Cosmological Distances”. In: *apj* 842.1, 47 (June 2017), p. 47. DOI: 10.3847/1538-4357/aa74ae. arXiv: 1703.02044 [astro-ph.GA].
- [146] A. Verhamme et al. “Lyman- α emission properties of simulated galaxies: interstellar medium structure and inclination effects”. In: *aap* 546, A111 (Oct. 2012), A111. DOI: 10.1051/0004-6361/201218783. arXiv: 1208.4781 [astro-ph.CO].
- [147] Katherine E. Whitaker et al. “Constraining the Low-Mass Slope of the Star Formation Sequence at $0.5 \leq z \leq 2.5$ ”. In: American Astronomical Society Meeting Abstracts 225, 329.04 (Jan. 2015), p. 329.04.
- [148] R.A. Windhorst et al. “Identification of faint radio sources with optically luminous interacting disk galaxies”. In: *nat* 375.6531 (June 1995), pp. 471–474. DOI: 10.1038/375471a0.
- [149] L. Wisotzki et al. “Nearly all the sky is covered by Lyman- α emission around high-redshift galaxies”. In: *nat* 562.7726 (Oct. 2018), pp. 229–232. DOI: 10.1038/s41586-018-0564-6. arXiv: 1810.00843 [astro-ph.GA].
- [150] Zheng Zheng and Joshua Wallace. “Anisotropic Lyman-alpha Emission”. In: *apj* 794.2, 116 (Oct. 2014), p. 116. DOI: 10.1088/0004-637X/794/2/116. arXiv: 1308.1405 [astro-ph.CO].

Appendix A

Appendix of GALFIT and EAZY Fits for Sub-sample

A.1 s_12390

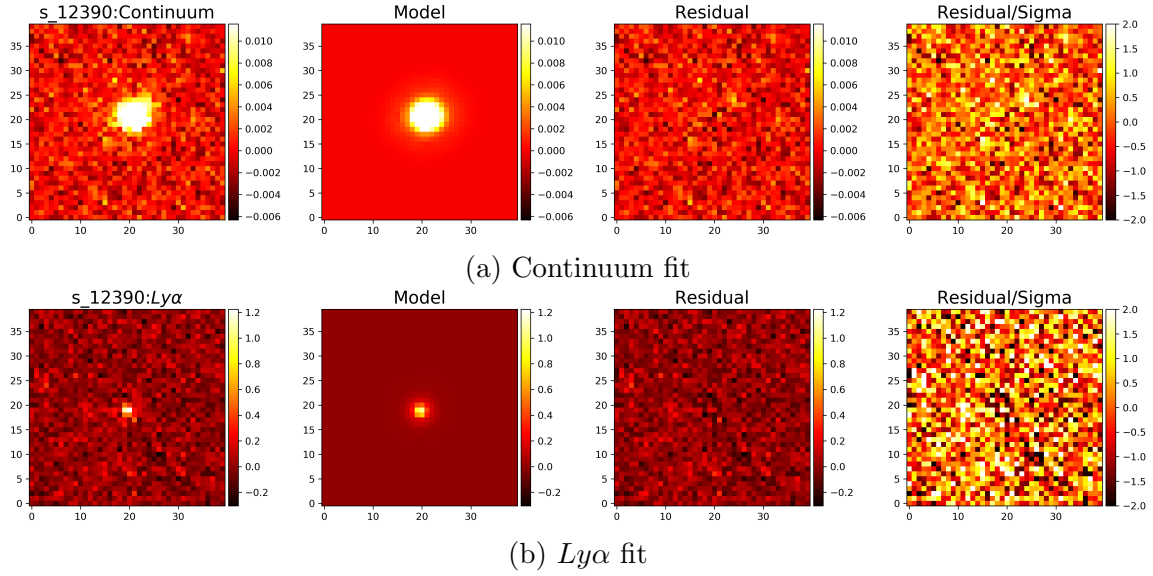


Figure A.1: s_12390 GALFIT fit with single Sérsic

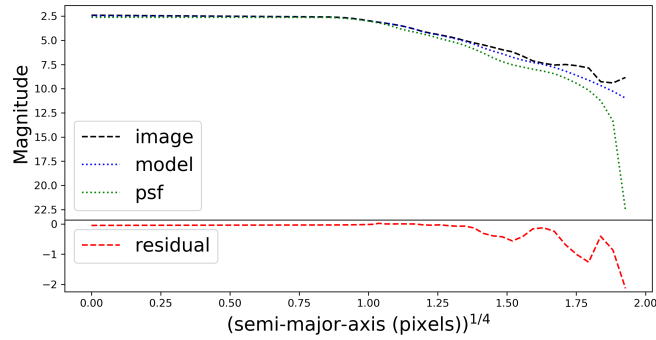


Figure A.2: s_12390 1D surface brightness profile

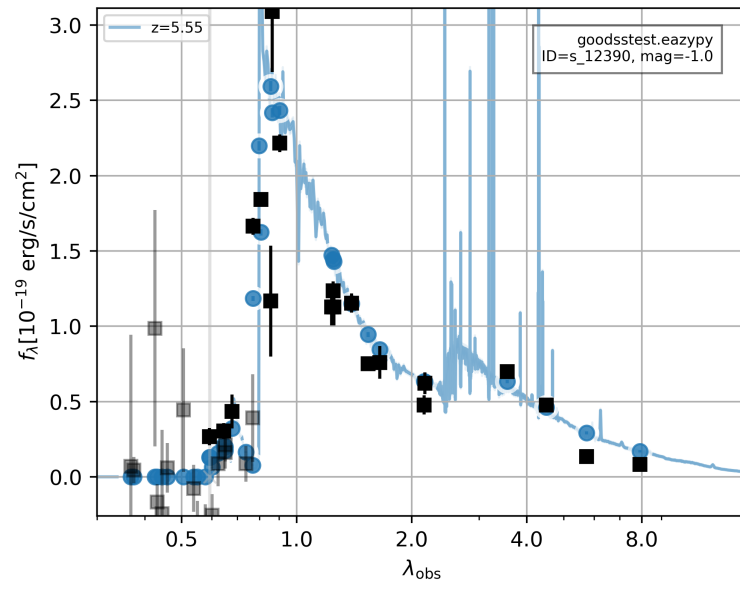


Figure A.3: s_12390 EAZY fit with fixed z at 5.55

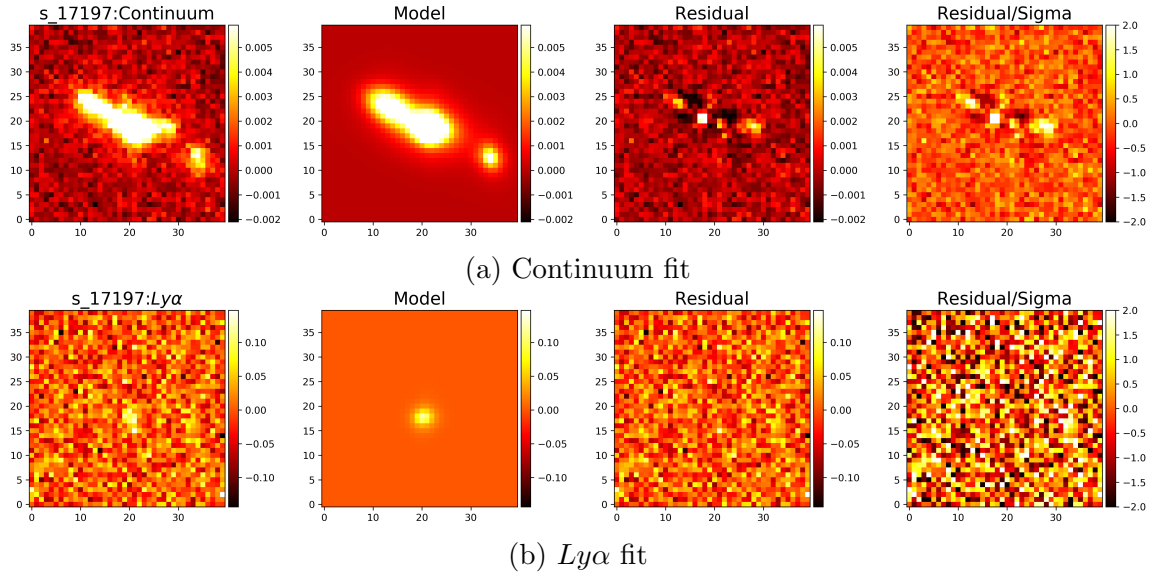
A.2 *s*_17197

Figure A.4: *s*_17197 GALFIT fit with 5 Sérsics for continuum and single Sérsic for line

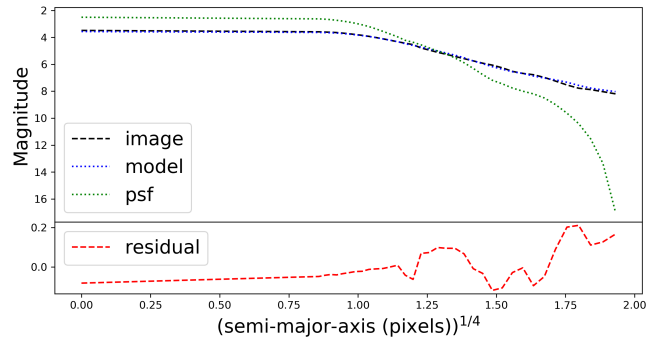


Figure A.5: *s*_17197 1D surface brightness profile

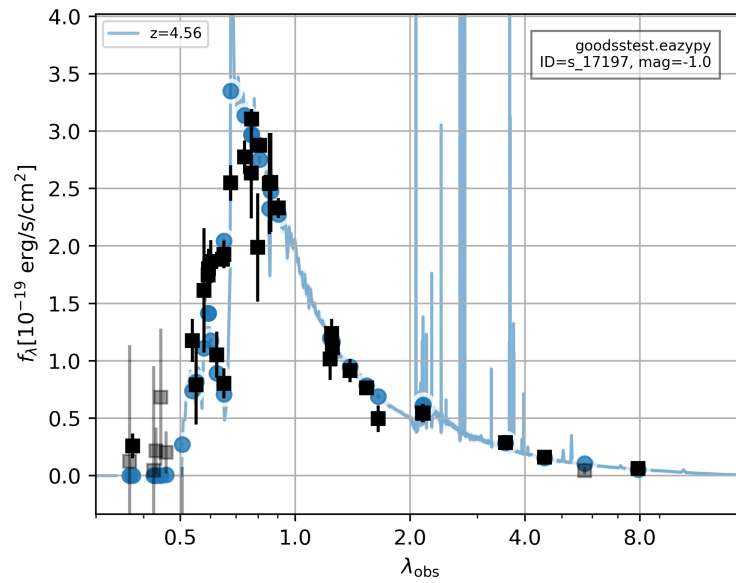


Figure A.6: *s*_17197 EAZY fit with fixed z at 4.56

A.3 s_17357

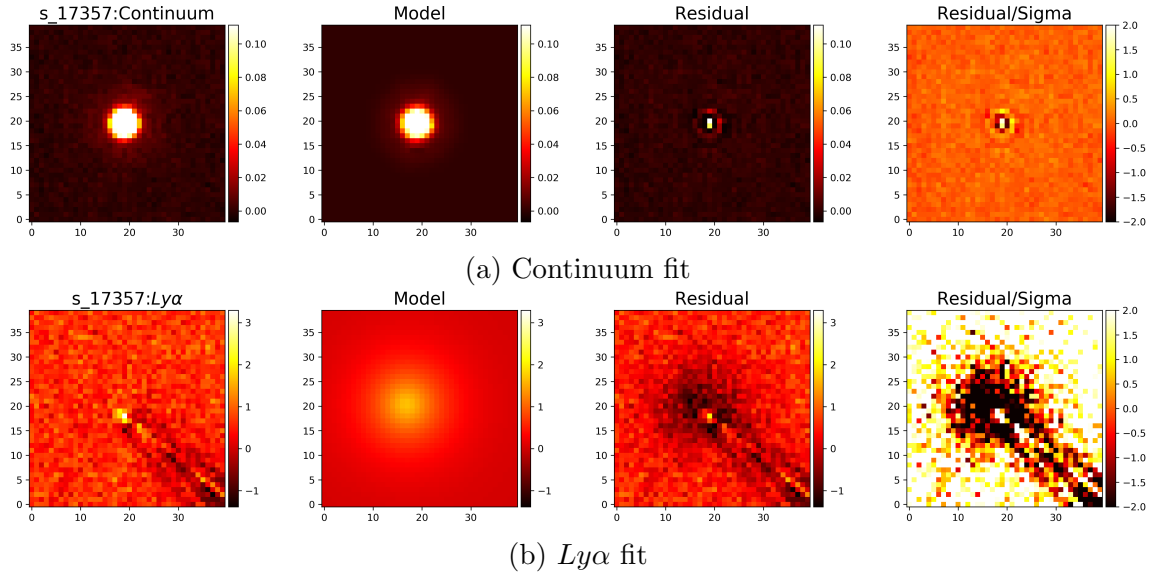


Figure A.7: s_17357 GALFIT fit with single Sérsic

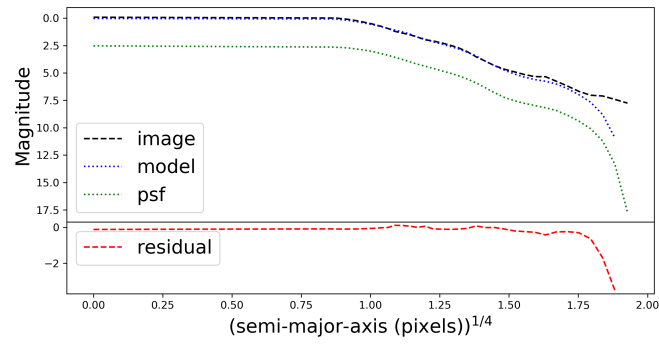
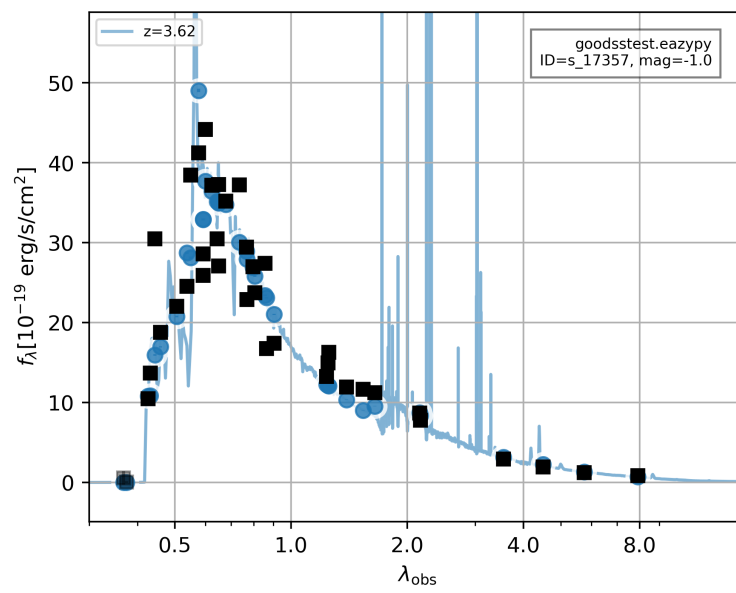
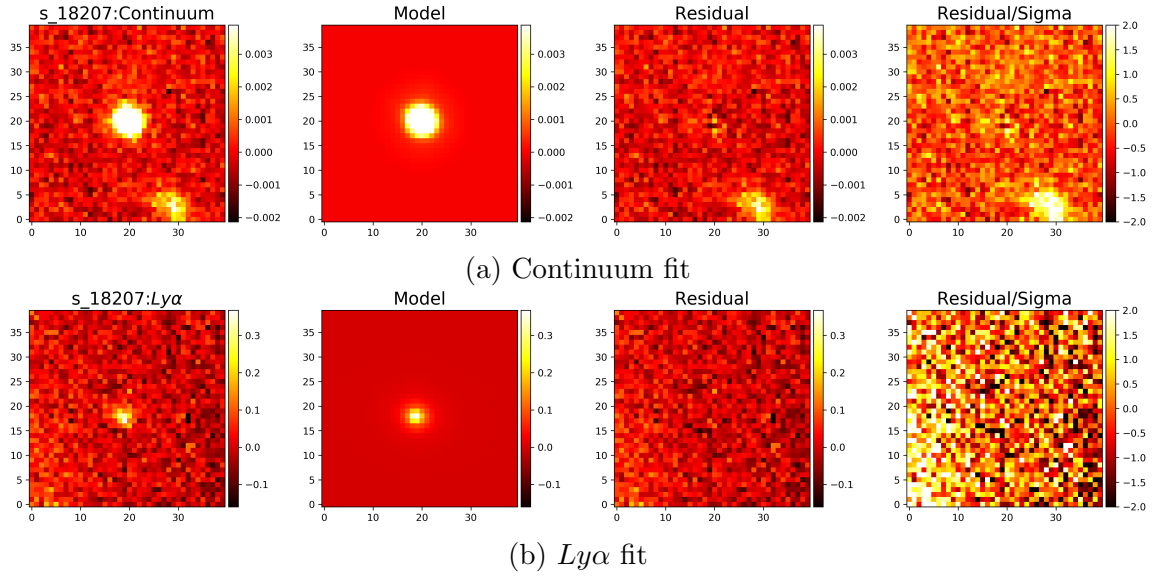
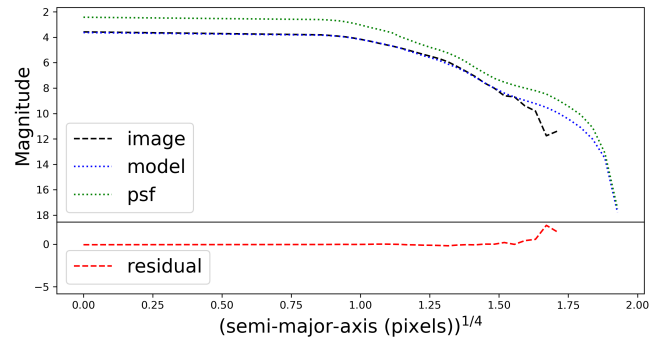
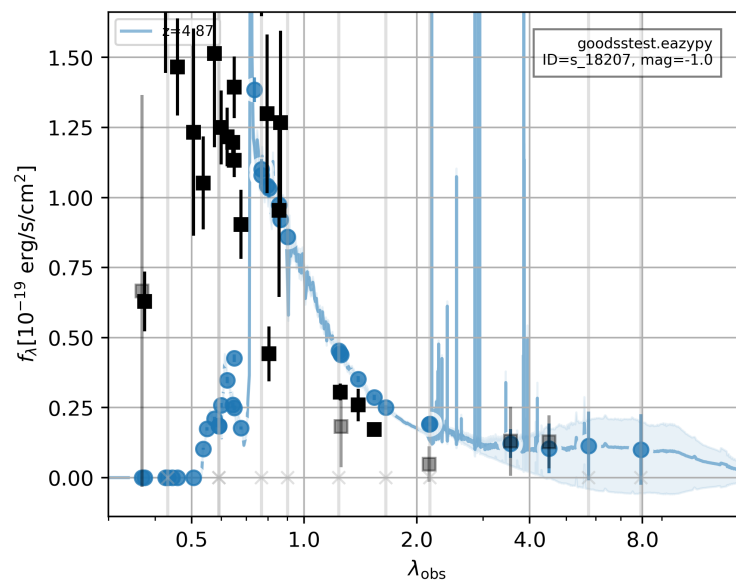


Figure A.8: s_17357 1D surface brightness profile

Figure A.9: s_17357 EAZY fit with fixed z at 3.62

A.4 *s*_18207Figure A.10: *s*_18207 GALFIT fit with single SérsicFigure A.11: *s*_18207 1D surface brightness profileFigure A.12: *s*_18207 EAZY fit with fixed z at 4.87

A.5 s_21181

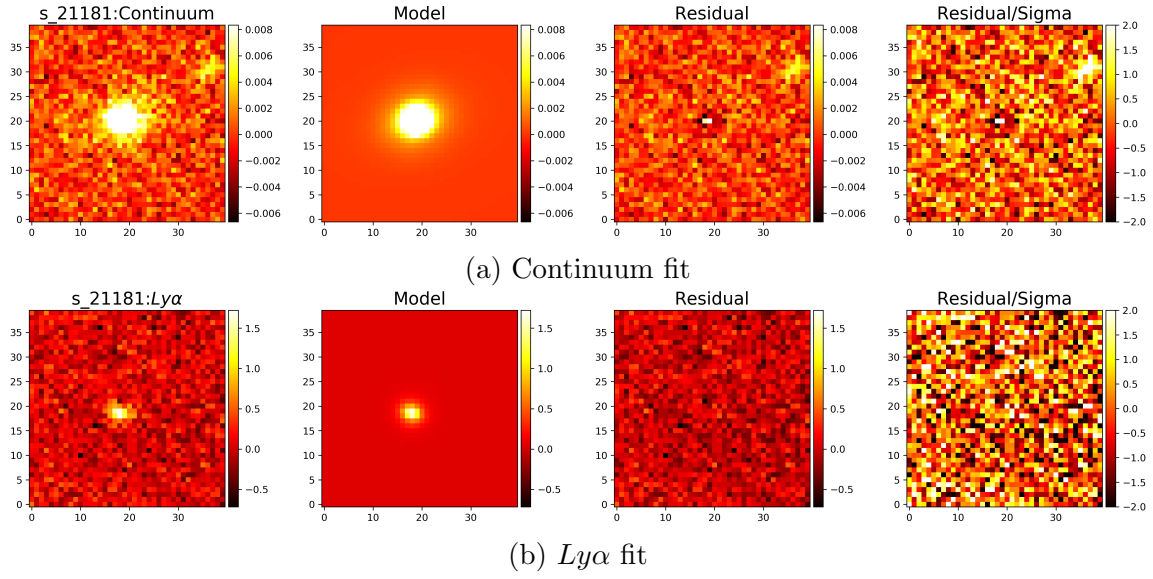


Figure A.13: s_21181 GALFIT fit with single Sérsic

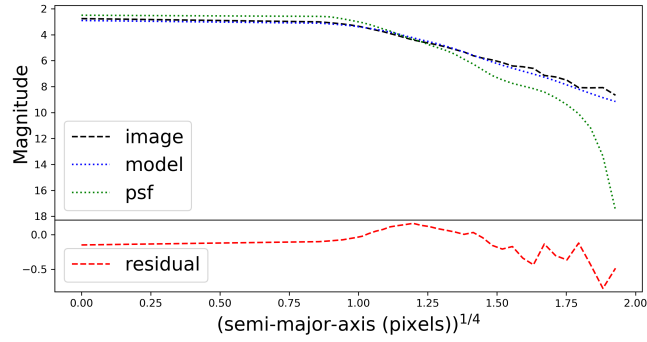
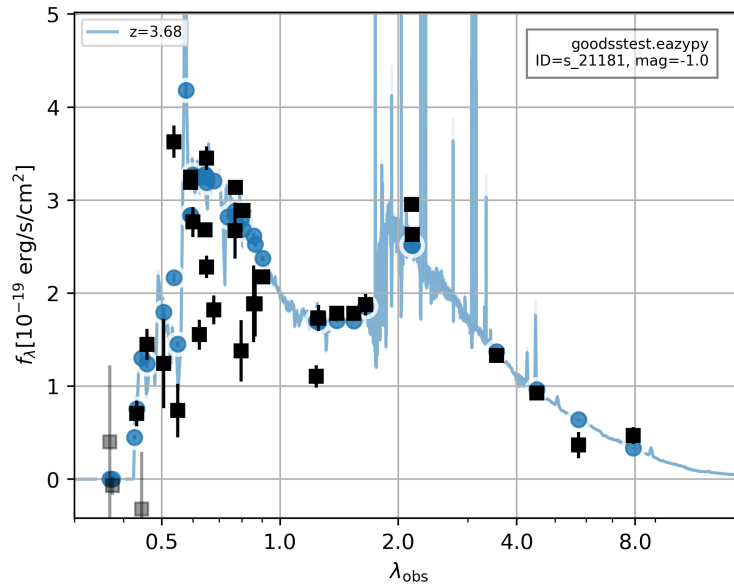


Figure A.14: s_21181 1D surface brightness profile

Figure A.15: s_21181 EAZY fit with fixed z at 3.68

A.6 s_26144

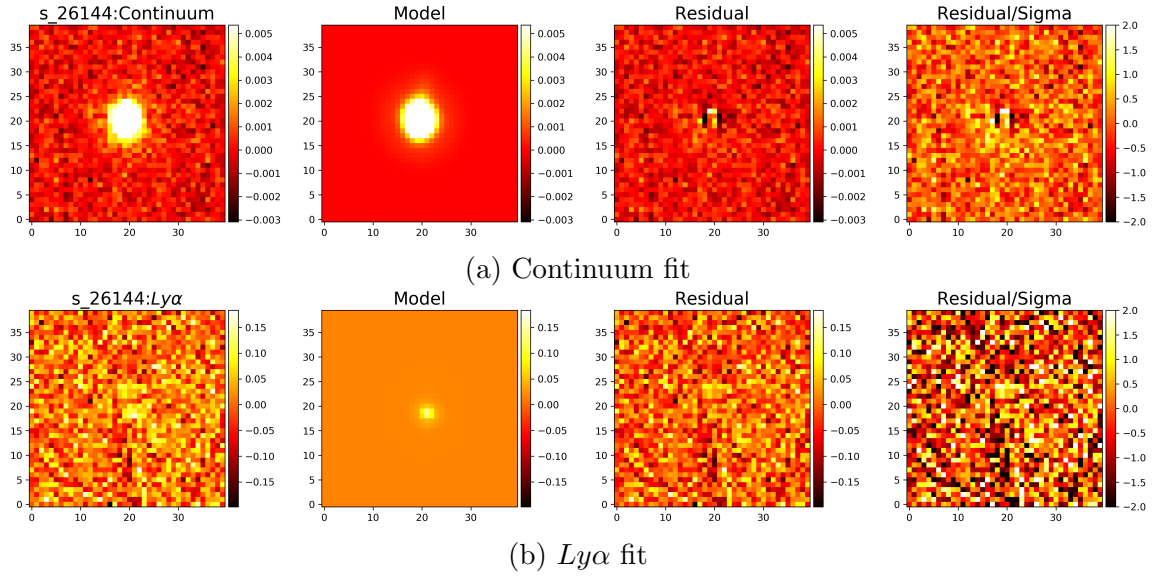


Figure A.16: s_26144 GALFIT fit with single Sérsic

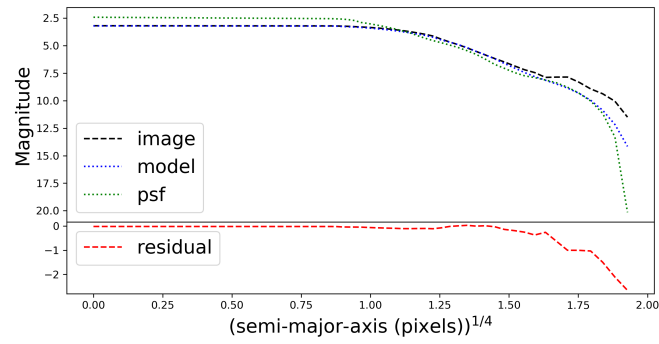
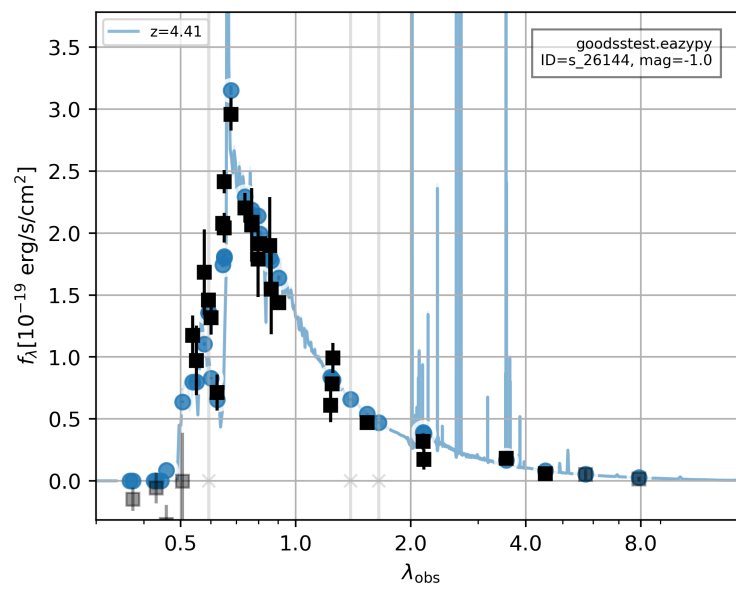


Figure A.17: s_26144 1D surface brightness profile

Figure A.18: s_26144 EAZY fit with fixed z at 4.41

A.7 s_33531

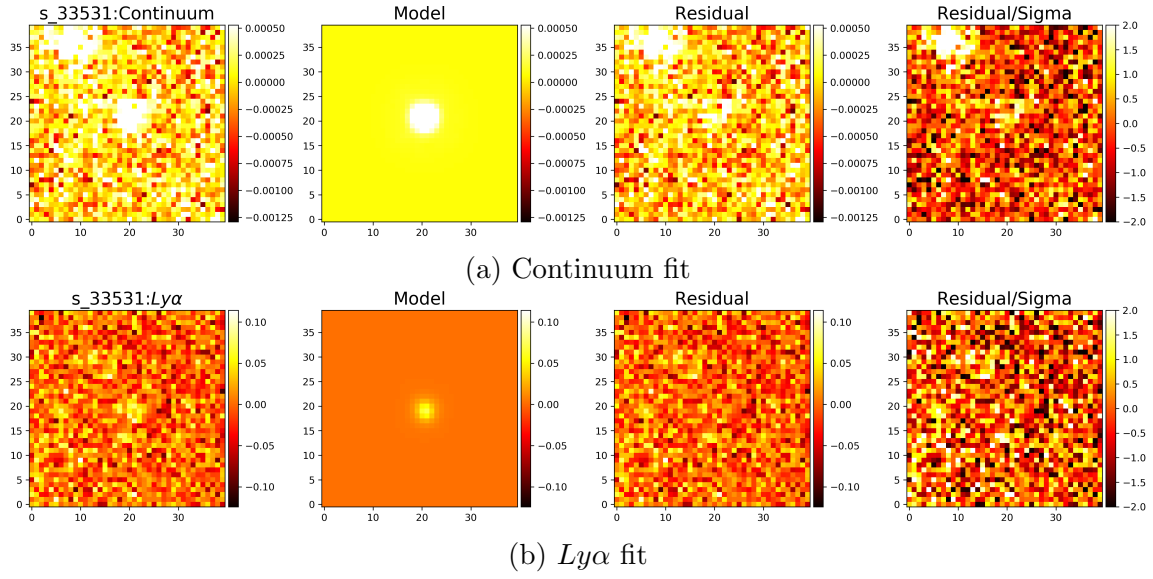


Figure A.19: s_33531 GALFIT fit with single Sérsic

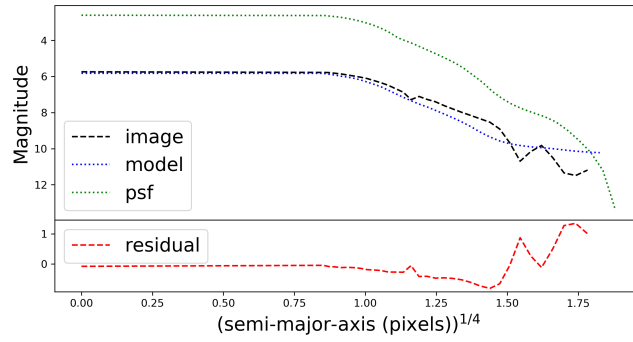
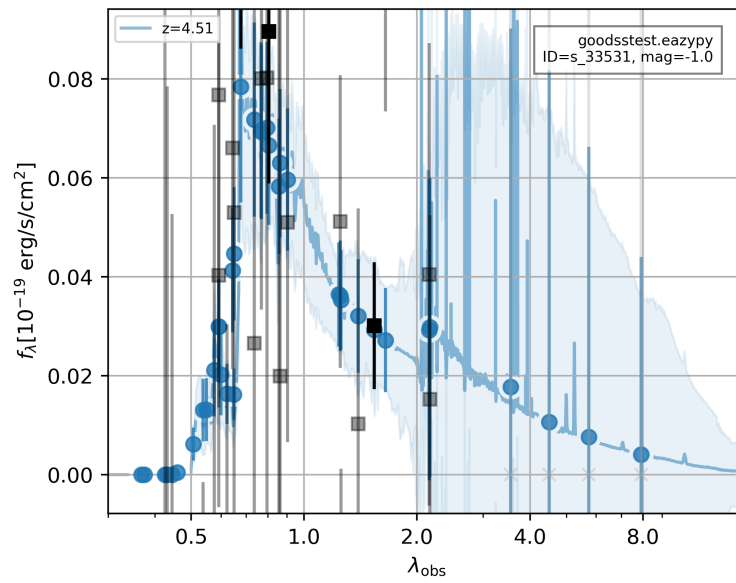


Figure A.20: s_33531 1D surface brightness profile

Figure A.21: s_33531 EAZY fit with fixed z at 4.51

A.8 s_36953

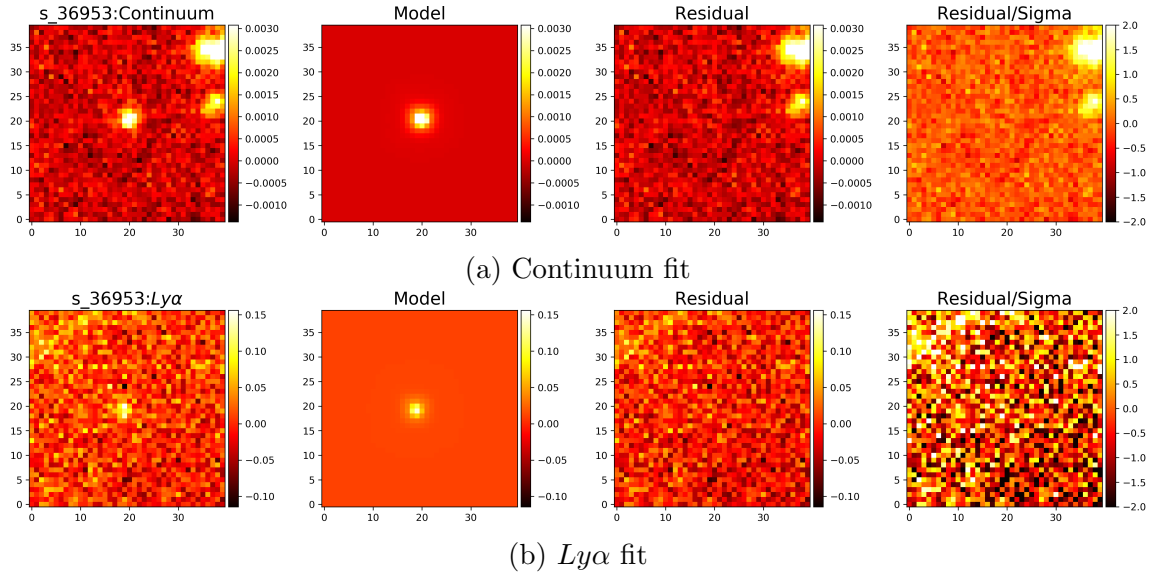


Figure A.22: s_36953 GALFIT fit with single Sérsic

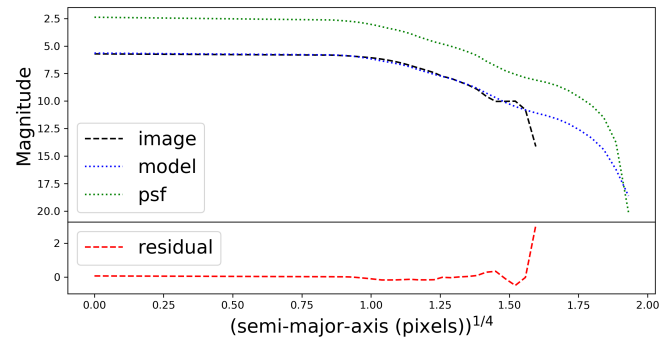
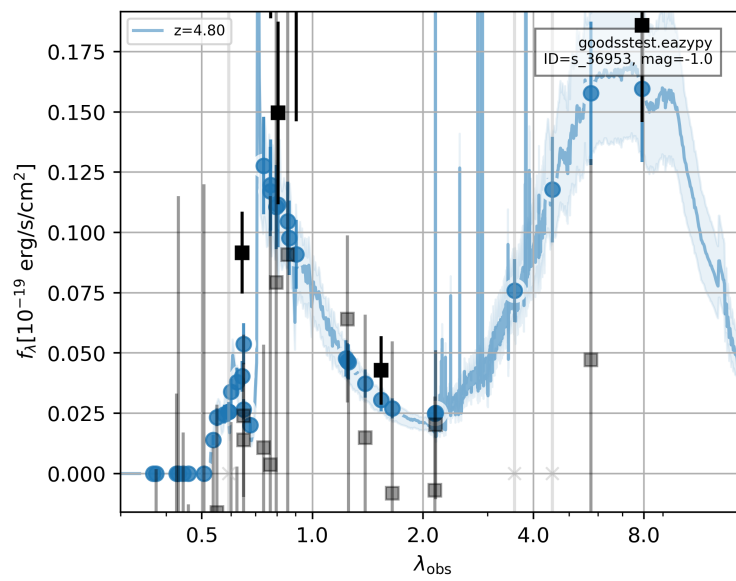


Figure A.23: s_36953 1D surface brightness profile

Figure A.24: s_36953 EAZY fit with fixed z at 4.80

A.9 s_43831

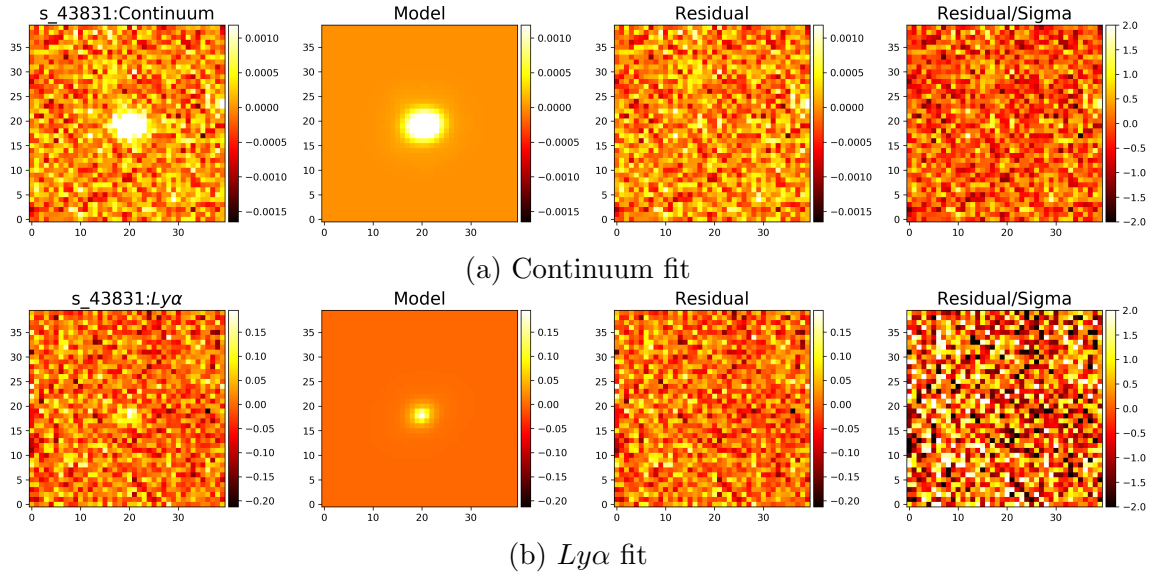


Figure A.25: s_42662 GALFIT fit with single Sérsic

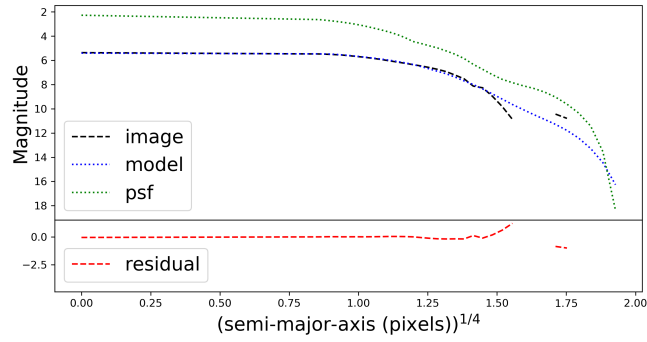
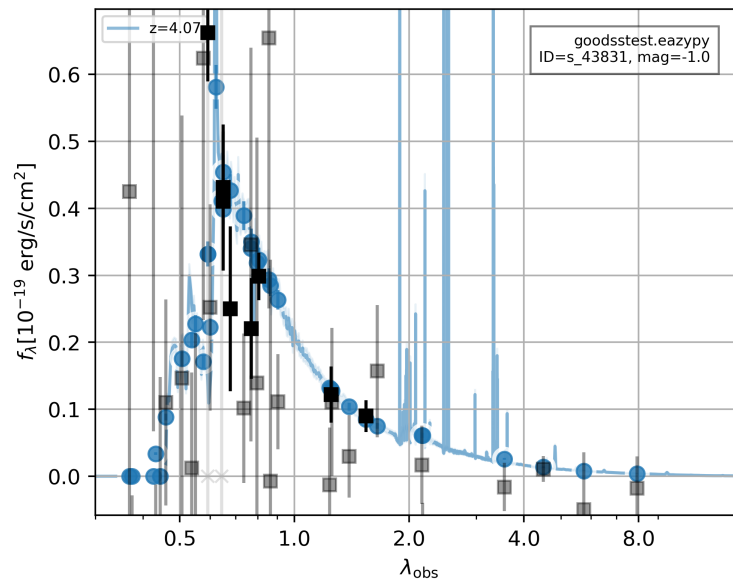


Figure A.26: s_43831 1D surface brightness profile

Figure A.27: s_43831 EAZY fit with fixed z at 4.07

A.10 s_44106

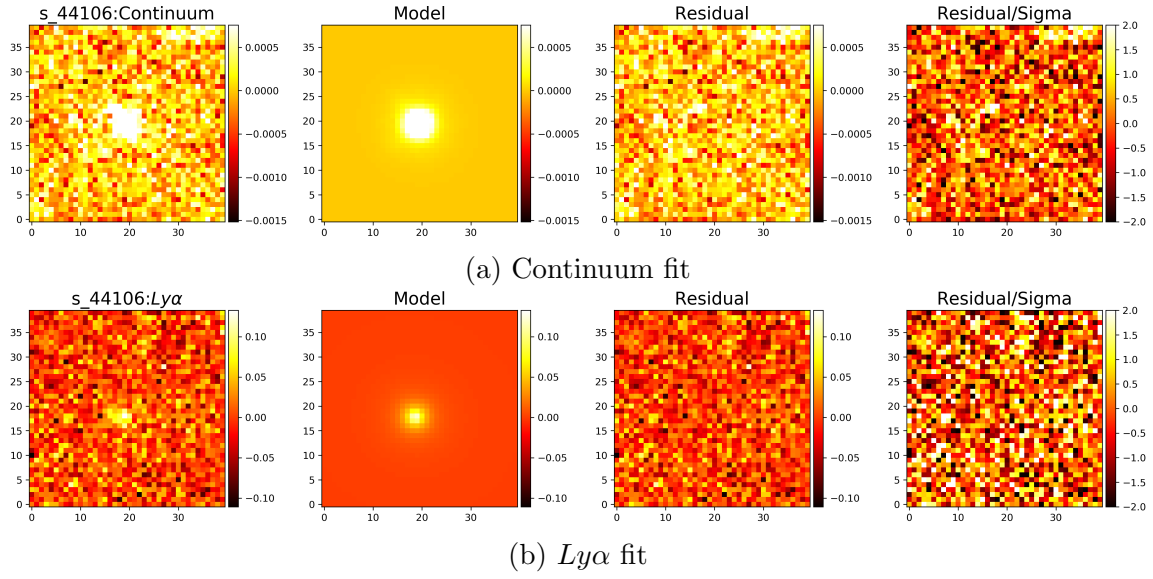


Figure A.28: s_44106 GALFIT fit with single Sérsic

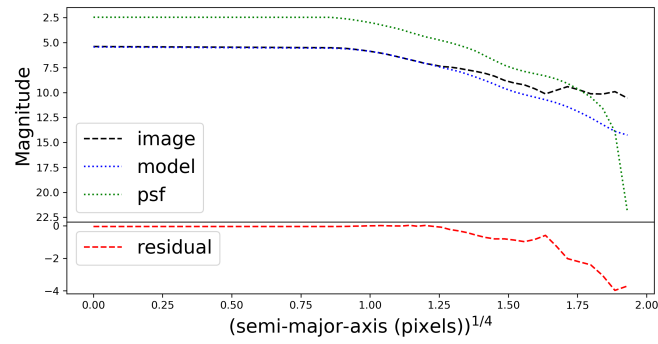
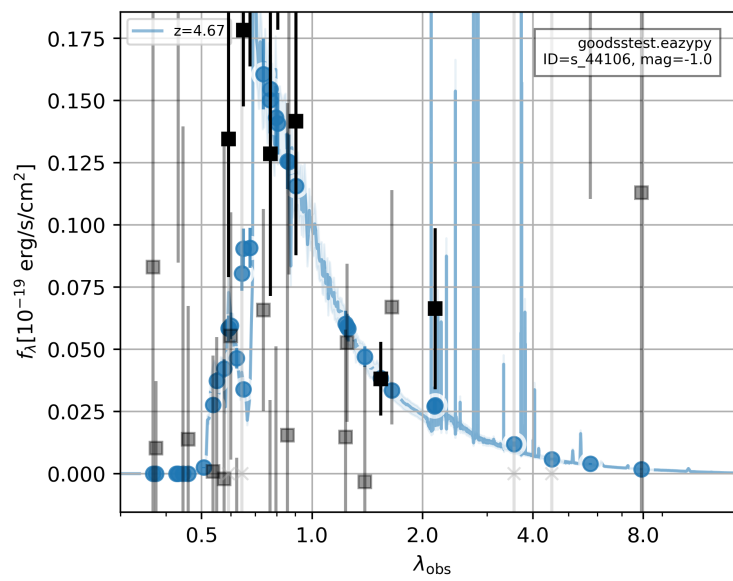


Figure A.29: s_44106 1D surface brightness profile

Figure A.30: s_44106 EAZY fit with fixed z at 4.67

A.11 n_16335

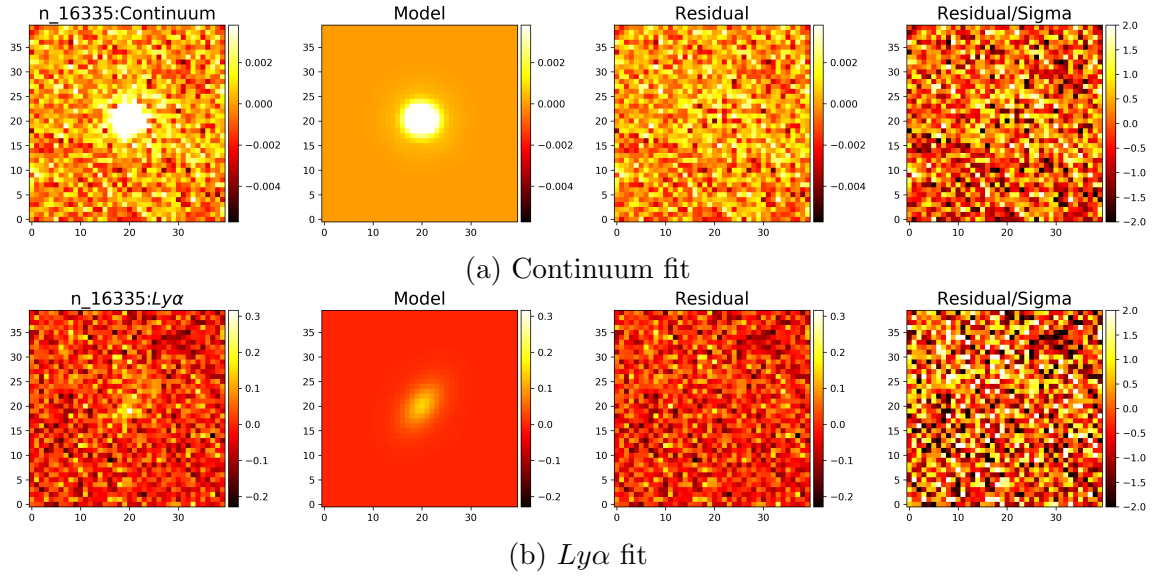


Figure A.31: n_16335 GALFIT fit with single Sérsic

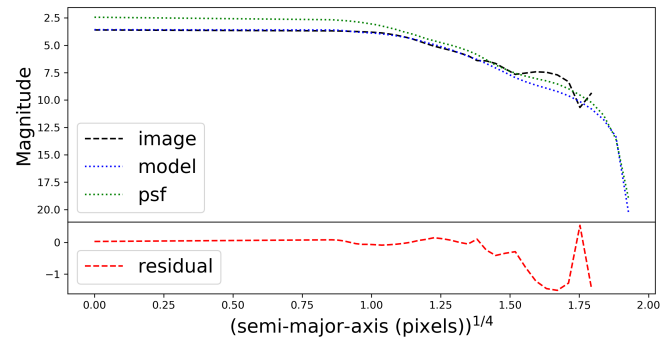
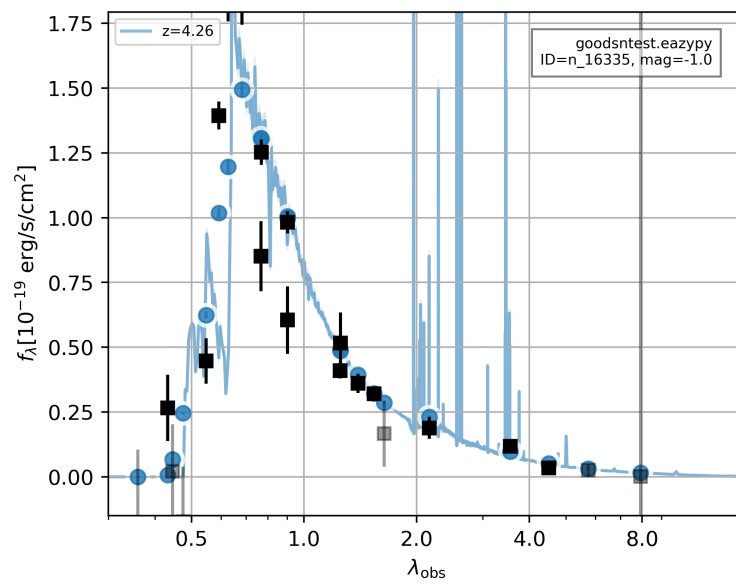
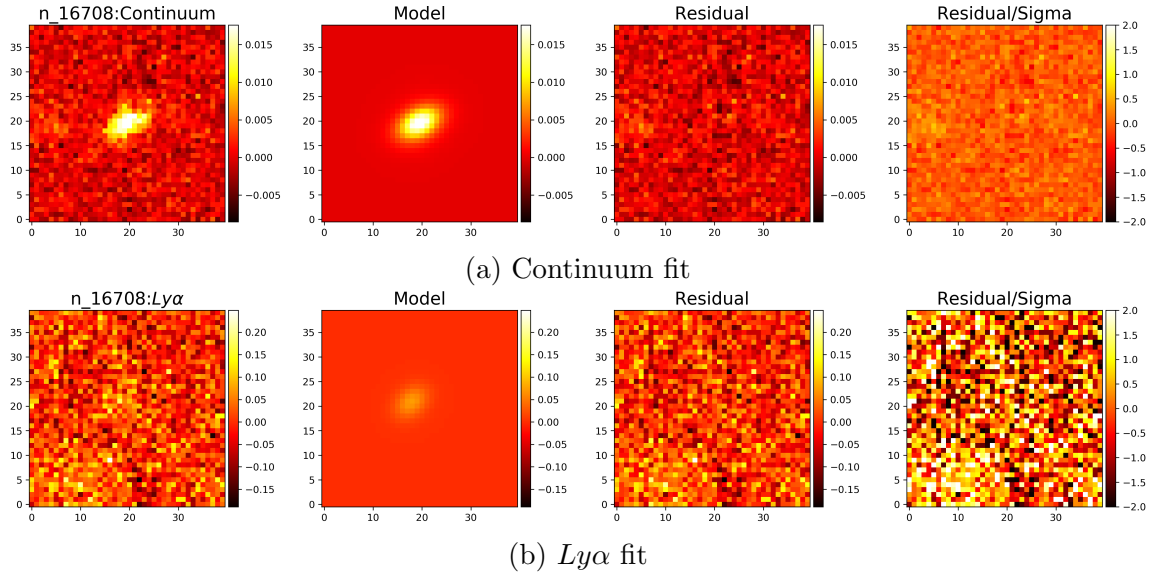
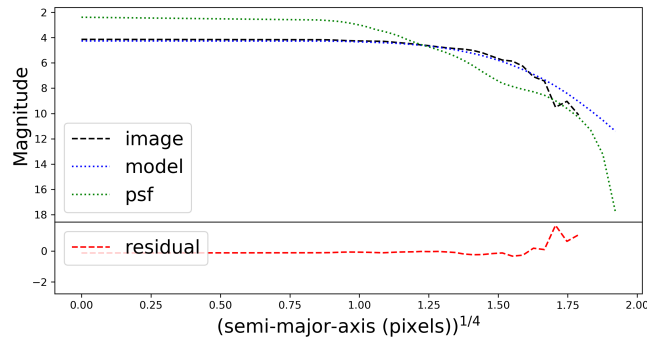
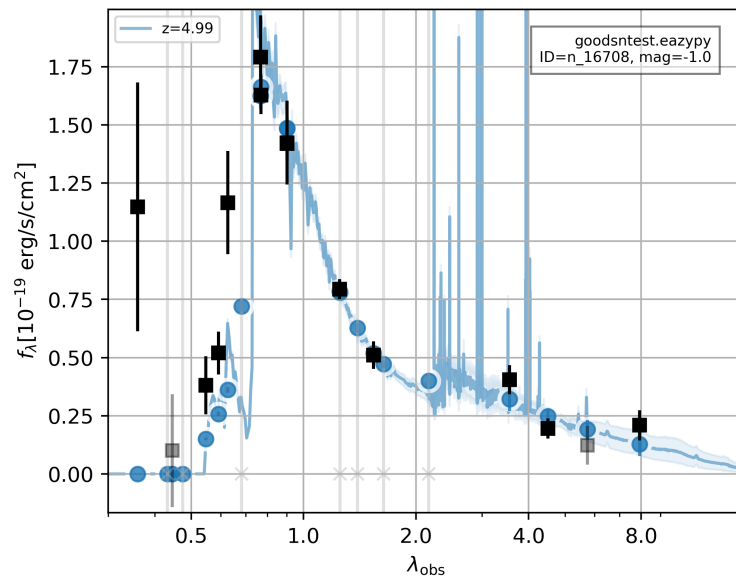


Figure A.32: n_16335 1D surface brightness profile

Figure A.33: n_16335 EAZY fit with fixed z at 4.26

A.12 *n*₁₆₇₀₈Figure A.34: *n*₁₆₇₀₈ GALFIT fit with single SérsicFigure A.35: *n*₁₆₇₀₈ 1D surface brightness profileFigure A.36: *n*₁₆₇₀₈ EAZY fit with fixed *z* at 4.99

A.13 n_29365

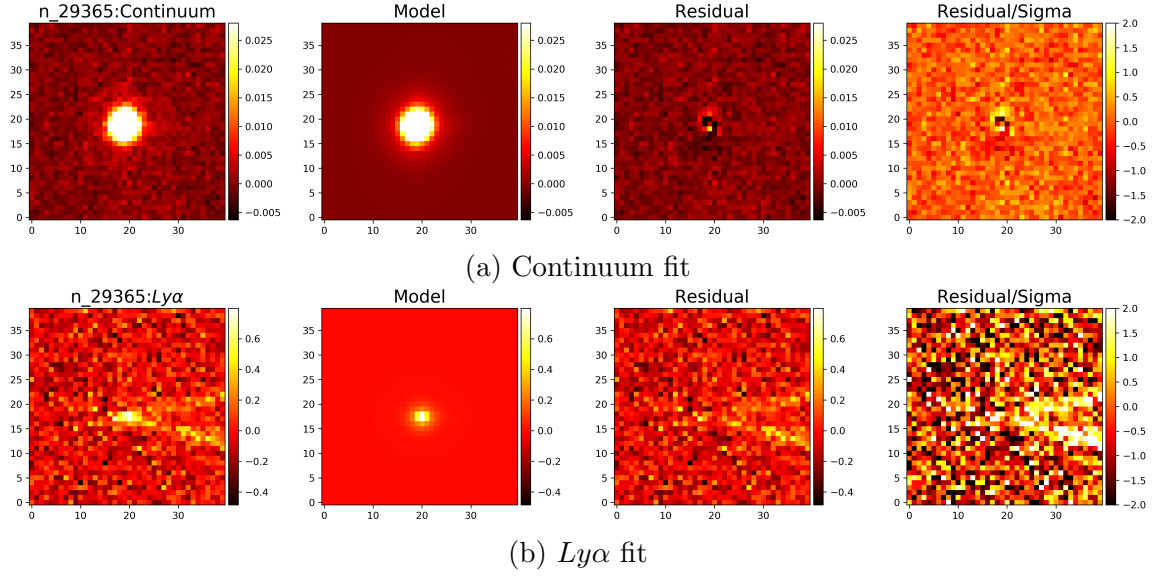


Figure A.37: n_29365 GALFIT fit with single Sérsic

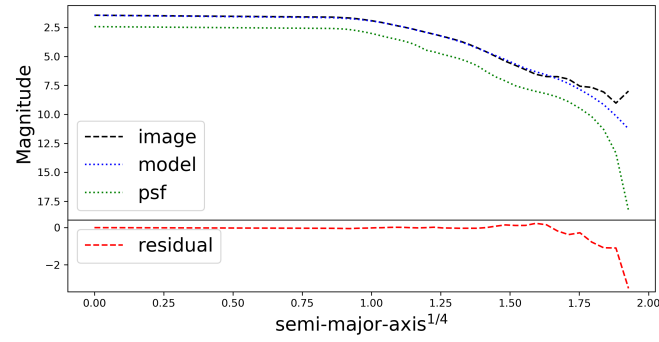
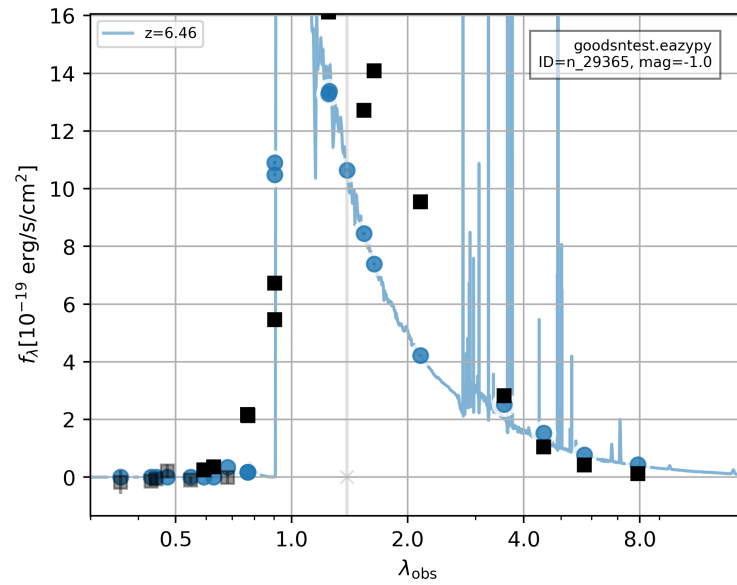
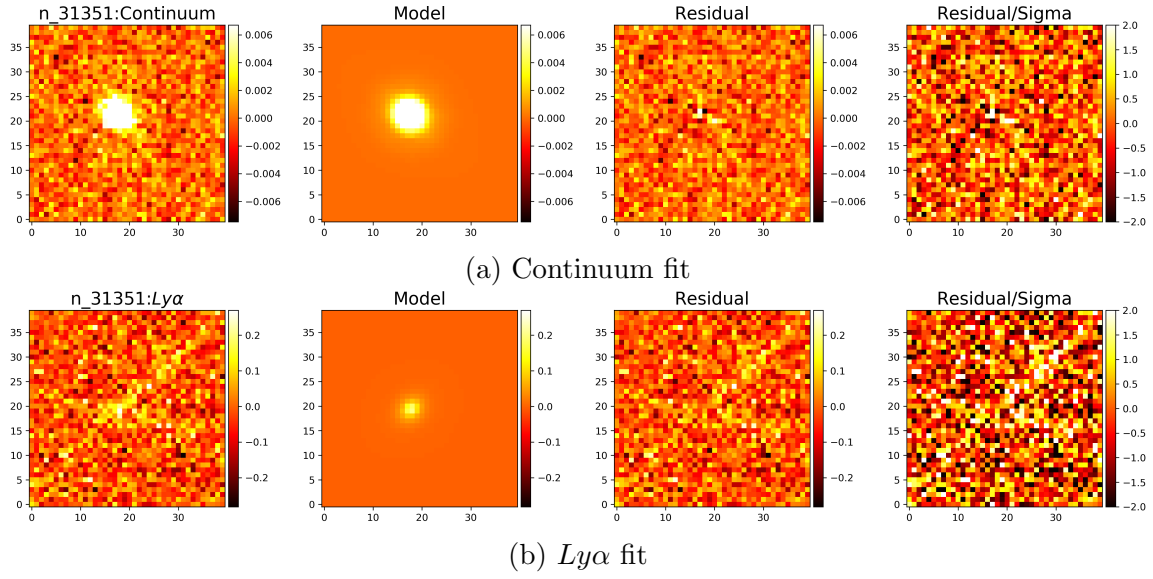
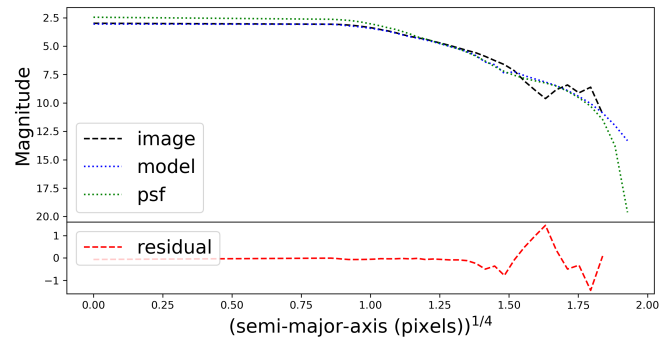
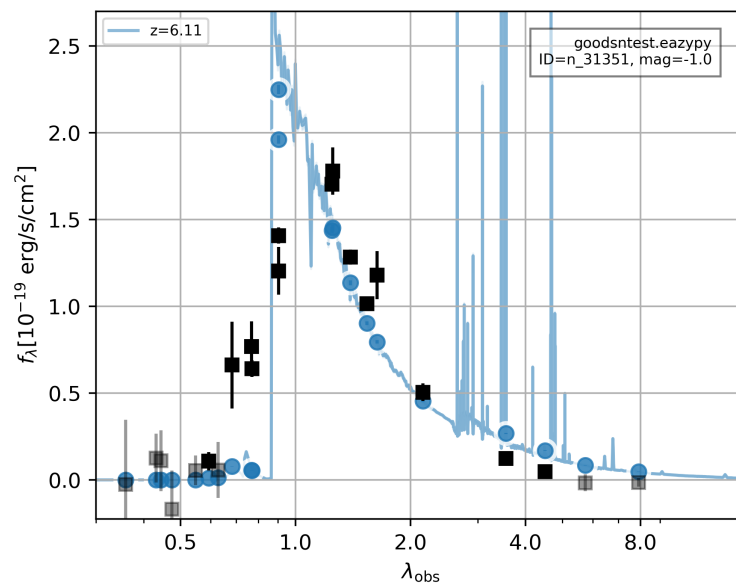


Figure A.38: n_29365 1D surface brightness profile

Figure A.39: n_29365 EAZY fit with fixed z at 6.46

A.14 *n*_31351Figure A.40: *n*_31351 GALFIT fit with single SérsicFigure A.41: *n*_31351 1D surface brightness profileFigure A.42: *n*_31351 EAZY fit with fixed z at 6.11

A.15 n_39376

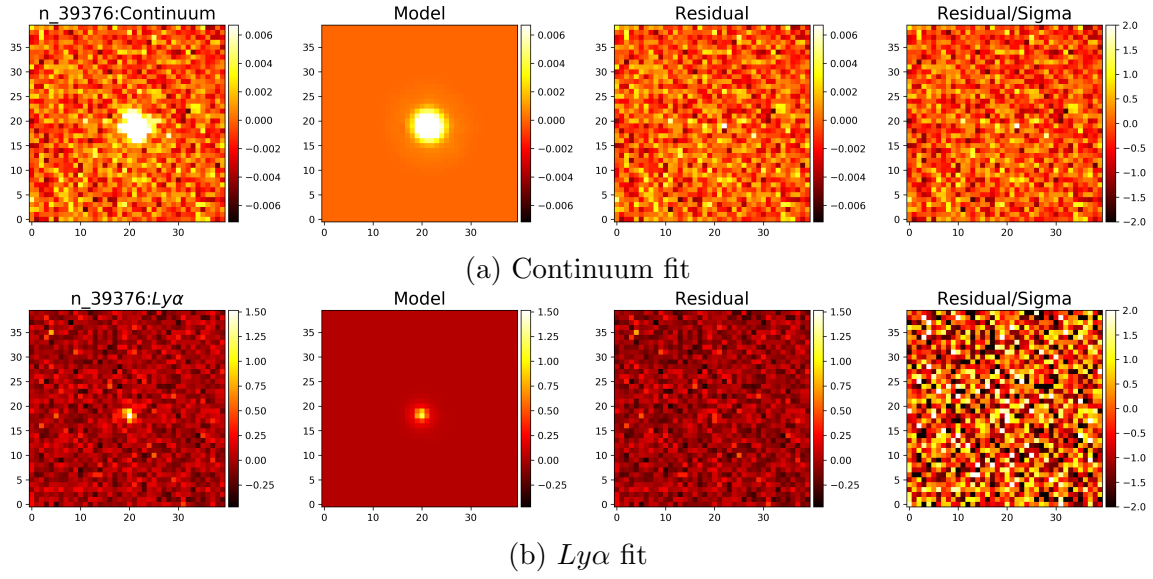


Figure A.43: n_39376 GALFIT fit with single Sérsic

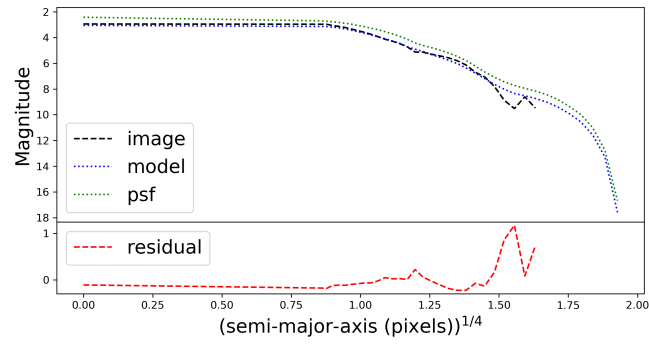
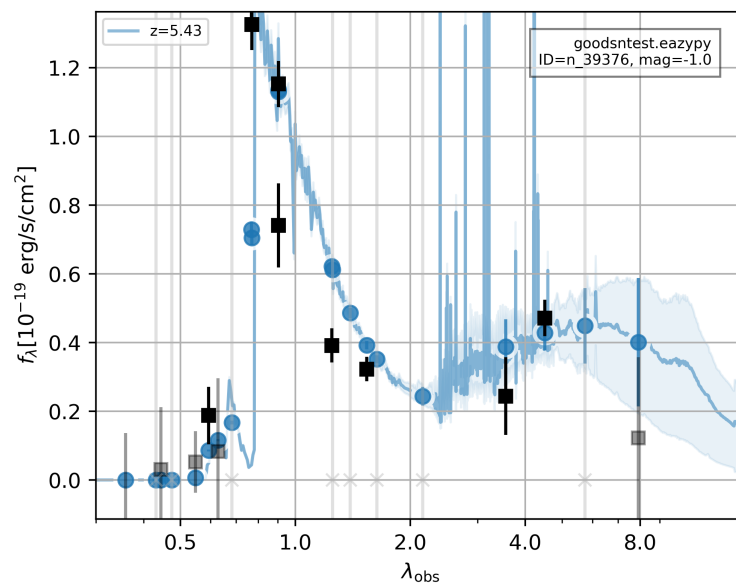


Figure A.44: n_39376 1D surface brightness profile

Figure A.45: n_39376 EAZY fit with fixed z at 5.43

A.16 e_06005

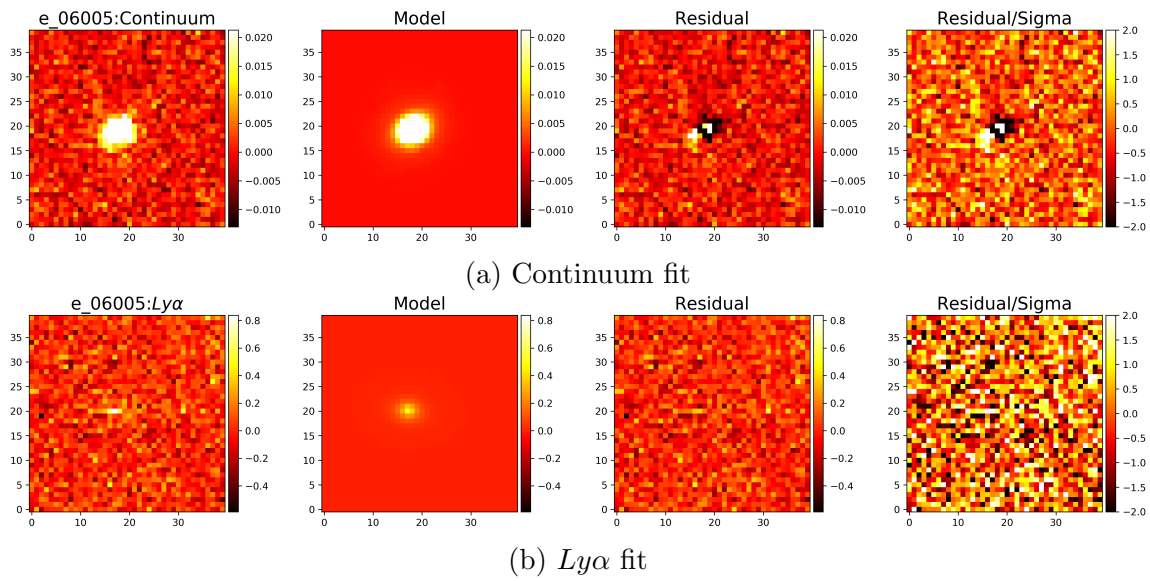


Figure A.46: e_06005 GALFIT fit with single Sérsic

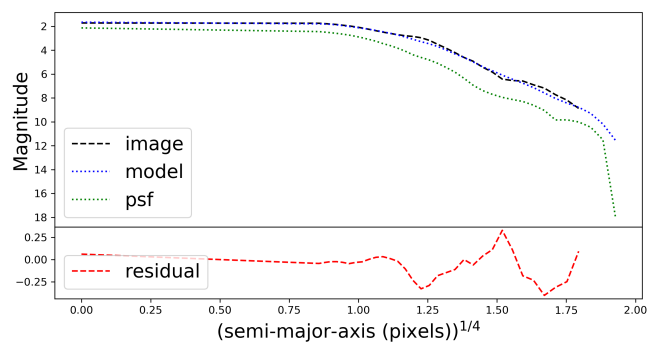
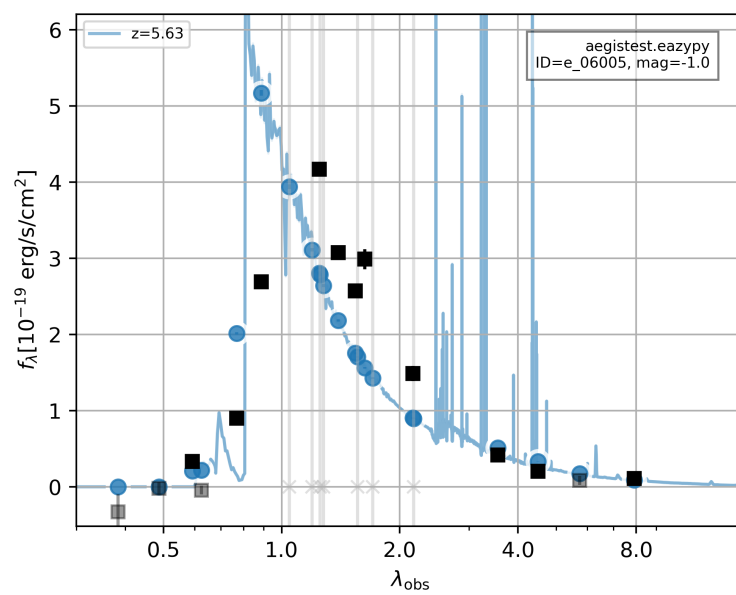


Figure A.47: e_06005 1D surface brightness profile

Figure A.48: e_06005 EAZY fit with fixed z at 5.63

A.17 e_18484

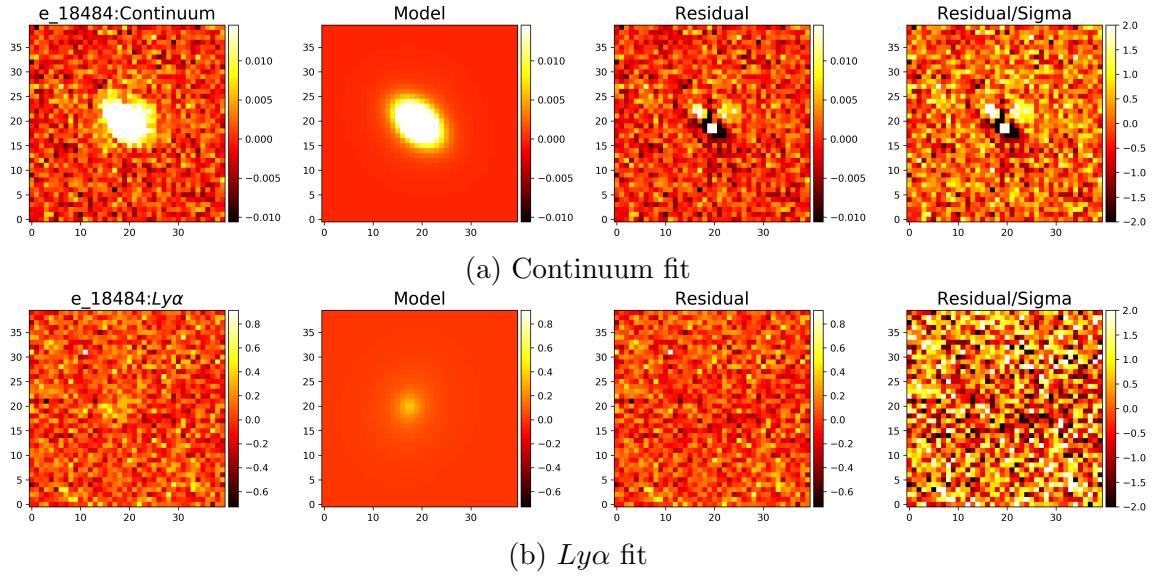


Figure A.49: e_18484 GALFIT fit with single Sérsic

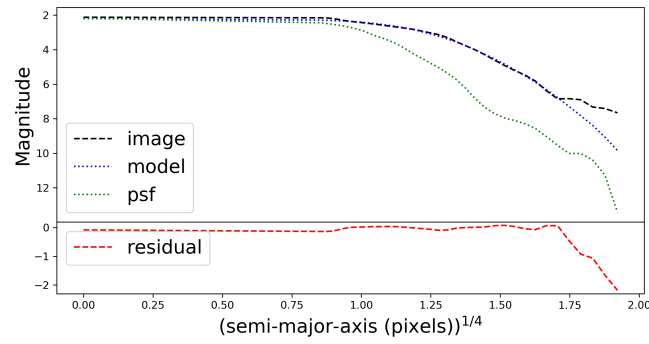
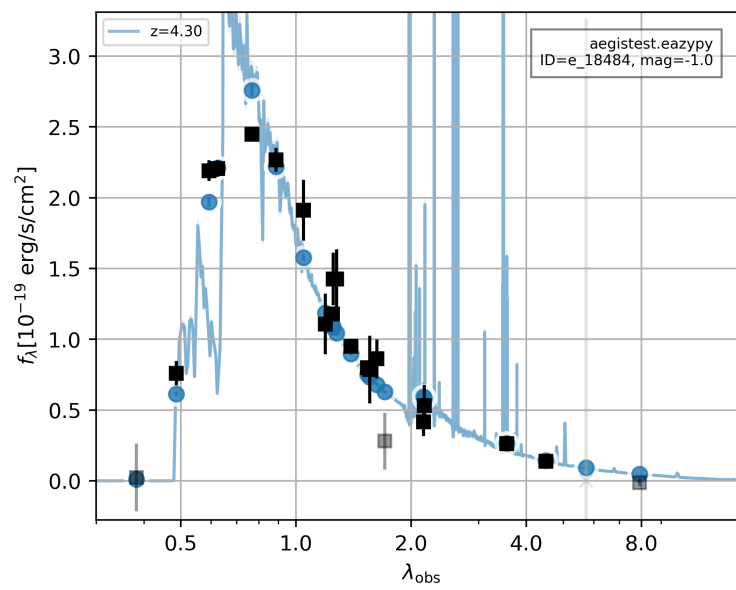


Figure A.50: e_18484 1D surface brightness profile

Figure A.51: e_18484 EAZY fit with fixed z at 4.30